THESIS FOR THE DEGREE OF LICENTIATE OF ENGINEERING

CORROSION OF FERRITIC STAINLESS STEELS USED IN SOLID OXIDE FUEL CELLS

INVESTIGATION OF NOVEL COATINGS IN SINGLE- AND DUAL-ATMOSPHERE CONDITIONS

Matthieu Tomas

Department of Chemistry and Chemical Engineering
CHALMERS UNIVERSITY OF TECHNOLOGY
Gothenburg, Sweden 2022

Corrosion of ferritic stainless steels used in solid oxide fuel cells
Investigation of novel coatings in single- and dual-atmosphere conditions
MATTHIEU TOMAS

Thesis for the degree of Licentiate of Engineering
Department of Chemistry and Chemical Engineering
Division of Energy and Materials
Chalmers University of Technology
SE-412 96 Gothenburg
Sweden
Telephone: +46 (0)31-772 1000
Nr: 2022:06

Cover:

Left: Cross-section of an interconnect exposed in dual atmosphere for 3000 h at 600 ℃. *Middle:* Cross-section of a Ce/Cu-coated AISI 441 exposed for 1000 h at 650 ℃ in humid atmosphere. *Right:* Top-view image of hematite nodules on AISI 441 exposed in dual atmosphere conditions.

Printed by Chalmers Reproservice
Gothenburg, Sweden 2022

Corrosion of Ferritic Stainless Steels used in Solid Oxide Fuel Cells
Investigation of Novel Coatings in Single- and Dual-Atmosphere Conditions
MATTHIEU TOMAS
Department of Chemistry and Chemical Engineering
Chalmers University of Technology

Abstract

Solid Oxide Fuel Cells (SOFCs) are systems that convert chemical energy into electrical energy. Their high electrical efficiency and clean emissions (when H_2 is used as fuel) make them a strong candidate for replacing conventional conversion systems, such as combustion engines. However, the high costs and limited life-times of SOFCs have hindered their widespread commercialisation.

One of the main costs in a fuel cell stack is for the interconnect, which connects the cells electrically. Interconnects are, nowadays, made of Ferritic Stainless Steel (FSS) and, when exposed to fuel cell operating temperatures, typically between 600℃ and 900℃, they suffer severe corrosion. The Cr_2O_3 layer that forms on the interconnects upon exposure to high temperatures mitigates the corrosion process to some extent. However, the formation of a chromia layer leads to two major issues: a) the volatilisation of Cr(VI) species, which poisons the cathode; b) an increase in the electrical resistance of the interconnect caused by the continuously growing oxide scale. Both of these issues can be mitigated by using coatings. The optimal candidates are spinel oxide coatings, due to their effectiveness at decreasing Cr evaporation and their high conductivity.

The first part of this thesis investigates the efficiency of Cu-based coatings for mitigating Cr(VI) evaporation, as compared to the Co-based coatings currently used. Two different processes are used for deposition of the coatings: a) Physical Vapour Deposition (PVD); and b) Thermal Spray (TS). It was found that, thin PVD coatings are as efficient as much thicker TS coatings at mitigating Cr(VI) evaporation when exposed at 650℃ in humid air. Area-specific resistance measurements showed that the PVD Ce/Cu coating is as good as the state-of-the-art PVD Ce/Co. The TS MnCo-oxide (MCO) coating, even if its microstructure differs, also display a good ASR.

The second part of this thesis focuses on the abilities of coatings that are exposed under simulated SOFC operating conditions, i.e. the simultaneous exposure to air and H_2/H_2O, to mitigate the so-called ‘dual-atmosphere effect’. Samples that were coated with Ce/Co on the air-side and uncoated on the fuel-side, as well as samples that were coated with Al or Al_2O_3 on the fuel-side and uncoated on the air-side were exposed at 600℃ for 3,000 h under dual-atmosphere conditions. It was found that applying a coating on the air-side delays the onset of break-away oxidation, although the best effect was seen for samples with Al and Al_2O_3 coatings on the fuel-side and the coating combination Al//Ce/Co. A significant reduction of the dual-atmosphere effect was observed once a coating was applied on the fuel-side of the interconnect.

Keywords: SOFC, Corrosion, Interconnect, Dual Atmosphere, Coatings, Area-Specific Resistance, Alumina, Copper

Acknowledgements

I would like to take this opportunity to acknowledge all the people who made this thesis possible and who supported me along the way.

First, I would like to thank my main supervisor Professor Jan Froitzheim and my co-supervisor Professor Jan-Erik Svensson for giving me the opportunity to complete my Licentiate in the Solid Oxide Fuel Cell Group at Chalmers University of Technology. I know that it was a rocky start, but we managed eventually. I am sure that the candies and chocolate tabs helped.

Second, I thank my former supervisor and colleague Claudia Goebel for giving the opportunity to integrate into the Solid Oxide Fuel Cell group as an intern (twice), and then as a Ph.D. student, and for her support along the way. I learned a lot from you, in terms of both Science and in practice. Thanks to you, I feel more confident as a researcher.

I would also thank the whole department for the guidance and continuous support they provided to me in the past 3 years.

This work would not have been possible without the fantastic team that I have been working with for the past years in the Fuel Cell Group. Thank you for welcoming me so warmly and bearing with me. Thank you Alberto, for the laughs, jokes, happiness, and support, especially in rough times. Thank you Reddy, for our always insightful talks and jokes. They have brightened up my days more than once. Thank you for always bearing with my moody behaviour. Thank you Camilla and Luca, #The Italians, for your perpetual good mood and the great talks that we had together. Overall, a big thank you to all of you for making the past 3 years exceptional.

Thank you Hannes, for the excellent advice, chats, support you gave me during my first internship in the Fuel Cell Group.

Special thanks also go to Julien for his never-ending friendship and support. Thanks for being the French part at Chalmers. I will miss our talks in your office and your ability to make me discover new ways to stimulate my nose.

Thank you Mariane for being the other French part at Chalmers. I will miss the nice chats and good *fika* that we shared.

Big and special thanks go to Valentina for her unconditional support and friendship throughout the years. Always ready to help me even from far away.

I would also like to thank Andrea, Sedi and Loli, for bringing happiness and laughter to the office.

Special thanks to my office mates Johan and Tommy, for creating an excellent atmosphere in the office and for all the help and useful insights.

Thanks to our industrial partners for interesting new research questions and good discussions. A special thanks to AB Sandvik Materials Technology and Elcogen AS for providing us with the necessary materials and coatings to make this research possible.

I would not be here without the support of my family and friends. Therefore, I would like to take this opportunity to thank my parents, Nathalie Peyruqueou and Jean-Yves Tomas, and my step-parents Cathy Tomas and Daniel Satre. Without your continuous support, I would not

have been able to achieve this. All of you know that it has been a bumpy road. Thank you so much!

And last but not least, I want to send a special and big thank you to Ema, for having lightened up my days over the past years, for supporting me, and for being here for me.

List of Publications

This thesis is based on the following manuscripts:

Manuscript I:
M. Tomas, V. Asokan, J. Puranen, J-E. Svensson and J. Froitzheim. **"Efficiencies of cobalt- and copper-based coatings applied by different deposition processes for applications in intermediate-temperature solid oxide fuel cells."** *Submitted to International Journal of Hydrogen Energy.*

Manuscript II:
M. Tomas, A. Visibile, J-E. Svensson and J. Froitzheim. **"Novel coatings for solid oxide fuel cell interconnects against the dual-atmosphere effect."**

Statement of author's contribution

I am the main author of all the appended manuscripts. For Manuscript I, I did most of the experimental work and microstructural analysis using the scanning electron microscope. The TEM analysis was performed by Dr. Vijayshankar Asokan. For Manuscript II, I performed most of the experimental and analytical work.

List of Acronyms

ASR: Area-Specific Resistance

BIB: Broad Ion Beam

CHP: Combined Heat and Power

EDS: Energy-Dispersive x-ray Spectroscopy

FC: Fuel Cell

FSS: Ferritic Stainless Steel

InCF: Intrinsic Chemical Failure

IT-SOFC: Intermediate-Temperature Solid Oxide Fuel Cell

$LaCrO_3$: Lanthanum chromite

LSCF: $(La,Sr)(Co,Fe)O_3$

LSM: Lanthanum Strontium Manganite

MCO: $(Mn,Co)_3O_4$

MICF: Mechanically Induced Chemical Failure

PEMFC: Proton Exchange Membrane Fuel Cell

PVD: Physical Vapour Deposition

RE: Reactive Element

SEM: Scanning Electron Microscope

SOEC: Solid Oxide Electrolyser Cell

SOFC: Solid Oxide Fuel Cell

TEC: Thermal Expansion Coefficient

TEM: Transmission Electron Microscope

TS: Thermal Spray

YSZ: Yttria-Stabilised zirconia

Contents

1 Introduction

1.1 Background

In 2021, the UN Climate Change Conference (COP26) brought together world leaders to find solutions and to accelerate actions to deal with climate change. Now, more than ever, the world needs new ways to produce clean/renewable energy. Scientists have warned that global warming will have significant consequences. An elevation of the global temperature by as little as 2°C will have a disastrous impact on the world [1-3]. Global energy consumption still relies heavily on fossil fuels, and much less so on renewable sources of energy (Figure 1). Today, countries such as India, China, Canada, the United States, and Australia still rely primarily on fossil fuels to produce the energy necessary for Society.

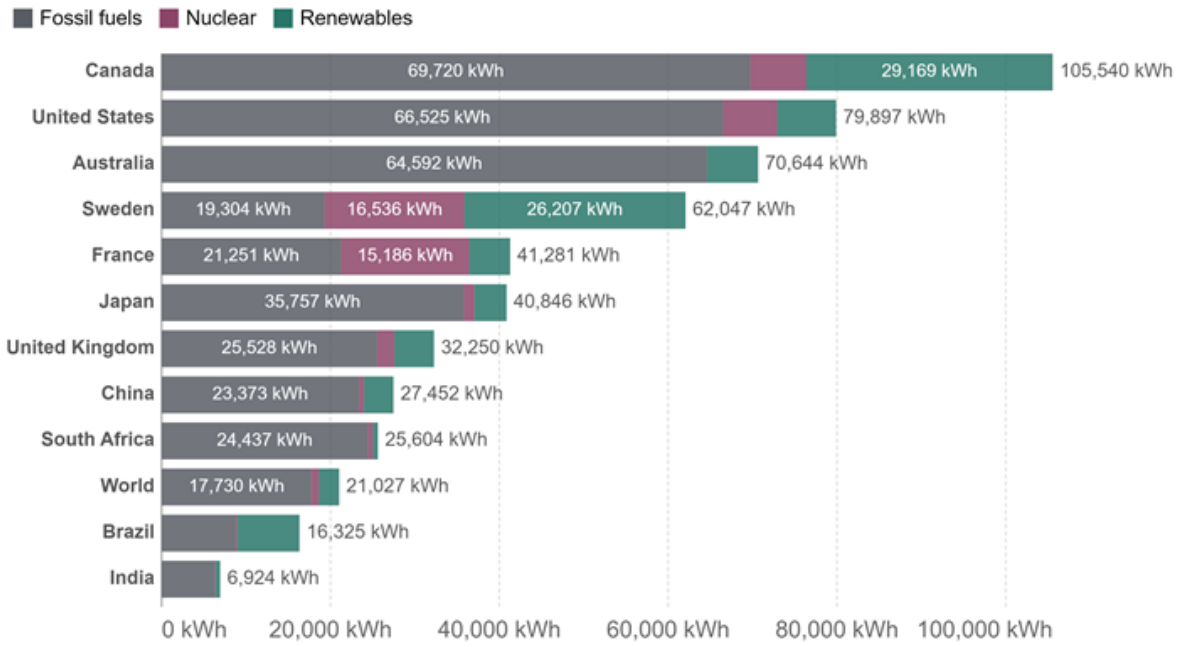

Figure 1: Per capita energy consumption by source [4].

Societies need to switch from fossil fuels, such as coal, oil, and shale gas, to more-sustainable energy sources, such as solar energy, wind energy, geothermal energy, to reduce greenhouse gas emissions. The switch relies heavily on advanced renewable energy generation systems, such as solar panels and wind turbines. However, the main drawback of these systems is their intermittent nature, so research has focused more on electricity storage systems combined with more-flexible and green energy conversion systems. In this context, Fuel Cells (FCs) represent one of the main candidates. FCs can be found in various forms [5]. One of the most widely used forms is Proton Exchange Membrane Fuel Cells (PEMFCs). These have the advantages of: attaining efficiencies of up to 60% when high purity hydrogen is used, having low operating temperatures of around 80°C, being suitable for mobile applications due to quick start-up times, and having good power output levels. However, PEMFCs need a catalyst to work, for example platinum, which is expensive. In addition, pure hydrogen must be used as

the fuel, and it should not be contaminated with carbon monoxide (CO) [6, 7]. The limitation of high-purity H_2 significantly affects the application of this technology for some uses. Therefore, the Solid Oxide Fuel Cell (SOFC) technology is being considered owing to its greater fuel flexibility. In SOFC, a solid oxide electrolyte that is permeable to oxygen ions is used instead of, for example, a proton exchange membrane. The main drawback of this technology is its high operating temperature, which ranges from 600°C to 900°C, as compared to the low operating temperature of PEMFC, which is around 80°C. However, the additional heat can be used in Combined Heat and Power (CHP) units or for further energy generation in gas or steam turbines. SOFCs have high electrical efficiency (>60%), and by utilising the heat produced, the efficiency can be increased up to 90% [8-10].

The interconnects or bipolar plates are essential for any FC system, in that their primary function is to connect multiple FCs in series, to form an FC stack with reasonable voltage output. Nowadays, interconnects in SOFCs are constructed of Ferritic Stainless Steels (FSS) and account for around 34% of the overall cost for a 1 kW stack, with a production of 50,000 units [11]. For the SOFC technology to become commercially attractive, the price per kWh must be reduced. This will involve reducing material costs by using commercially available FSS, decreasing the total cost of coating the steel, and reducing the operating temperature [10, 12, 13]. Another challenge to SOFC system adoption is its limited life-time. For stationary systems to have commercial feasibility, an expected life-time of at least 40,000 h is needed. However, the use of FSS as interconnects makes this goal more challenging to reach. Metallic interconnects suffer from corrosion when exposed to high temperatures of ≥600°C. Phenomena such as increased electrical resistance, Cr evaporation, and the dual-atmosphere effect exert strong impacts on the life-times of the interconnects and the FCs [14, 15].

Understanding the corrosion mechanism allows for the development of mitigation strategies. One example is the reduction of Cr evaporation through the application of a coating to the air-facing side of the interconnect, such as the state-of-the-art coating $(Mn,Co)_3O_4$ (MCO); thus, depletion of Cr from the steel and Cr poisoning can be avoided [16-18]. In addition, some coatings, such as Ce, decrease the growth rate of the oxide scale that forms on top of the substrate at high temperatures, thereby increasing the interconnect life-time as less Cr is consumed [19, 20]. A thinner oxide scale also means reduced electrical resistance, which leads to an improvement of the overall power output of the stack. Another important corrosion phenomenon is the dual-atmosphere effect, which entails increased corrosion on the air-facing side of the interconnect if the material is exposed simultaneously to hydrogen on the other side of the interconnect [21]. To make SOFCs commercially attractive, additional research is needed to understand and mitigate the corrosion phenomena, so as to prolong the life-time of the stack and reduce its production cost.

1.2 Aim of this Thesis

The present work focuses on the use of different coatings to mitigate the corrosion phenomena occurring in interconnects when exposed to different SOFC-operating conditions.

The first part of this thesis focuses on novel coatings and the efficiency levels of different deposition process, towards a switch from the state-of-art Ce/Co coating to Cu-based coatings.

Coatings are applied to SOFC interconnects to reduce Cr evaporation and decrease oxide scale growth [10, 14, 22]. One has to keep in mind that interconnects have to be electrically conductive and that applying a coating might increase electrical resistance. In recent years, there has been a focus on spinel coatings owing to their high Cr mitigation rates and high theoretical conductivities [16, 23]. The switch from Co-based coatings to Cu-based coatings could open new avenues for cost reduction, improve safety by avoiding exposition to Co dust, and have a positive geopolitical impact in poorer countries by reducing the use of Co, and thus its extraction [24, 25].

The second part of this thesis discusses the effects of coatings on interconnects when these are exposed to real-life SOFC conditions, i.e., a dual atmosphere. In SOFCs, interconnects experience a dual atmosphere, with hydrogen on the fuel-side and humid air on the air-side. This triggers an increase in the degradation of the FC stack. The effect has been found to be most-prominent at 600℃ [21]. This so-called ‘dual-atmosphere effect’ is not yet fully understood but is under active research [26-32]. To the best of the author's knowledge, this is the first time that protective coatings, designed to inhibit hydrogen diffusion, have been investigated in a dual atmosphere at 600℃.

2 Theory

2.1 Fuel Cell

FCs convert chemical energy into electrical energy through a controlled chemical reaction of a fuel with air. The working principle was discovered independently by William Grove and Christian Friedrich Schönbein in 1830s [22]. They discussed a simple system that converts chemical energy set free during the formation of H_2O, from hydrogen and oxygen, to electrical energy [33]. A fuel cell is composed of an anode, a cathode and an electrolyte. The electrolyte is located between the cathode and anode. The ingenuity of this system is its simplicity. A simple chemical redox reaction allows the reduction of oxygen and the oxidation of hydrogen, allowing the safe conversion of chemical energy to electrical energy. The overall chemical reaction is shown in Equation (2.1):

$$\frac{1}{2}O_2 + H_2 \rightarrow H_2O \tag{2.1}$$

The electrolyte must have high ionic conductivity and poor electronic conductivity. At the anode, the oxidation of hydrogen occurs, and at the cathode, the reduction of oxygen occurs. The electrons are led through an external circuit [34]. The type of electrolyte typically categorises FCs, as this defines the operating temperature, the types of ions conducted, and which fuel can be used for the FC. One example is the PEMFC, which conducts protons and is the most commonly used FC type. As fuel, only high-purity H_2 without contaminating CO can be used. The operating temperature range is 70℃–110℃ [7].

On the other hand, the operating temperature of an SOFC is between 600°C and 900°C, which means that it does not need a noble metal catalyst and can work with a wide variety of fuels, such as methane or hydrogen. The high temperature entails a slower start-up time compared to the PEMFC, but also increased corrosion of certain components [10, 22]. Given the slow start-up, the two technologies can be applied in various ways. While PEMFCs are considered mainly for mobile applications and transportation purposes, SOFCs are mainly considered for Auxiliary Power Units (APUs) in trucks, stationary applications such as back-up power in data centres, and in CHP units in residential applications [34, 35]. The necessity to operate at high temperature also has some advantages, as the extra heat can be collected and used to heat hot water systems in building (for example), thereby increasing the overall efficiency. One advantage that SOFCs have over PEMFCs is their high-level efficiency. While PEMFCs achieve up to 50% efficiency [7], SOFCs reach efficiencies of >60% and have potential overall efficiencies of 90% if the system exploits the exhaust heat in CHP units [36].

The SOFC technology holds promise for the future as the system can be used in reverse mode, in the form of a Solid Oxide Electrolyser Cell (SOEC). The SOEC can produce green H_2 as it emerges as the new sustainable fuel for the future and is attracting increasing interest from different fields worldwide. While this work focuses on SOFCs, most of the acquired knowledge is expected to be equally applicable to SOECs [37]. The SOFC will be described in more detail in the next section.

2.2 Solid Oxide Fuel Cell

The SOFC is based on a ceramic electrolyte that is permeable to O^{2-} ions. Figure 2a shows the working principle of an SOFC that uses H_2 as the fuel. The oxidation of H_2 into H_2O occurs at the anode [Equation (2.2)]. The electrons set free during the oxidation are transferred through an external circuit to the cathode, where O_2 is reduced to O^{2-} [Equation (2.3)]. The O^{2-} ions can then diffuse through the solid electrolyte to the anode, where they react with the protons and form water. When hydrogen is used as the fuel, the overall reaction is as shown in Equation (2.4).

Oxidation reaction: $$H_2 + O^{2-} \rightarrow H_2O + 2e^- \quad (2.2)$$

Reduction reaction: $$\frac{1}{2}O_2 + 2e^- \rightarrow O^{2-} \quad (2.3)$$

Overall reaction: $$\frac{1}{2}O_2 + H_2 \rightarrow H_2O \quad (2.4)$$

Because of thermodynamics limitations, one cell can deliver up to 1.2 V [38]. Therefore, multiple cells have to be stacked and electrically connected in series with interconnects to form an FC stack (Figure 2b). Due to the high operating temperatures, all the components must have a similar Thermal Expansion Coefficient (TEC), to avoid thermal stresses during start-up and shut-down.

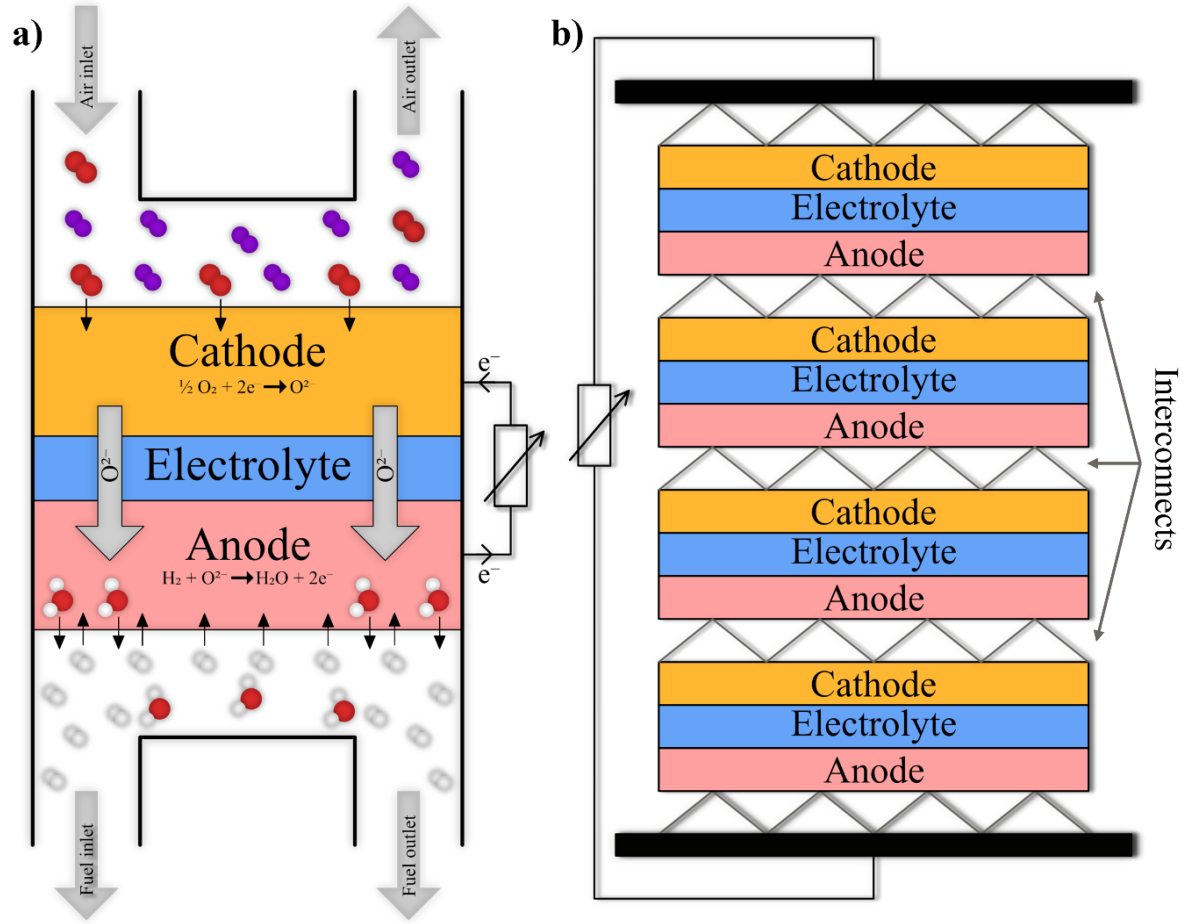

Figure 2: Solid oxide fuel cell: a) Operating principle; and b) Fuel cell stack. Based on [39]

2.2.1 Cathode

The cathode must be stable at high temperatures and in oxidising atmospheres. The material must be porous to allow a good gas flow and have high electron conductivity to maintain good catalytic activity for oxygen reduction [Equation (2.3)] [40]. A frequently used cathode material is Sr-doped $LaMnO_3$ (LSM). The addition of Yttria-stabilised zirconia (YSZ) increases the oxygen ion conductivity [41, 42]. The most commonly used cathode material in Intermediate-Temperature Solid Oxide Fuel Cells (IT-SOFCs) is $(La,Sr)(Co,Fe)O_3$ (LSCF) [43, 44].

2.2.2 Electrolyte

The electrolyte must be stable in both anode and cathode atmosphere and have sufficiently high ionic conductivity (>0.05 $S \cdot cm^{-1}$) and low electron conductivity. Moreover, the material must be shaped into a thin, strong film that allows no gas leaks. Commonly used electrolyte material at high temperatures is Yttria-stabilised zirconia (YSZ) (>700°C). It has been suggested that zirconia (ZrO_2) doped with 8-10 mol% yttria (Y_2O_3) is the optimal option for ion conduction [7]. For applications at lower temperatures, Gadolinia-doped ceria (GDC) is a popular electrolyte which display higher conductivity (two order of magnitude) than YSZ. However, GDC has a higher electronic conductivity at lower oxygen pressures (anode side), leading to higher leakage current decreasing the power output [45].

2.2.3 Anode

Similar to the cathode, the anode materials must be stable at high temperatures. However, in contrast to the cathode material, the anode materials must be stable also in reducing atmospheres. The material also needs to be a good electron conductor, exhibit good catalytic properties for oxidation of the fuel [see Equation (2.2)], and be porous to allow sufficient gas flow. A common anode material used is a porous cermet (ceramic-metallic composite) that consists of a mixture of nickel and YSZ (Ni-YSZ) [46]. This mixture of the electrolyte material and a material with high electron conductivity, allows for a good TEC match between the anode and electrolyte and ensures pore formation [47].

2.2.4 Interconnect

The interconnects (bipolar plates) connect single cells to form an FC stack (Figure 2b). Their main functions are to connect electrically the anode to the cathode of the neighbouring cell, and to separate the anode and cathode gases. Interconnects need to exhibit high electronic conductivity, low ionic conductivity, high mechanical strength, high thermal conductivity, and chemical stability regarding other cell components and in reducing and oxidising atmospheres [48].

In the past, efforts to develop interconnects primarily focused on ceramic oxides with a

perovskite structure as the interconnect material. Only a few oxides, e.g., lanthanum chromite ($LaCrO_3$), satisfied the rigorous requirements. However, these oxides are all very costly and have several disadvantages, such as low formability.

Due to a decrease in the operating temperature from 1,000°C to <800°C, as a result of improvements in electrolytes and electrode materials, current research is focusing on metallic interconnects instead of ceramic interconnects. Several candidates have been studied, but FSS with a chromium content in the range of 16%–22% are the most commonly used. The chromium oxide (Cr_2O_3) layer formed at high temperature is a protective oxide. The protective oxide property of Cr_2O_3 ensures sufficient corrosion resistance for the FSS at the operating temperature. The semiconducting property allows for sufficiently high electrically conductivity of the interconnect at the operating temperature. Besides the above-mentioned required properties, metallic interconnects are easier to shape, have good workability, and are cheaper than ceramic interconnects.

2.3 Oxidation of Metals

When most metals, are exposed to oxygen-containing atmospheres, oxidation phenomena occur, according to Equation (2.5):

$$\mathrm{xM(s)} + \frac{y}{2} O_2\mathrm{(g)} \leftrightarrow M_x\mathrm{O}_y\mathrm{(s)} \tag{2.5}$$

The metallic surface will almost instantly be covered by an oxide layer (metal oxide) that prevents direct metal-oxygen contact. For further metal oxidation to occur, one of the reactants, the metal or oxygen, must diffuse through the oxide scale. Usually, both phenomena happen simultaneously, although one is dominant. The speed with which a metal can oxidise is often determined by the rate at which ions can diffuse through the oxide scale.

2.3.1 Thermodynamics

To determine if a metal is stable under certain conditions, e.g., temperature, atmosphere, etc., the Gibbs free energy of a system can be calculated according to Equation (2.6):

$$G = H - TS \tag{2.6}$$

where *G* is the Gibbs free energy, *H* is the enthalpy, *T* is the temperature, and *S* represents the entropy.
For systems with $\Delta G < 0$, the reaction is spontaneous, whereas systems with $\Delta G = 0$ are in equilibrium, and the reaction is thermodynamically impossible for systems with $\Delta G > 0$. When a metal oxidises, three phases are essential: the metal, the metal oxide, and the gas phase. To predict whether a metal will oxidise, Equation (2.7) can be used:

$$\Delta G = \Delta G^0 + RT \ln \frac{a_{(MxOy)^{(s)}}}{a_{M(s)}^{x} \times a_{O_{2(g)}}^{\frac{y}{2}}} \quad (2.7)$$

where ΔG^0 is the change in Gibbs free energy under standard conditions, R is the gas constant, T is the absolute temperature, and a_x is the thermodynamic activity of a species z. The activity for a pure solid can be approximated to 1, while for a gas, the activity can be assumed to be equivalent to the partial pressure (pO_2). Thus, the Gibbs free energy at a specific temperature can be expressed as a function of the oxygen partial pressure, according to Equation (2.8):

$$\Delta G = \Delta G^0 + RT \ln \frac{1}{pO_2^{\frac{y}{2}}} \quad (2.8)$$

As per Equation (2.8), two parameters allow the determination of whether a metal or an oxide is stable under certain conditions: the temperature T; and the oxygen partial pressure pO_2. The domain of stability of metal oxides at different temperatures and at different partial pressures are shown in the Ellingham diagram (Figure 3) [49].

Thermodynamics show if the formation of corrosion products is energetically favoured, following the chemical reaction: A (in alloy) + BO → AO + B (in alloy). Thermodynamics can be considered as the driving force for the degradation of metals and alloys in corrosive atmospheres. Alloys are composed of more than one metal or non-metallic elements (carbon in the case of steels) that are not stable in a reactive gaseous atmosphere.

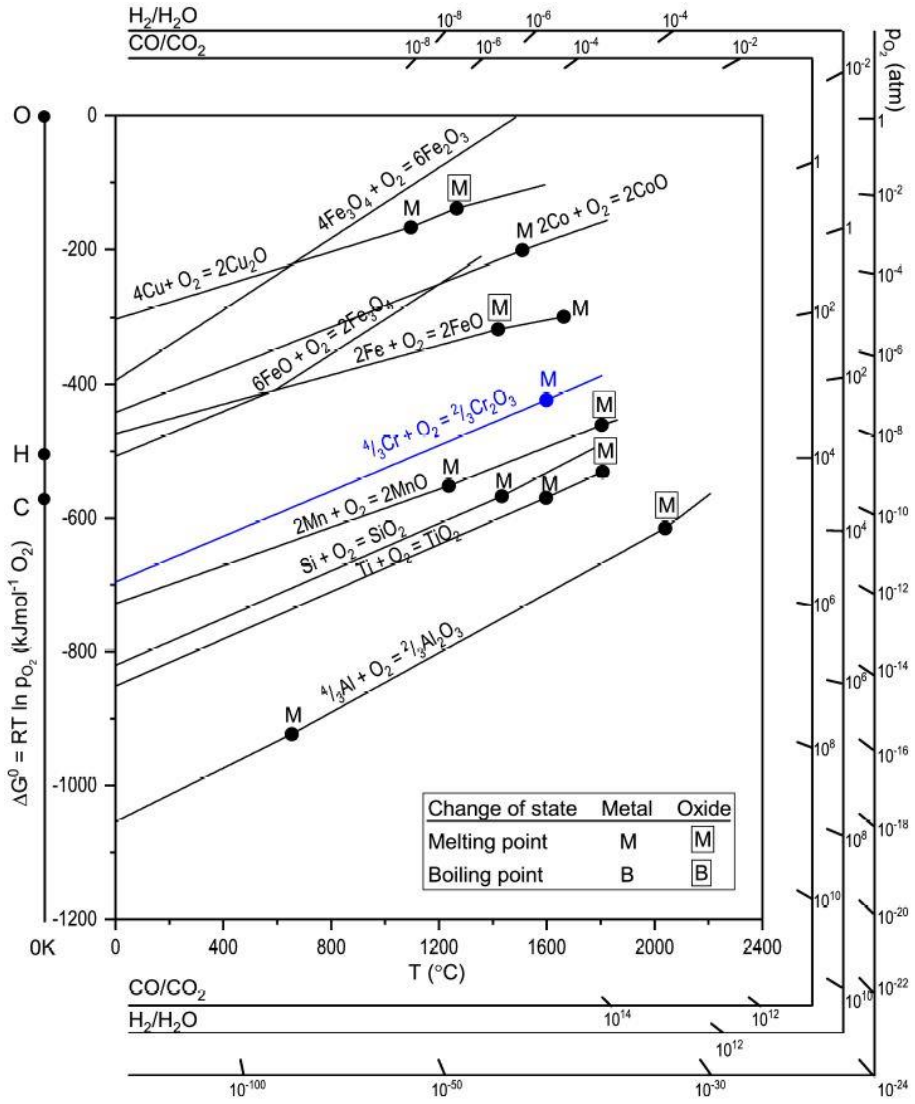

Figure 3: Ellingham diagram for the selected oxides [50, 51].

2.3.2 Kinetics

Kinetics are used to understand the reaction mechanism and determine the reaction's rate-limiting step. There are three different ways to analyse the rate of metal oxidation, and these entail measuring: (a) how much metal was consumed; (b) how much oxygen was consumed; and (c) how much oxide was formed. The latter is the most commonly used technique because it is experimentally straight-forward to measure the mass gain of the sample.

To evaluate the kinetics, different rate laws can be formulated. The three most widely used are: (a) linear law; (b) logarithmic law; and (c) parabolic law (Figure 4). That being said, not all reactions follow these laws, and deviations or a mixture of different rate laws are common. Nevertheless, the rate laws can give some information about the protective behaviour of an oxide layer [49].

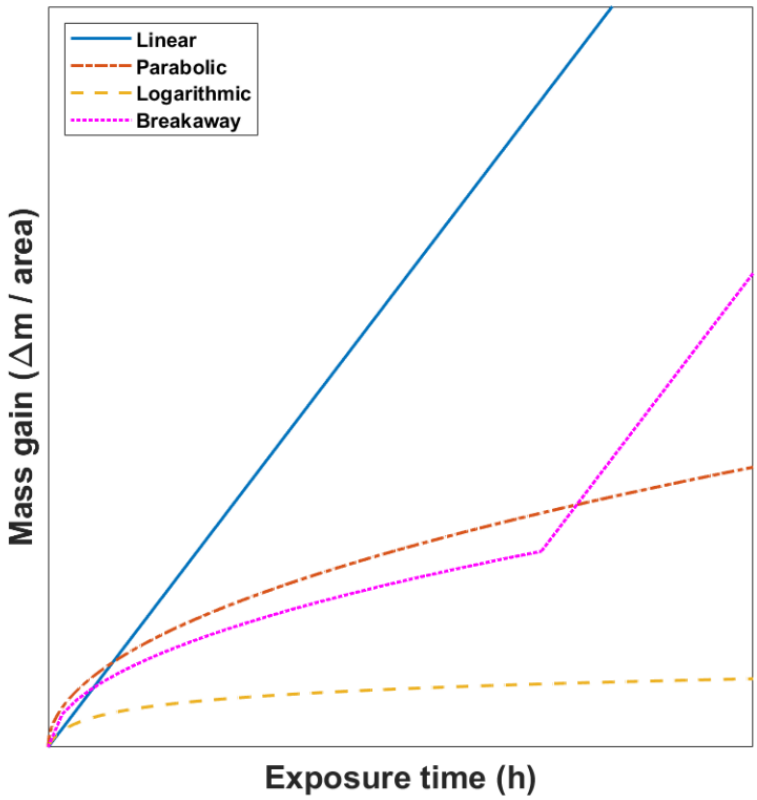

Figure 4: Typical metal oxidation regimes.

2.3.2.1 Linear Rate Law

When the mass gain as a function of time is increasing linearly, it can be described according to Equation (2.9):

$$\Delta m = k_l t + C \tag{2.9}$$

where Δm is the mass change, k_l is the linear rate constant, t is the exposure time, and C is an integer. This behaviour is commonly seen under conditions where surface or phase-boundary processes are the rate-determining steps. This phenomenon is observed if the oxide scale is porous or very thin. A linear mass gain behaviour may also be observed if the thickness of the protective layer is constant [50].

2.3.2.2 Logarithmic Rate Law

When the mass gain as a function of time is behaving logarithmically, it can be described according to Equation (2.10):

$$\Delta m = k_{log} \log(t + t_0) + C \tag{2.10}$$

where Δm is the mass change, k_{log} is the logarithmic rate constant, *t* is the exposure time, and *C* is an integer.
This rate law is observed at low temperatures (< 400°C) and for very thin oxide layers (up to 4 nm in thickness). The rate-determining step for this rate law is not yet fully understood. Different hypotheses have been proposed, such as the transport of electrons from the metal to the oxide-gas interface through quantum mechanical tunnelling through the oxide layer. This mechanism is only possible for thin oxide scales [50].

2.3.2.3 Parabolic Rate Law

Parabolic behaviour is usually associated with Carl Wagner's oxidation model for parabolic rate growth [52]. When the mass gain as a function of the time is parabolic it can be described using Equation (2.11):

$$\Delta m^2 = k_p t + C \tag{2.11}$$

where Δm is the mass gain, k_p is the parabolic rate constant, *t* is the exposure time, and *C* is an integer. This behaviour is observed when solid-state diffusion transport of the reactants or electrons through the oxide scale (lattice transport) is the rate-determining step. Carl Wagner assumed that:

- the scale is continuous, dense, and well-adherent;
- the composition of the oxide is constant throughout the scale;
- the scale growth is driven by solid-state diffusion;
- thermodynamic equilibrium exists at the oxide/gas interface and the metal/oxide interface; and
- oxygen solubility in the metal is negligible.

The thicker the oxide layer, the slower the diffusion through the scale. The resulting oxide scales are often described as protective oxide scales [20].

2.3.2.4 Break-away oxidation

Break-away oxidation refers to a specific and rapid mass gain behaviour. Break-away oxidation is frequently observed when a protective oxide scale is transformed into a non-protective oxide scale. There are two main reasons why this happens:

a) Mechanically induced chemical failure (MICF)
b) Intrinsic chemical failure (InCF)

In the case of MICF, the oxide scale reaches a critical thickness, at which point cracking, the rupturing of the oxide, or even spallation reduces the thickness of the protective layer. This leads to direct contact between the substrate and the oxygen. Three outcomes are possible:

1) If the cracks and rupture formation stay below a critical value and the protecting oxide-forming element, e.g., Cr or Al, is not depleted, a continuous protective oxide scale forms (self-healing) [53].
2) If the substrate is locally depleted of the protective oxide-forming element, e.g., Cr or Al, a non-protective, fast-growing Fe-rich oxide forms [54].
3) If the rates of cracking and rupturing are high, a non-protective oxide scale can form even if the substrate is not depleted of the protective oxide-forming elements.

In the case of InCF, an element that forms the protective oxide scale is depleted in the alloy, e.g., the depletion of Cr. The formation of a protective oxide is then thermodynamically less-favourable, so a non-protective, fast-growing oxide (e.g., Fe-rich oxide) may form [53].

2.3.3 Oxide Scale Growth

The growth of an oxide layer follows three distinct steps, as depicted in Figure 5.

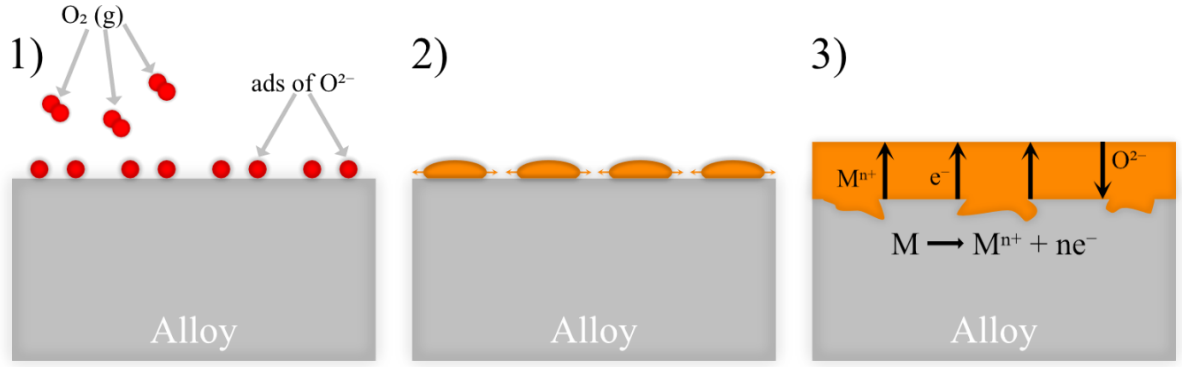

Figure 5: Oxidation steps on a metal substrate [50]: 1) O_2 adsorption; 2) Oxide nucleation; 3) Continuous oxide scale growth.

In Step 1, oxygen molecules from the atmosphere are adsorbed onto the metal surface, thereby creating a charge transfer and forming O^{2-} and M^{n+}. During Step 2, the formation of metal oxide nuclei occurs at the metal surface. The growth of the metal oxide proceeds until a continuous layer covers the entire surface (Step 3). Once formation of the continuous layer is completed, solid-state diffusion through the oxide scale is required for further oxidation. Protective oxide scales, such as Cr_2O_3, are distinguished by their low porosity, and low ion diffusivity. All of these properties support a slow-growing oxide scale. At high temperatures, the first two steps

happen very rapidly, and the third step is considered the rate-determining step for continued scale growth [20].

2.3.4 Defects in Oxide Scales

Depending on the type of ionic diffusion process occurring in the scale, the oxide growth direction will be either inwards or outwards. If oxygen diffusion predominates the oxide will grow inwards. However, if the diffusion is dominated by metal ion transport, the scale will grow outwards. The different ways in which an oxide can grow are depicted in Figure 6. The types of defects in oxide crystals determine the dominant mode of transportation, e.g., anionic or cationic. Oxide crystals consist of an ordered array of cations and anions. However, due to different factors, oxide crystals contain defects of various types depending on the elements that they contain. The defect structure depends on the temperature, the oxygen partial pressure, and the energy of formation of a specific defect in a lattice [55]. Oxides are classified according to the electrical charge that is transported. If an oxide carries an electrical charge through electrons in the conduction band, it is an *n-Type* oxide. Conversely, if an oxide carries an electrical charge through electron holes in the valence band, it is a *p-Type* oxide [20].

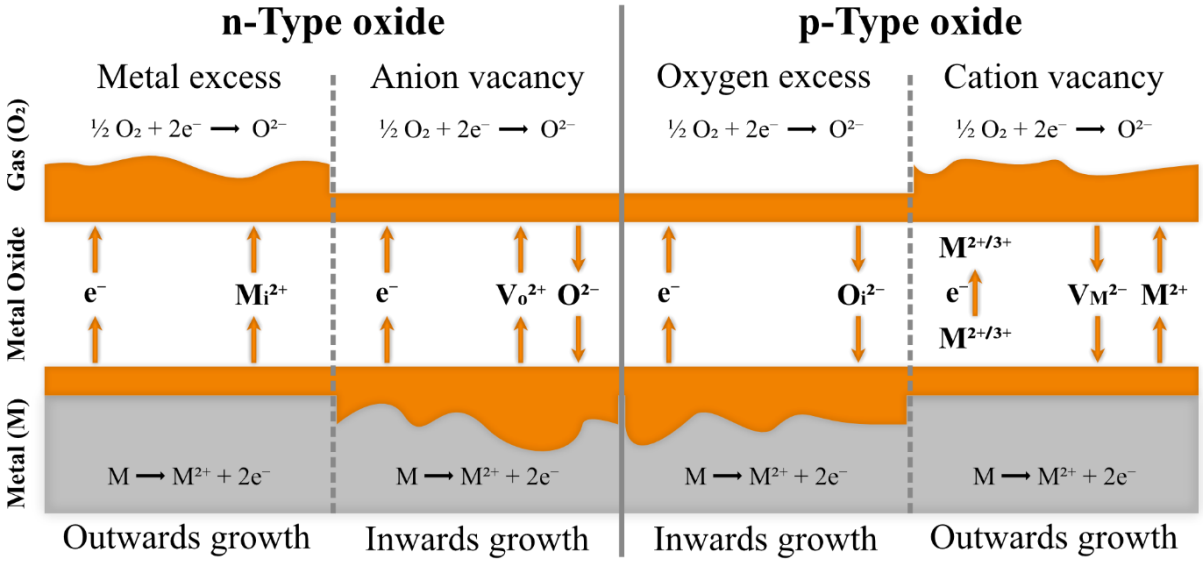

Figure 6: Simplified model of diffusion-controlled oxidation in a metal oxide. Adapted from [56].

The n-Type oxides are divided into two groups:

1) Metal excess oxides: contain interstitial cations in the lattice, balanced out by an equal number of electrons in the conduction band. Cations are transported through the lattice by hopping from interstitial sites.
2) Oxygen vacancies oxides: contain anion vacancies, which result in positive charges that are compensated by conduction band electrons [20, 50].

The p-Type oxides are also divided into two groups:

1) Oxygen excess oxides: contain interstitial anions in the lattice balanced out by electron holes in the valence band. Excess ions can diffuse through the oxide by changing interstitial sites.
2) Metal vacancies oxides: contain cation vacancies that result in negative charges that are compensated by electron holes in the valence band. Ion vacancies can also diffuse in the lattice, leading to the conduction of the vacant ions species [20, 50].

2.3.5 Chromium(VI) Evaporation

Cr-containing alloys are design to form a protective, slow-growing, and dense Cr_2O_3 layer when exposed to high temperatures. Nonetheless, in certain atmospheres, other volatile Cr species can form. In a dry atmosphere, gaseous CrO_3 will be formed according to Equation (2.12):

$$Cr_2O_3(s) + 1.5\ O_2\,(g) \rightarrow 2\ CrO_3\,(g) \qquad (2.12)$$

The requirements for significant CrO_3 formation are: high temperature (T~1,000°C), and high O_2 partial pressure [50].

Another volatile Cr-species, $CrO_2(OH)_2$, will form in water vapour-containing atmospheres. Several authors [57, 58] have reported that $CrO_2(OH)_2$ is the most-abundant volatile Cr species in the air when water vapour is present even in small amount. $CrO_2(OH)_2$ is formed according to Equation (2.13):

$$Cr_2O_3(s) + 2\ H_2O + 1.5\ O_2(g) \rightarrow 2\ CrO_2(OH)_2\ (g) \qquad (2.13)$$

Furthermore, the rate of Cr evaporation is dependent upon the gas flow. Figure 7 shows the effect of the gas flow on the Cr evaporation of an FSS that contains 21 wt% Cr (Sanergy HT) at 850°C in air with 3% H_2O vapour. At low flow rates, the Cr evaporation is proportional to the rate flow, whereas a plateau appears at a higher flow rate (≈ 6,000 sml·min^{-1}). In this range, the Cr evaporation is independent of the air-flow rate [60].

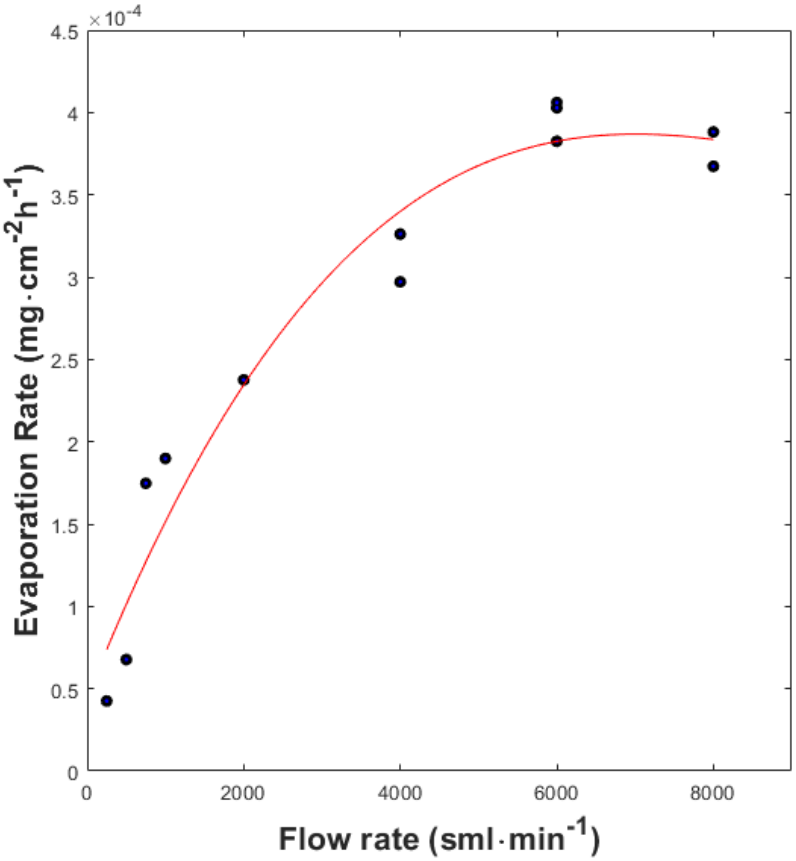

Figure 7: Rate of Cr vaporisation as a function of the gas flow rate at 850°C in air + 3% H_2O on the Sanergy HT substrate. Source: [60].

2.4 Corrosion of Interconnects

Interconnects are an essential part of every FC stack, as they connect electrically the cells within a stack. When exposed to high temperatures, interconnects are expected to form a protective oxide layer, i.e., Cr_2O_3. While alloys that form an Al_2O_3 layer would be the best candidates due to the presence of an adherent and dense oxide, their insulating properties exclude them from being used. On the other hand, Cr_2O_3-forming alloys suffer from continuous Cr(VI) evaporation, although the semi-conductive behaviour of the chromia makes it the best candidate for interconnects. Most researchers are, therefore, focusing on chromia-forming steels.

2.4.1 Stainless steels

Different types of stainless steel exist, and they are classified according to their crystalline structure. The most common types are ferritic and austenitic stainless steels. Their crystal structure is depicted in Figure 8. Their respective TEC is between $11.5 \cdot 10^{-6}\ K^{-1}$ and $14 \cdot 10^{-6}\ K^{-1}$ for ferrite and $18 \cdot 10^{-6}\ K^{-1}$ and $20 \cdot 10^{-6}\ K^{-1}$ for austenite. Because of the TEC of ferrite matches better the other components of the fuel cell (10 - $12.5 \cdot 10^{-6}\ K^{-1}$), research have mainly focused on ferritic stainless steels [48, 61].

1) Ferritic stainless steels, which have a crystalline body-centred cubic (BCC) structure (see Figure 8a).
2) Austenitic stainless steels, which have a crystalline face-centred cubic (FCC) structure (see Figure 8b).

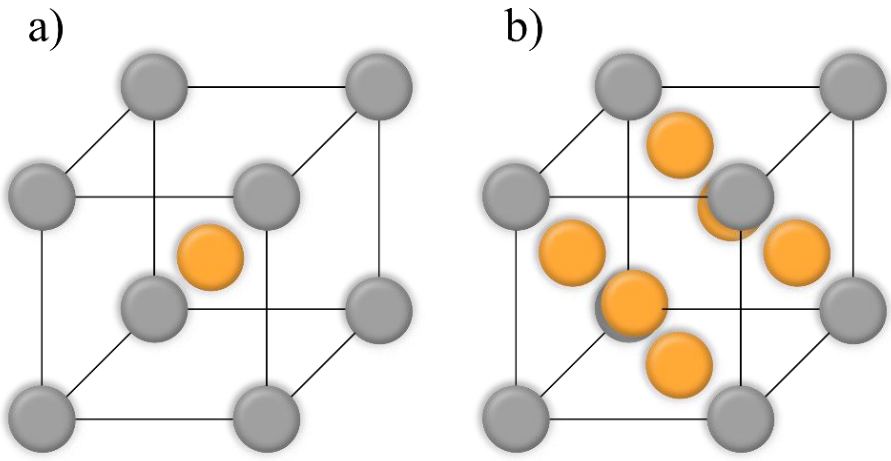

Figure 8: Schematic of the: a) body-centred cubic; and b) faced-centred cubic crystalline structures.

Current state-of-the-art interconnect materials are Ferritic Stainless Steel (FSS). Yet, these interconnects deteriorate over time due to the harsh conditions that prevail during FC operation.

2.4.2 Ferritic Stainless Steels as Interconnects

FSS are the most common choice of interconnect material due to their TEC, which matches the

TEC values of the other parts of the FC, especially the anode, more closely than the TEC values of the austenitic stainless steels [48, 62]. FSS commonly contain between 10% and 26% Cr. A Cr content of 13% is necessary to retain the ferritic structure at all temperatures (Figure 9). The most-suitable forms are steels with more than 16% Cr. A too-high Cr content in the alloy increases the risk for the formation of a brittle σ-phase or the depletion of Cr from the steel [63].

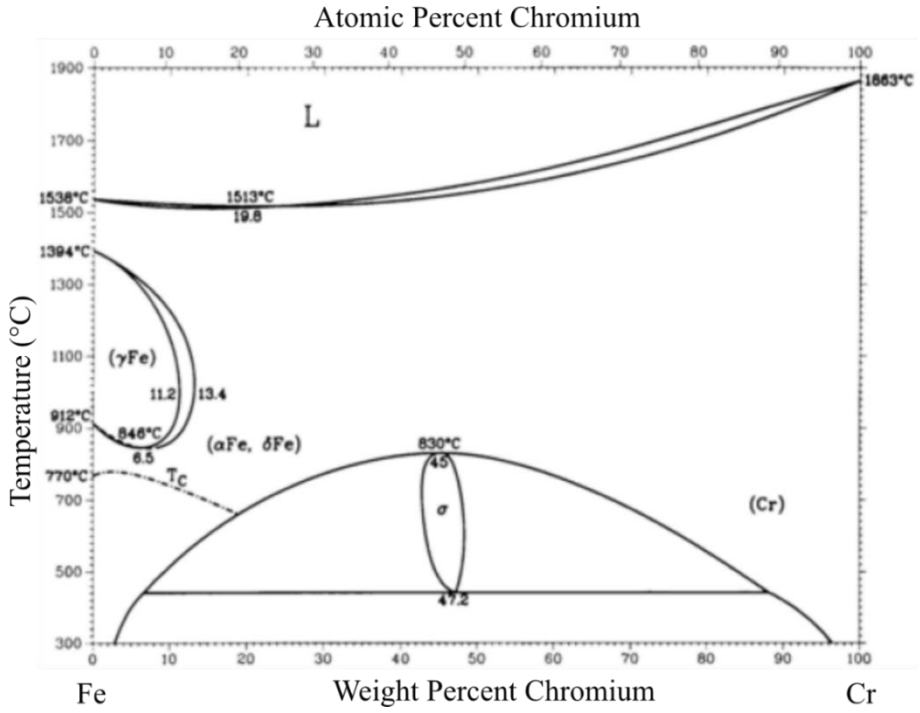

Figure 9: Binary-phase Fe-Cr diagram taken from [64]. α-Fe and δ-Fe have a BCC crystalline structure, i.e., ferritic phase, and γ-Fe has an FCC crystalline structure, i.e., austenitic phase.

Specific alloys have been developed for use as interconnects, e.g., Crofer 22 APU, Crofer 22 H, and Sanergy HT. These alloys have a Cr content of at least 21%, as well as other alloying elements such as Mn and reactive elements, which are added to avoid specific issues [65], as will be discussed later in the thesis. These alloys are specifically designed for use as interconnects in FCs, so they are relatively expensive. Therefore, cheaper materials are being investigated, for example, AISI 441 and AISI 430 with Cr contents in the range of 16%–20% [61, 65-68]. These alloys are best-suited for lower SOFC operating temperatures (600°C–700°C), since at higher temperatures, the Cr content might not be sufficient [66, 69]. The following different alloying elements are often found in the chemical compositions of interconnect materials, and their benefits are discussed.

2.4.2.1 Mn to reduce Cr(VI) evaporation

Different issues during FC operation are linked to Cr evaporating from the interconnect: (a) Cr-deficiency in the interconnect; and (b) Cr-poisoning of the cathode. Adding small amounts of manganese (up to 0.5 wt%) as an alloying element can help to reduce Cr(VI) evaporation by

a factor of 2–3. This addition results in the formation of a $(Cr,Mn)_3O_4$ top layer with a continuously growing Cr_2O_3 layer underneath [65, 70]. Nevertheless, coatings will be used to further mitigate the Cr evaporation.

2.4.2.2 Other alloying elements (Si, Nb, Mo or W and Ti)

Silicon is a remnant product of stainless steel manufacturing process. However, in the context of the use of such stainless steels as interconnects, it could be an issue if a continuous SiO_2 scale forms. This scale acts as an insulator and, thus, leads to a significant increase in electrical resistance, which is detrimental for interconnects. Si has also been reported to be detrimental for adhesion between the oxide scale and the metal and causes the Cr_2O_3 layer to spall off during thermal cycling [15]. Therefore, alloys that are designed specifically for use as interconnects either employ a specific vacuum induction melting process to avoid Si contamination or add other alloying elements to bind Si. Crofer 22 APU employs the first method, while Crofer 22 H and Sanergy HT use the latter approach of adding alloying elements such as Nb, Mo, and W, resulting in the formation of laves phases. These intermetallic precipitates, which consist of $(Fe,Cr)_2(Nb,W,Mo)$, have the positive side-effect of increasing the hardness and the creep strength of the steel [71, 72].

The presence of titanium (Ti) in the alloy will result in internal oxidation. This phenomenon can have a beneficial effect, as the internal oxide zone may strengthen the near-oxide scale area and prevent the oxide scale from buckling [73]. The presence of Ti in the alloy reduces the contact resistance of the oxide scale by doping the Cr_2O_3 scale [74]. This doping effect also increases Cr diffusion, which results in increased growth of the chromia scale [74]. If the concentration of Ti is too high, spallation of the scale may occur [73].

2.4.2.3 Reactive elements (Ce, Hf, La, and Y)

Reactive elements (REs), such as Ce, Hf, La, and Y, are known to be highly beneficial for the overall oxidation behaviour of the alloy [75-77]. The most-common effects of the reactive elements are:

- Increased oxide-scale adhesion and increased resistance to spallation,
- Decreased oxide scale growth,
- Modification of the growth mechanism of the oxide scale,
- Selective oxidation of the alloy.

The mechanisms through which REs work are not fully understood. Nevertheless, there is a general consensus that the addition of REs changes the growth mechanism of the oxide scale. The most common theory suggests that non-doped Cr_2O_3 growth is due to predominant outward diffusion of the metal cations. However, when the Cr_2O_3 scale is doped with an RE, the outward diffusion of the metal cations is inhibited by the segregation of the RE at the grain boundaries. Consequently, the low flux of oxygen ions becomes the predominant mechanism. The growth mechanism shifts from predominantly outward diffusion of Cr ions to inward diffusion of oxygen ions, which slows oxide scale growth and improves oxide scale adhesion [78-82].

Specific alloys, such as Crofer 22 H, Crofer 22 APU, and Sanergy HT, have REs incorporated into the bulk during the manufacturing process. However, this incorporation increases the overall production cost. An alternative way of adding REs is through coating [67, 83]. Although coatings with REs improve oxidation resistance, Cr evaporation is not reduced [67]. Therefore, RE coatings must be combined with a second coating that mitigates Cr evaporation, such as a Co-Mn spinel or a metallic Co [84, 85].

2.4.3 Coatings to Mitigate Cr(VI) Evaporation

Adding alloying elements to the steel only has a limited effect on these degradation mechanisms. Therefore, additional protection is needed. Nowadays, coatings are commonly used to reduce Cr(VI) evaporation. Those coatings can be applied to the steel using different techniques, such as spray-drying, dip-coating, screen printing, aerosol spray deposition, plasma spraying, and PVD [86-89].

The main types of coatings are:

a) *Perovskite-type coatings:* possess high electrical conductivity and good compatibility with the other FC parts [90]. However, a thick coating is required to decrease the oxidation rate significantly, and the adhesion of the coating to the substrate is often poor. In addition, the extent of mitigation of Cr evaporation by a perovskite-type coating is limited [14, 91, 92].

b) *Spinel-type coatings:* the most-often used coating type, as it shows very high efficiency in mitigating Cr evaporation. The spinel coating MnCo-oxide (MCO) offers good Cr retention [16, 17] and high electrical conductivity [23].

Besides applying the oxide coating directly, a conversion coating route can be utilised [18]. For this technique, the alloy is coated with a metal, such as Co or Cu, which is then oxidised at a high temperature to form the corresponding metal oxide. For example, to achieve the MCO coating via the conversion coating route, Co is first oxidised to Co_3O_4 and then enriched with Mn through outward diffusion of Mn from the steel substrate [18, 67]. The advantages of conversion coatings are that thin and dense coatings can be achieved. The process is highly cost-effective because large-scale, roll-to-roll coating applications are possible. It has been shown that REs can also be good coating materials, since they decrease the oxide scale growth rate and improve scale adherence [75, 93]. Ce/Co coating combines the positive effects of MCO conversion coatings and RE coatings. Today, a 10-nm-thick Ce coating underneath a 600-nm-thick Co coating is considered the state-of-the-art coating arrangement [84, 94, 95].

2.4.4 Electrical Conductivity of Oxide Scales

The main role of an interconnect is to electrically connect the cells within an FC stack. The growth of a poorly conducting oxide scale on the interconnect during operation significantly increases the overall resistance. To describe the electrical conductivity of an oxide, the sum of the conductivities of the electronic and ionic charge carriers is calculated according to Equation (2.14):

$$\sigma_{total} = \sigma_{ionic} + \sigma_{electronic} \quad (2.14)$$

where σ_{total} is the electrical conductivity, σ_{ionic} and $\sigma_{electronic}$ are the respective conductivities and $\sigma_{electronic}$ is defined as the sum of the conductivity of the electrons σ_e and holes σ_h in Equation (2.15) [50]:

$$\sigma_{electronic} = e(nv_e + pv_h) \quad (2.15)$$

where *n* and *p* are the concentrations of electrons and holes, respectively, and v_e and v_h are the electrons and hole mobilities, respectively [50]. In the same reasoning, σ_{ionic} is the sum of the anion (σ_a) and cation (σ_c) conductivities according to Equation (2.16):

$$\sigma_{ionic} = \sigma_a + \sigma_c \quad (2.16)$$

Both the mobility and the concentration terms are temperature-dependent. The mobility v_e of electrons decreases with higher temperatures while the mobility of ions increases with higher temperatures. This leads to a positive temperature-dependency for the oxide as the increased charge carrier concentration and mobility of ions compensate for the decreased mobility of electrons. In the case of a metallic conductors, for which conductivity decreases with increasing temperature, the decreased mobility of electrons are not compensated by the increased charge carrier concentration, resulting in a decrease in conductivity [50].

The temperature-dependence of the conductivity of oxide scales can also be expressed using the Arrhenius equation (2.17) [50]:

$$\sigma = \sigma_0 \times \exp\left(\frac{-E_a}{R \times T}\right) \quad (2.17)$$

where σ_0 is a pre-exponential factor, *R* is the ideal gas constant, *T* is the absolute temperature, and E_a is the activation energy.

Due to the complexity of the oxide scales, the overall conductivity is measured rather than the conductivity of one oxide. Usually, the resistance of an oxide scale is measured, which commonly is expressed as Area-Specific Resistance (ASR) and can be described according to Equation (2.18):

$$ASR = R \times A \quad (2.18)$$

where *R* is the resistance, and *A* is the area. *R* can also be expressed according to Equation (2.19):

$$R = \frac{1}{\sigma} \times \frac{L}{A} \quad (2.19)$$

where σ is the conductivity, *L* is the oxide thickness, and *A is* the area.

2.4.4.1 Electrical conductivity of the chromia scale

Since interconnects are mainly constructed of FSS, the electrical properties of the growing chromia scale have a major impact on the overall conductivity of the interconnect. Cr_2O_3 is known to be an intrinsic semiconductor at high temperatures (>1,000℃). However, it exhibits an extrinsic semiconductor behaviour at lower temperatures and relies mainly on dopants [96, 97]. Below 1,000℃, chromia acts as a p-Type semiconductor, and its conductivity depends on the oxygen partial pressure [97]. Even though the primary doping mechanism for Cr_2O_3 is unclear, it has been shown to have a dual semiconductor behaviour, expressing n-Type and p-Type semiconducting behaviours depending on the types of defects that it contains [98]. Researchers [98, 99] have attributed this dual semiconducting behaviour to the presence of an n-Type internal subscale and n-Type or p-Type outer scale at temperatures >800℃, depending on the oxygen partial pressure.

2.4.4.2 Electrical conductivity of spinels

As stated in Section 2.4.3, spinels are the primary coatings used in interconnects. Therefore, it is crucial to understand how electrons are transported in a spinel structure and which spinels are highly conductive. It is commonly believed that electrons jump from one octahedral site to another, and if cations of mixed-valence occupy the sites, the electrical conductivity is increased [23, 100]. This explains why Cr-containing spinels often exhibit high resistance because, in the spinel structure, the only possible valence of Cr is Cr^{3+}, which tends to occupy the octahedral sites [101]. *Petric et al.* [23] conducted an extensive study of the conductivities of different spinels and discovered that spinels that contain Mn, Co or Cu have the highest conductivities.

Table I: Specific conductivity values for different spinels measured at 800℃, except where noted. Source: [23]. The conductivities are given in $S \cdot cm^{-1}$.

	Mg	**Mn**	**Co**	**Ni**	**Cu**	**Zn**
Al	$MgAl_2O_4$ $\sigma = 10^{-6}$	$MnAl_2O_4$ $\sigma = 10^{-3}$	$CoAl_2O_4$ $\sigma = 10^{-5}$	$NiAl_2O_4$ $\sigma = 10^{-4}$	$CuAl_2O_4$ $\sigma = 0.05$	$ZnAl_2O_4$ $\sigma = 10^{-6}$
Cr	$MgCr_2O_4$ $\sigma = 0.02$	$\mathbf{Mn_{1.2}Cr_{1.8}O_4}$ $\boldsymbol{\sigma = 0.02}$	$CoCr_2O_4$ $\sigma = 7.4$	$NiCr_2O_4$ $\sigma = 0.73$	$CuCr_2O_4$ $\sigma = 0.40$	$ZnCr_2O_4$ $\sigma = 0.01$
Mn	$MgMn_2O_4$ $\sigma = 0.97$	Mn_3O_4 $\sigma = 0.10$	$CoMn_2O_4$ $\sigma = 6.4$	$NiMn_2O_4$ $\sigma = 1.4$	$\mathbf{Cu_{1.3}Mn_{1.7}O_4}$ $\boldsymbol{\sigma = 225}$ (**750**℃)	$ZnMn_2O_4$
Fe	$MgFe_2O_4$ $\sigma = 0.08$	$MnFe_2O_4$ $\sigma = 8.0$	$CoFe_2O_4$ $\sigma = 0.93$	$NiFe_2O_4$ $\sigma = 0.26$	$CuFe_2O_4$ $\sigma = 9.1$	$ZnFe_2O_4$ $\sigma = 0.07$
Co		$\mathbf{MnCo_2O_4}$ $\boldsymbol{\sigma = 60}$	$\mathbf{Co_3O_4}$ $\boldsymbol{\sigma = 6.7}$			

2.4.5 Dual-Atmosphere Effect

Under fuel cell conditions, interconnects are exposed to two different atmospheres in parallel (Figure 10). One side of the interconnect is exposed to air (air-side), while the other side is exposed to H_2 (fuel-side).

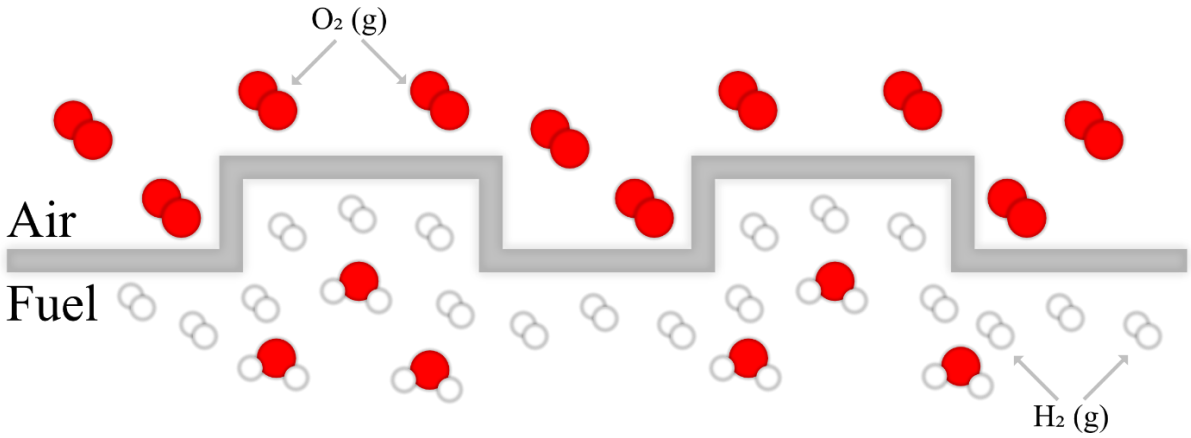

Figure 10: Interconnect exposed under dual-atmosphere conditions.

Many studies [21, 27, 31, 32, 102, 103] have focused on the effect of the dual atmosphere on the corrosion behaviours of FFS interconnects. Most of them have found increased corrosion on the air-side when hydrogen is used as the fuel. The effect of hydrogen is still unclear, and a lot of discrepancies have been noted. On the one hand, some studies of samples exposed to the dual atmosphere at high temperatures (around and above 800°C) have shown enrichment of Fe on the oxide scale [32] or the formation of thicker oxide scales [31]. On the other hand, studies [104, 105] have not observed significant anomalous oxidation of samples exposed to dual-atmosphere conditions at 800°C. *Ardigo et al.* [104] did not find Fe in the oxide scales, after 100 h of exposure at 800°C in an O_2-H_2O atmosphere and observed instead a $(Cr,Mn)_3O_4$ spinel on top of a chromia scale. *Kurokawa et al.* [105] detected small quantities of Fe in the scale but did not observe break-away corrosion.

The trend to lower the operational temperatures is expected to reduce material degradation, allowing for the use of cheaper materials. However, recent research has shown an increased dual-atmosphere effect at lower temperatures. *Alnegren et al.* [21, 26], who investigated the dual-atmosphere effects at lower temperatures, found an apparent effect of the dual atmosphere for samples exposed at 600°C. The samples were covered with Fe-rich nodules, while samples exposed at higher temperatures were protective. An increase of corrosion rate at low temperatures is also reported by several authors [61, 106, 107].

Those results indicate an inverse temperature effect, as described by *Alnegren et al.* [26], i.e., a more pronounced effect observed at lower temperatures than at high temperatures. It was suggested that the inverse temperature effect is due to a reduction of Cr diffusion from the bulk, causing a decrease in Cr at the metal/oxide interface and leading to the formation of break-away oxidation.

It is widely agreed that hydrogen diffuses through the steel substrate from the fuel-side and interferes with the oxidation process on the air-side. It has been shown that hydrogen diffuses

rapidly through steel sheets and that at 600°C, it has a permeation rate in the order of $mm \cdot h^{-1}$ [108]. Numerous hypotheses have been put forward for the mechanism underlying break-away oxidation. Some research groups [109, 110] have indicated that the formation of hydroxides in the oxide scale leads to the formation of hematite nodules (Figure 11) through accelerated diffusion of Fe ions. They have assumed that metal vacancies form to balance the positive charge created by substituting an oxygen anion with a hydroxide. This would increase the cation diffusivity. An alternative explanation is that deformation of the surface (during cold work) triggers the nucleation and growth of oxide phases and increases the outward diffusion of cations [111-113]. *Rufner et al.* [31] have suggested that alteration of the oxygen activity by hydrogen could be the reason for the dual-atmosphere effect. The formation of steam within the oxide scale, which forms pores at high pressure, could increase scale growth and increase the inward diffusion of oxygen. This hypothesis has also been put forward by *Holcomb et al.* [114].

Gunduz et al. [29] discarded these hypotheses, instead it was concluded that hydrogen decreased the Cr diffusion at the grain boundaries, decreasing the Cr supply to the scale and thus promoting the formation of a non-protective Fe-based oxide scale. The beneficial effect of pre-oxidation was also demonstrated and believed to explain most of the discrepancy in the literature regarding the dual atmosphere effect [29].

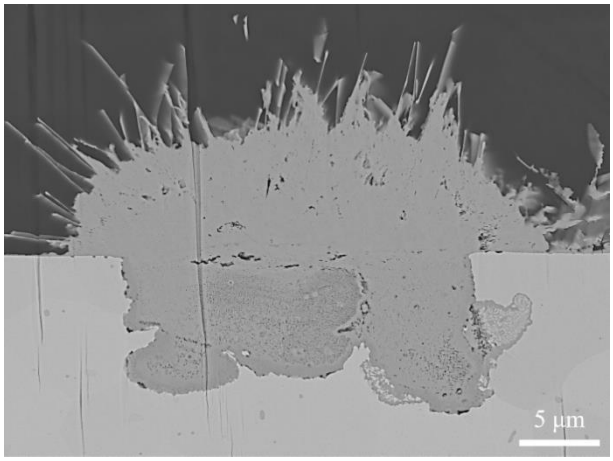

Figure 11: Cross-section of a hematite nodule formed on the air-side of an AISI 430 foil after exposure to dual-atmosphere conditions at 600 °C for 336 h.

3 Materials and Methods

3.1 Materials

The compositions of the materials used in this work, together with their respective thicknesses, are listed in Table II, Table III and Table IV.

Table II: Composition of AISI 441 substrate (in wt.%) as specified by the manufacturer, used in this work.

Material	Fe	Cr	C	Mn	Si	Ni	Ti	Nb	Al	N	P	S
AISI 441 Batch: 89893	Bal.	17.53	0.016	0.40	0.59	0.15	0.172	0.41	0.007	0.015	0.024	< 0.001

Depending on the experiment, specific sample geometries were required, and different coatings were studied. All samples produced by PVD were coated by Sandvik Materials Technology AB [115]. The Thermal Spray (TS) coatings were produced by Kuopion Konepaja Oy. Before exposure, all materials were cleaned in an ultrasonic bath, using acetone and ethanol.

Table III: Characteristics of the materials used in Manuscript I. The PVD coating was applied to sheets of the substrate, after which the samples were cut out of the steel sheets in the form of 1.5 cm × 1.5 cm coupons. TS coatings were applied on pre-cut steel sheet resulting in coated edges (see [95] for details).

Material	Thickness	Deposition process	Coating	
			Inner	Outer
AISI 441	0.3 mm	PVD	20 nm Ce	600 nm Cu
AISI 441	0.3 mm	PVD	20 nm Ce	600 nm Mn/Cu
AISI 441	0.3 mm	PVD	20 nm Ce	600 nm Co
AISI 441	0.3 mm	TS	~10 μm Cu oxide	
AISI 441	0.3 mm	TS	~10 μm Mn/Cu oxide	
AISI 441	0.3 mm	TS	~10 μm Mn/Co oxide	
AISI 441	0.3 mm	None	Uncoated	

Table IV: Characteristics of the materials used in Manuscript II. The coating was applied to sheets of the substrate, after which the samples were stamped out of the steel sheets in the form of Ø 21 mm coupons.

Material	Thickness	Deposition process	Coating	
			Fuel-side	Air-side
AISI 441	0.2 mm	PVD	Al_2O_3 (~500 nm)	Uncoated
AISI 441	0.2 mm	PVD	Al (~1000 nm)	Uncoated
AISI 441	0.2 mm	PVD	Al (~1000 nm)	10 nm Ce / 600 nm Co
AISI 441	0.2 mm	PVD	Uncoated	10 nm Ce / 600 nm Co
AISI 441	0.2 mm	PVD	Uncoated	Uncoated

The mass gain was recorded each week throughout the exposure in a separate experiment. The samples were weighed using a Mettler Toledo XP6 scale, which is accurate to one-tenth of a microgram.

3.2 Single-atmosphere exposures

The exposures were carried out in tubular furnaces (see Figure 12). The experimental set-up used for tubular furnaces is shown in Figure 13. For Manuscript I, all the samples were exposed in a tubular furnace with a humid air-flow of 6 $L \cdot min^{-1}$. Cross-sections were realized using a Broad Ion Beam (BIB) and characterized using scanning electron microscopy/energy-dispersive x-ray spectroscopy (SEM/EDS). ASR measurements were carried out to determine the resistance of the sample.

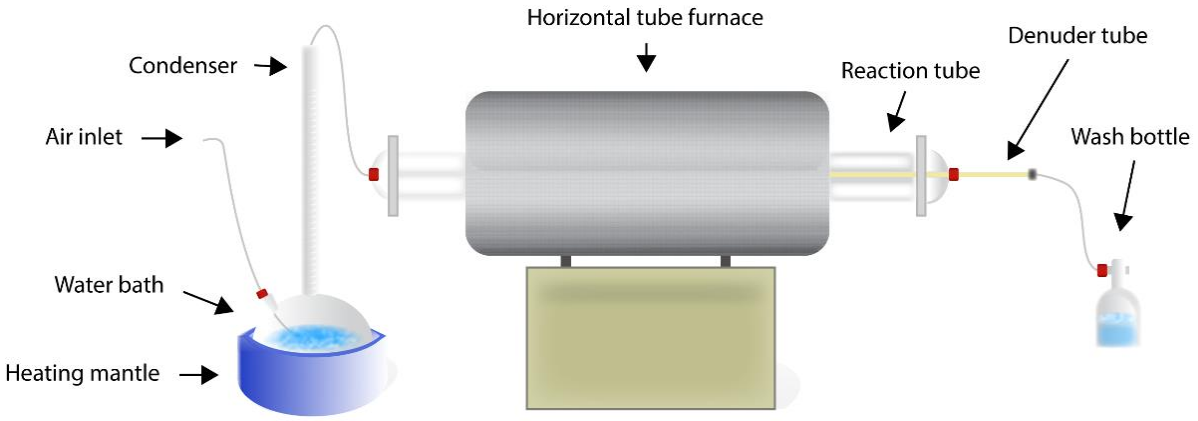

Figure 12: Experimental setup used for single-atmosphere exposures and Cr(VI) evaporation measurements. Taken from [116].

3.2.1 Cr(VI) evaporation measurements

Cr(VI) evaporation is a major issue for the life-span of an SOFC. The emission of Cr^{6+} species is poisonous for the cathode, reducing its catalytic activities. Therefore, it is necessary to quantify the level of Cr(VI) evaporation of a potential interconnect material. *Froitzheim et al.* [60] have developed a technique to measure Cr evaporation *in situ*. A denuder tube coated with Na_2CO_3 is placed downstream of the samples. The $CrO_2(OH)_2$ species evaporating from the samples will react with Na_2CO_3 in the denuder, to form the thermally stable Na_2CrO_4. The chromate is then dissolved in water and the concentration of Cr(VI) is determined by UV-VIS spectrophotometry. The chemical reaction upon which this measurement is based on is shown in Equation (3.1):

$$CrO_2(OH)_2(g) + Na_2CO_3\ (s) \rightarrow Na_2CrO_4\ (s) + H_2O\ (g) + CO_2\ (g) \qquad (3.1)$$

The coated denuders (see Figure 13) were exchanged regularly during the exposure and rinsed with distilled water. The absorbance of the resulting solution was measured by UV-VIS spectrophotometry. As shown in Section 2.3.5, the formation of $CrO_2(OH)_2$ is dependent upon the water vapour concentration in air. Therefore, all the experiments were carried out in an air atmosphere that contained 3% H_2O vapour, achieved by bubbling dried and cleaned air through a warm water bath connected to a condenser, which was set at 24.4 °C (see Figure 12). A high air-flow rate (6,000 sml·min^{-1}) was used, to ensure flow-independent Cr(VI) evaporation (Figure 7).

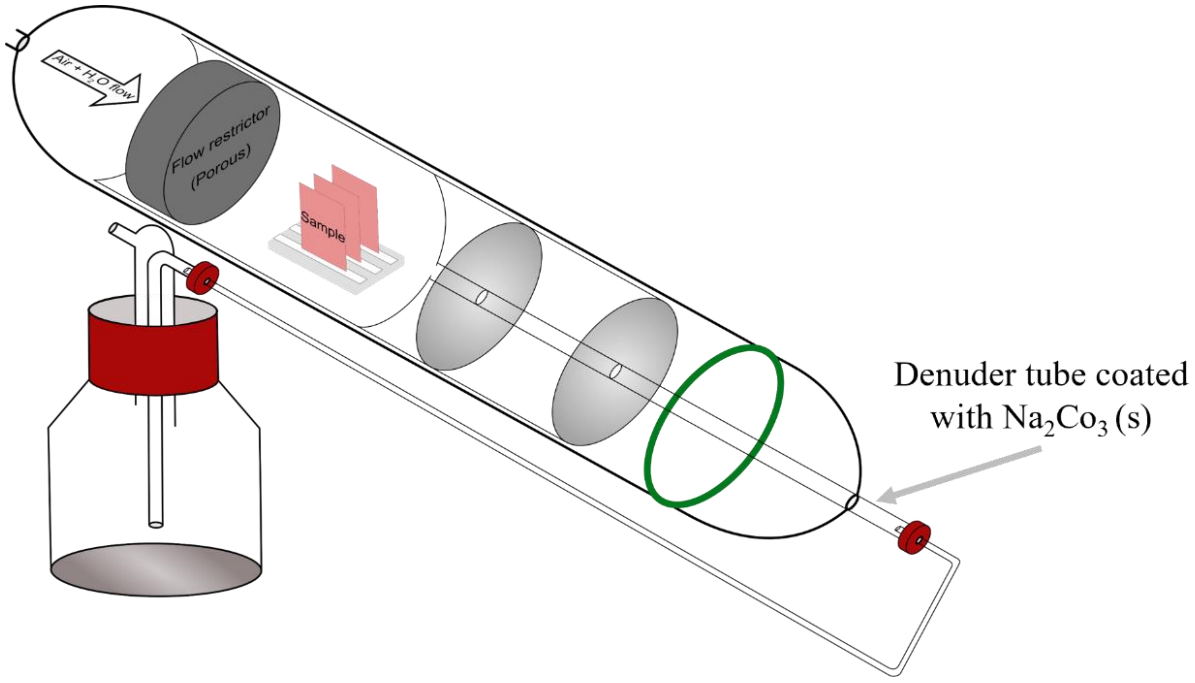

Figure 13: Experimental set-up for tube furnace exposures and Cr(VI) evaporation measurements, based on Froitzheim et al. [60].

3.3 Dual-atmosphere exposures

Dual-atmosphere exposures were carried out to investigate the dual-atmosphere effect on novel coatings. The dual-atmosphere sample holder (shown in Figure 14) is based on a design from Montana State University, USA. More details of the design can be found elsewhere [27, 31]. The sample holder contains six slots, with three on each side. Gold rings were used to ensure gas tightness, which was controlled before and after the exposure. The gas composition and flow rates are described in Figure 14. The humidity level of each gas stream was attained by bubbling the gas through water that was heated to 24.4°C, giving a controlled humidity of 3%. All the dual-atmosphere exposures were conducted at 600°C.

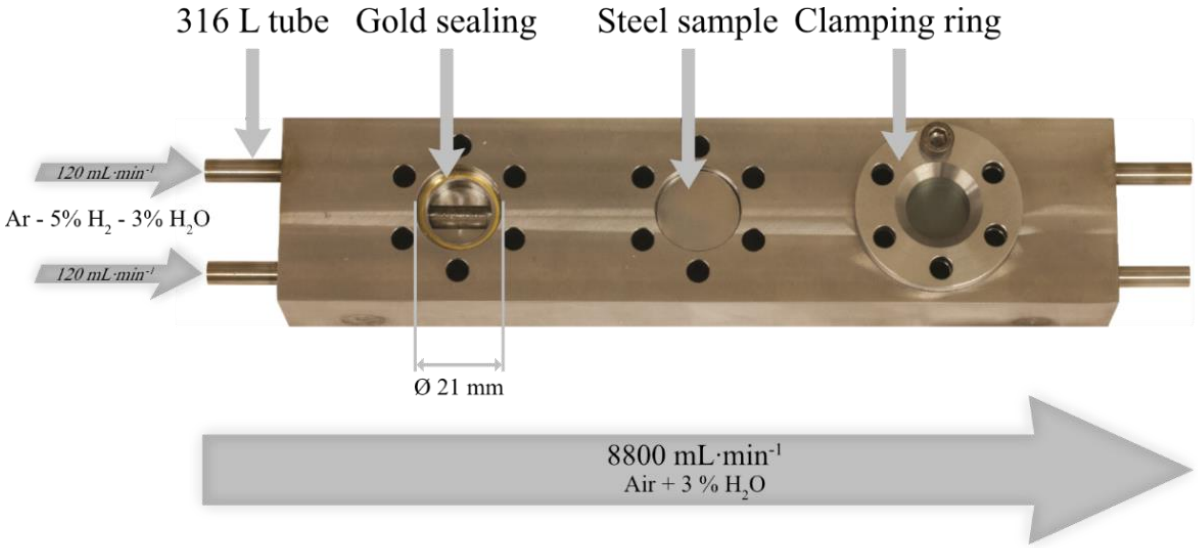

Figure 14: Sample holder for the apparatus used to assess the dual-atmosphere exposures.

3.4 Characterization methods

Different analytical methods were used to examine and characterize the sample and to evaluate the corrosion behaviour. These techniques are described in the following chapters.

3.4.1 UV-VIS Spectrophotometry

To quantify the amount of chromium that evaporated during high-temperature exposure, UV-VIS spectrophotometry was used. If a solution contains light-absorbing materials (in this work Cr^{6+}) the intensity of the light passing through the solution will decrease. The Beer-Lambert law [see Equation (3.2)] describes the relationship between absorbance A and the concentration of the light-absorbing species in the solution c:

$$A = log\frac{I_0}{I} = \varepsilon_\lambda \times c \times l \tag{3.2}$$

where I_0 is the initial light intensity, I is the light intensity after passing through the cuvette, $\varepsilon\lambda$ is the wavelength-dependent molar absorption coefficient, and l is the path length through the sample (thickness of the cuvette).

One light-absorbing species is hexavalent Cr. Therefore, solutions that contain this Cr species can be easily analysed using UV-VIS, and their Cr contents can be derived. For these solutions, the maximum absorption is at a wavelength of 370 nm. Thus, all measurements were conducted at this wavelength. More details of the measurements can be found in the previous publication [117].

3.4.2 Broad Ion Beam Milling

To obtain high quality cross-sections without impacting negatively the sample (and especially, the thin oxide scales), a Broad Ion Beam (BIB) mill was used. The working principle of this instrument involves bombardment of the sample with Ar ions. This removes the sample surface layer-by-layer (see Figure 15), while smoothing it out. This technique avoids the mechanical issues associated with using the classical polishing method. Prior to milling, the samples need to be prepared in three steps. First, the samples have to be cut in the middle, perpendicular to the rolling direction, to ensure that the cross-section is representative of the entire sample. Second, they need to be gold-coated to provide good contrast for SEM examination, and third, a silicon wafer is glued on top of the sample, to protect the oxide layer from the milling process. The Leica EM TIC 3X system was used for BIB milling, and a voltage of 8 keV was used.

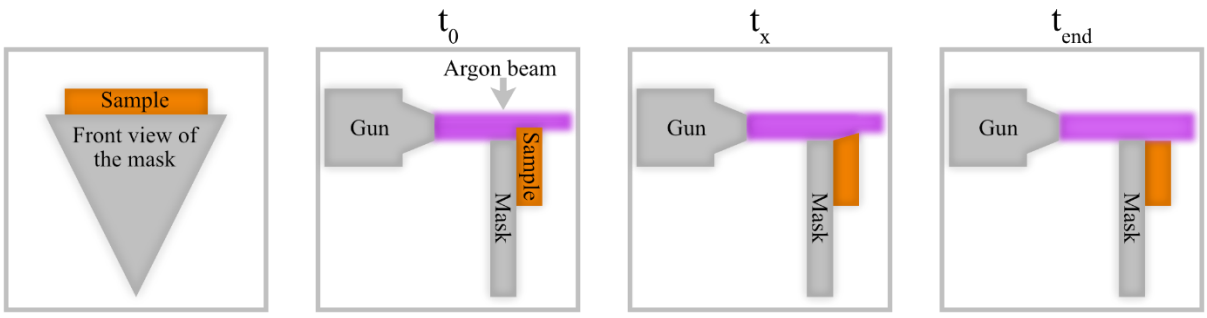

Figure 15: Schematic of the working of the BIB milling process at different time-points in the process.

3.4.3 Scanning Electron Microscopy / Energy-Dispersive x-ray Spectroscopy

SEM is a valuable tool for microstructural and morphological examinations. Compared to optical microscopy, SEM has a resolution in the nanometre range, which allows for a detailed analysis of the thin oxide layers that form on steel substrates during high-temperature exposures. In SEM, accelerated electrons interact with the surface of the sample. The nature of the resulting emissions depends on the energy released when the electrons in the sample are excited by an incoming electron beam (Figure 16). Different types of emissions can be analysed using various detectors. The three most commonly analysed emissions are: a) secondary electrons; b) back-scattered electrons; and c) x-ray radiation. Since these emissions have different energies, they can easily be detected separately by different detectors. The signals that

the detectors record generate an image of the sample surface. To understand the differences between the images created by the different detectors, it is essential to consider the interaction volume of each emission type (see Figure 16d) [118, 119]. All the listed signals were used in this work and are described in more detail below.

3.4.3.1 Secondary Electrons

Secondary electrons (SEs) are generated by the inelastic scattering of an incoming electron beam. The incoming accelerated electron ejects an electron from one shell of an atom (usually the K shell). The ejected electron is called a secondary electron (see Figure 16a). Due to their low energy (range, 1–20 eV), only the secondary electrons generated at the surface or close to the surface can be ejected from the material. They can resolve surface structures down to the order of 1 nm [118, 119].

3.4.3.2 Back-scattered Electrons

Back-scattered electrons are an excellent source of both compositional and topographic information. They are generated by elastic scattering between an electron and an atomic nucleus (Figure 16b). Because they are highly energetic, their interaction volume is higher (Figure 16d) than the secondary electrons, resulting in a lower image resolution. For heavy atoms, the signal is brighter in comparison to that of the lighter atoms, yielding to chemical contrast. The energy for back-scattered electrons is higher (similar to the accelerating voltage) than that for secondary electrons (range, 1–20 eV) [118, 119].

3.4.3.3 Energy-Dispersive x-ray Spectroscopy

Energy-Dispersive x-ray Spectroscopy (EDS) is used to obtain more-exact chemical information. For x-ray generation, the primary electron ejects an electron from the inner shell of an atom. An electron from an outer shell then relaxes into the void. This relaxation of the atom into the ground state leads to the emission of an x-ray photon (Figure 16c). The energy of the released x-ray photon is characteristic for each element. The x-ray radiation can penetrate much further into the sample than can secondary and back-scattered electrons, and the interaction volume for x-ray photons is more-substantial. However, the resolution is drastically reduced (see Figure 16d) [118, 119].

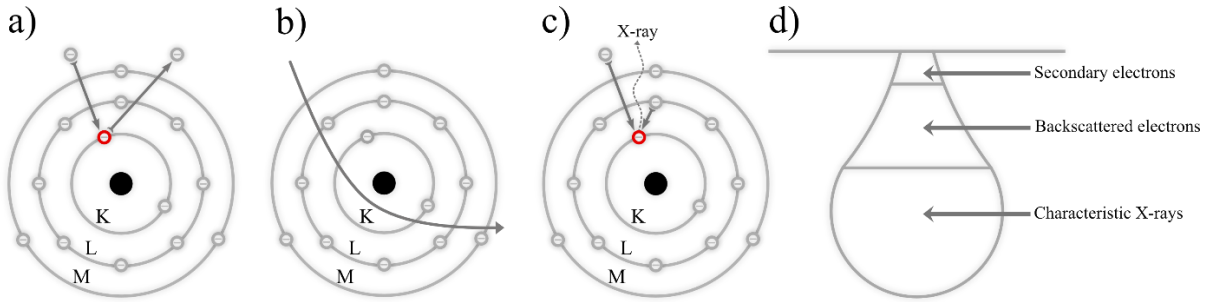

Figure 16: Schematic of the different SEM signals produced (a-c) and their interaction volumes (d) [118, 119].

3.4.4 Transmission Electron Microscopy

TEM [56] is a valuable tool for characterising the microstructure, chemical composition, and crystal structure of a sample at very high resolution. In contrast to SEM, the electrons penetrate through the sample. To be transparent to electrons, the sample must be extremely thin (usually 20–200 nm in thickness). TEM operates at a very high acceleration voltage (usually 200–300 kV). If the sample is crystalline, the incoming electrons are diffracted by planes of atoms inside the material, forming a transmission electron diffractogram. Thus, the crystalline structure of a compound can be identified [118, 120]. The TEM analysis was performed by Dr. Vijayshankar Asokan using the FEI Titan 800-300 apparatus equipped with the Oxford X-sight EDS detector. Images were acquired in scanning TEM mode using a High-Angle Annular Dark-field (HAADF) detector.

3.4.5 X-Ray Diffraction

X-ray diffraction is a technique that is commonly used to characterize the crystal structure of a crystallized material. An incoming monochromatic X-ray beam, in this study (CuK_α), is diffracted from the different lattice planes of a crystal. Diffraction phenomena occur if the incident beam's wavelength has the same order of magnitude as the inter-atomic spacing of the examined crystal. The diffraction occurs only at specific angles and only if constructive interferences are achieved. These properties are given when the Bragg equation [Equation (3.3)] is fulfilled [121].

$$n\lambda = 2d_{hkl}sin\theta_{hkl} \tag{3.3}$$

where n is an integer, λ is the wavelength, hkl are the Miller's indices, d_{hkl} is the lattice plane spacing, and θ_{hkl} is the lattice plane. The Bragg equation represents the relationship between the lattice plane spacing, d_{hkl}, and the angle at which the incoming X-ray beam meets the lattice plane θ_{hkl} (see Figure 17).

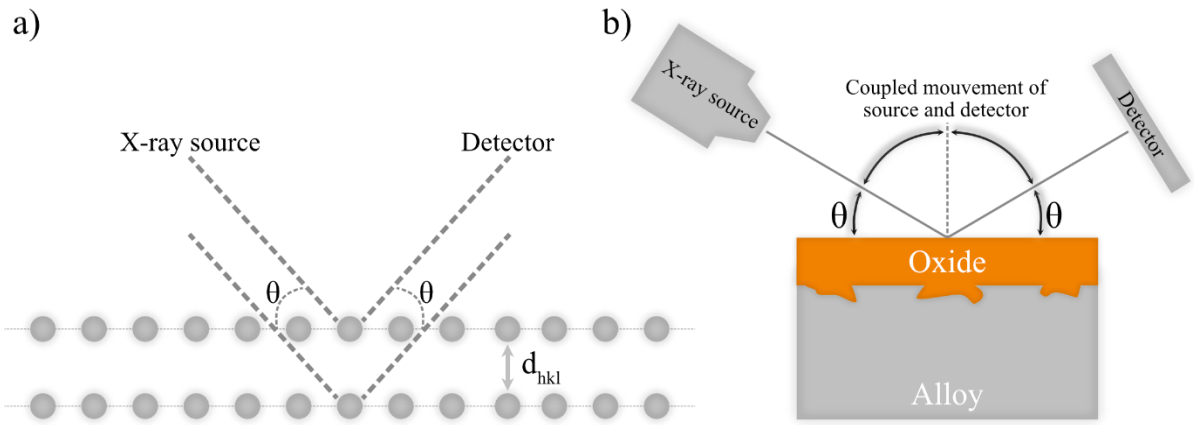

Figure 17: Schematic of: a) Bragg's law; and b) Bragg-Brentano geometry.

3.4.6 Area-Specific Resistance

ASR measurements were carried out in Manuscripts I and II to measure the resistance levels of the coatings, in both humid air (for Manuscript I) and humid H_2 (for Manuscript II). The measurements were exclusively performed *ex situ*, given that *in situ* measurements are problematic due to an effect of the Pt electrode on the overall resistance of the sample, as shown by *Grolig et al*. [122, 123]. The standard procedure to measure the ASR of an exposed samples is to sputter a Pt electrode of area 1 cm^2 onto the sample using a Quorom 150 sputter coater. Thereafter, the sputtered area is painted with a Pt-paste (Metalor 6926), dried at 150°C for 15 min, and sintered at the exposure temperature for 1 h, as described in Scenario (a) in Figure 18.

In Manuscript I, owing to poor adhesion of the Pt to the Cu oxide scales, an Au electrode was sputtered according to Scenario (b) in Figure 18. To ensure optimal contact between the Pt electrode of the experimental set-up and the sample, an approximately 400-nm Au electrode was sputtered onto the sample.

In Manuscript II, the sputtered electrode was composed of Pt. For experimental reasons, the sintering of Pt-paste could not be realised. An approximately 400-nm Pt electrode was sputtered instead, as described in Scenario (c) in Figure 18.

The NorEC Probostat (Norway) combined with the Keithley 2400 source meter was used for four-point probe measurements in DC mode (see Figure 19). A current of 100 mA was chosen for all the measurements. ASR was measured at the exposure temperature and during the cooling period, to verify the semiconductive behaviour. More details of the procedure and experimental set-up can be found elsewhere [122, 123].

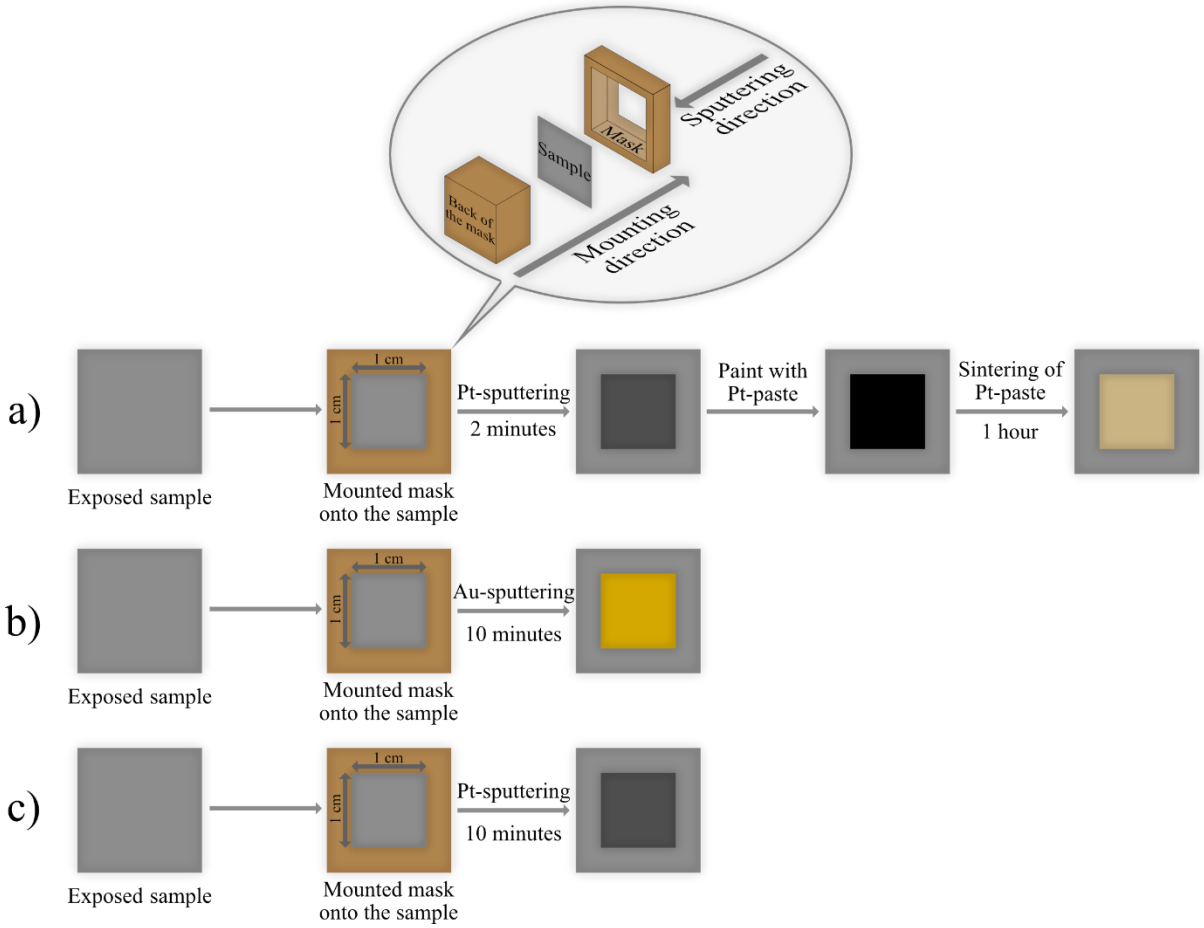

Figure 18: Schematic of the electrode preparation process [122].

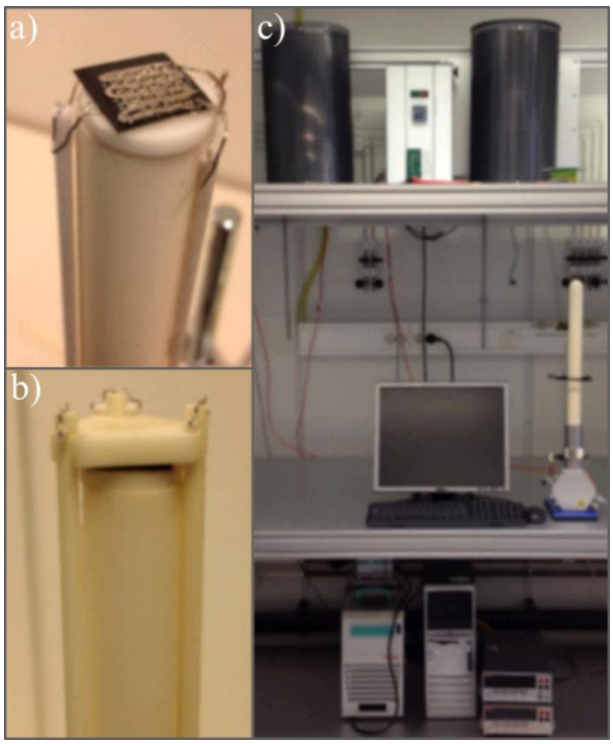

Figure 19: ASR experimental set-up with: a) the mounted sample; b) the Probostat top; and c) the entire set-up.

4 Results and Discussion

4.1 Investigation of the efficiencies of Co-based and Cu-based coatings for IT-SOFC applications using different deposition processes

For the SOFC technology to be successful, two main challenges must be overcome: a) the long-term stability of the system; and b) the material cost. As stated in Section 2.4, the choice of interconnect material strongly influences these factors. Cr(VI) evaporation from the steels and the use of cheap stainless steels, such as AISI 441, may lead to shorter material life-spans but are more cost-effective and they undergo severe corrosion when exposed to high temperatures and humid atmospheres. One strategy to overcome these problems is the use of coatings. Among the state-of-the-art coatings is a Ce/Co coating [84, 124]. Copper-based coatings are investigated to decrease further the cost. Copper is seven times cheaper than cobalt (10 USD/kg for Cu vs. 70 USD/kg for Co).

4.1.1 Cr(VI) mitigation analysis

Compared to uncoated samples, coated samples showed a much lower level of Cr(VI) evaporation throughout the exposure (see Figure 20). The uncoated samples displayed a high Cr(VI) evaporation level, which agrees with the previous findings of *Falk-Windisch et al.* [84].

On average, PVD Ce/Cu-coated and Ce/MnCu-coated samples exhibited equivalent levels of Cr(VI) evaporation. In contrast, the state-of-the-art Ce/Co coating displayed a slightly lower Cr(VI) evaporation level. This difference should not be over-interpreted, as all of the values are extremely low.

TS Cu-coated samples, TS Mn/Cu-coated samples, and TS MCO-coated samples displayed similar Cr(VI) evaporation rates after 1,000 h of exposure to humid air, compared to the PVD coatings. The TS coatings appear to exhibit lower Cr(VI) evaporation level than PVD coatings. However, in this comparison one has to take into consideration that the TS coatings have coated edges while the PVD coated samples have uncoated edges.

To allow for a direct comparison PVD Ce/Co-coated samples with coated edges were exposed to the same conditions. After 1,000 h of exposure at 650°C in humid air, the PVD Ce/Co-coated samples with coated edges displayed a similar Cr(VI) evaporation rate as the corresponding TS coatings. *Reddy et al.* [95] have reported similar results, in that they found much lower levels of Cr(VI) evaporation from Crofer 22 APU with coated edges when exposed at 800°C in air + 3% H_2O. PVD coatings seem to be as efficient as TS coatings when the edges are coated, while the coating thickness is 10-fold thinner for PVD coatings (~1 µm for PVD compared to ~10 µm for TS). It is reasonable to assume that the slight difference in Cr(VI) evaporation level between the PVD and TS coated samples is also due to the thickness of the coatings, which are thicker for TS samples, thus further reducing the Cr evaporation rate.

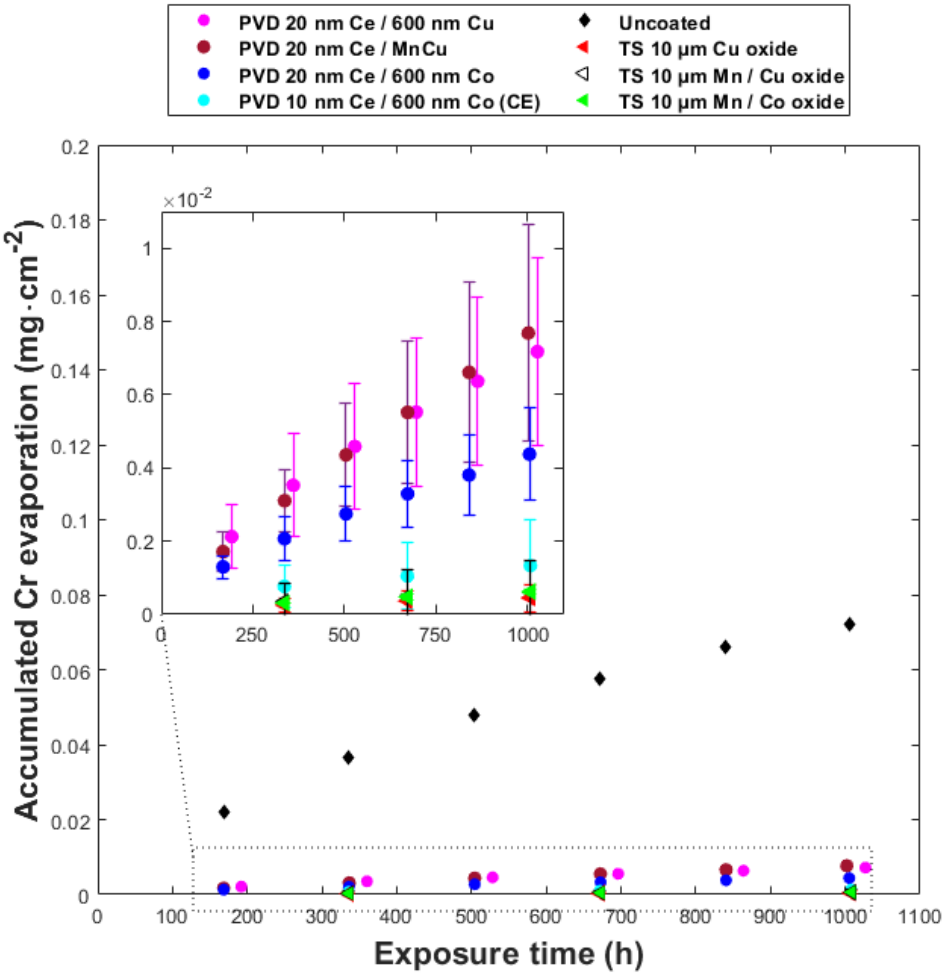

Figure 20: Cumulative Cr evaporation as a function of time for the PVD Ce/Cu-coated samples (magenta circles), PVD Ce/MnCu-coated samples (brown circles), PVD Ce/Co-coated samples (blue circles), PVD Ce/Co-coated samples with coated edges (cyan circles), TS Cu-coated samples (red triangles), TS Mn/Cu-coated samples (open triangles), TS Mn/Co-coated samples (green triangles), and uncoated samples (black diamonds) that were exposed for 1,000 h at 650°C in air that contained 3% water vapour. Error bars indicate the standard deviation.

4.1.2 Microstructural and chemical investigations

4.1.2.1 PVD Ce/Co coating

The PVD Ce/Co-coated sample cross-section, depicted in Figure 21, which was exposed for 1,000 h in air + 3% water vapour, shows a top homogeneous (Co, Mn)$_3$O$_4$ spinel cap layer. A Cr_2O_3 layer is present closest to the metal, and is approximately 200 nm in thickness. At the (Co, Mn)$_3$O$_4$ / Cr_2O_3 interface, a very thin CeO_2 layer is observed. A similar microstructure was observed by *Falk-Windisch et al.* [84]. REs have been described by *Hou et al.* [75] as being beneficial for Cr_2O_3-forming alloys in terms of lowering the Cr_2O_3 scale growth rate. A clear difference in chromia thickness has been observed between samples coated with a thin ceria layer and samples without an RE layer [16, 18, 84, 124].

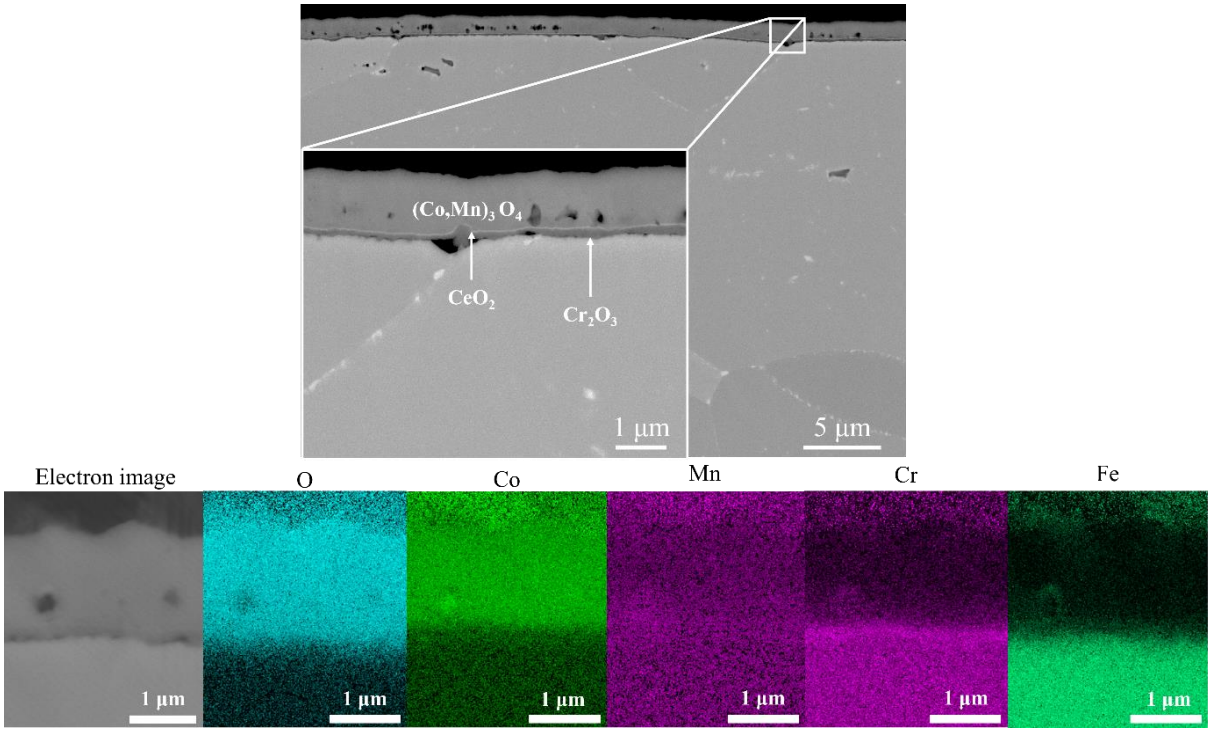

Figure 21: SEM-Back-scattered Electron (BSE) image of a BIB-milled cross-section of PVD Ce/Co-coated 441 exposed for 1,000 h at 650 °C in air + 3% water vapour, together with the corresponding EDS analysis.

4.1.2.2 PVD Ce/Cu coating

The SEM micrograph of the PVD Ce/Cu-coated sample (Figure 22a) depicts a thin and homogeneous oxide scale composed of three distinct layers. The top layer consists of a pure CuO scale, and this is followed by a $(Cu,Cr,Mn,Fe)_3O_4$ intermediate spinel, and closest to the metal, a thin Cr_2O_3 layer is observed. At the chromia/spinel interface, a thin CeO_2 layer is present. The number of pores within the top layer appears to be higher than for the Ce/Co-coated samples, as previously described in Section 4.1.2.1. TEM analysis was performed on the homogeneous layer of the Ce/Cu-coated sample (Figure 22b). The EDS analysis showed the presence of a pure CuO top layer, with a thickness of roughly 1 µm, followed by a thin spinel layer (~300 nm in thickness) with a predominance of Cu (~40 cation%), Cr (~ 30 cation%), and Mn (~20 cation%), but also containing a small quantity of Fe. *Talic et al.* [125] have suggested that there is faster diffusion of Cr when Cu is present within the spinel. This may explain the high concentration of Cr observed within the intermediate spinel.

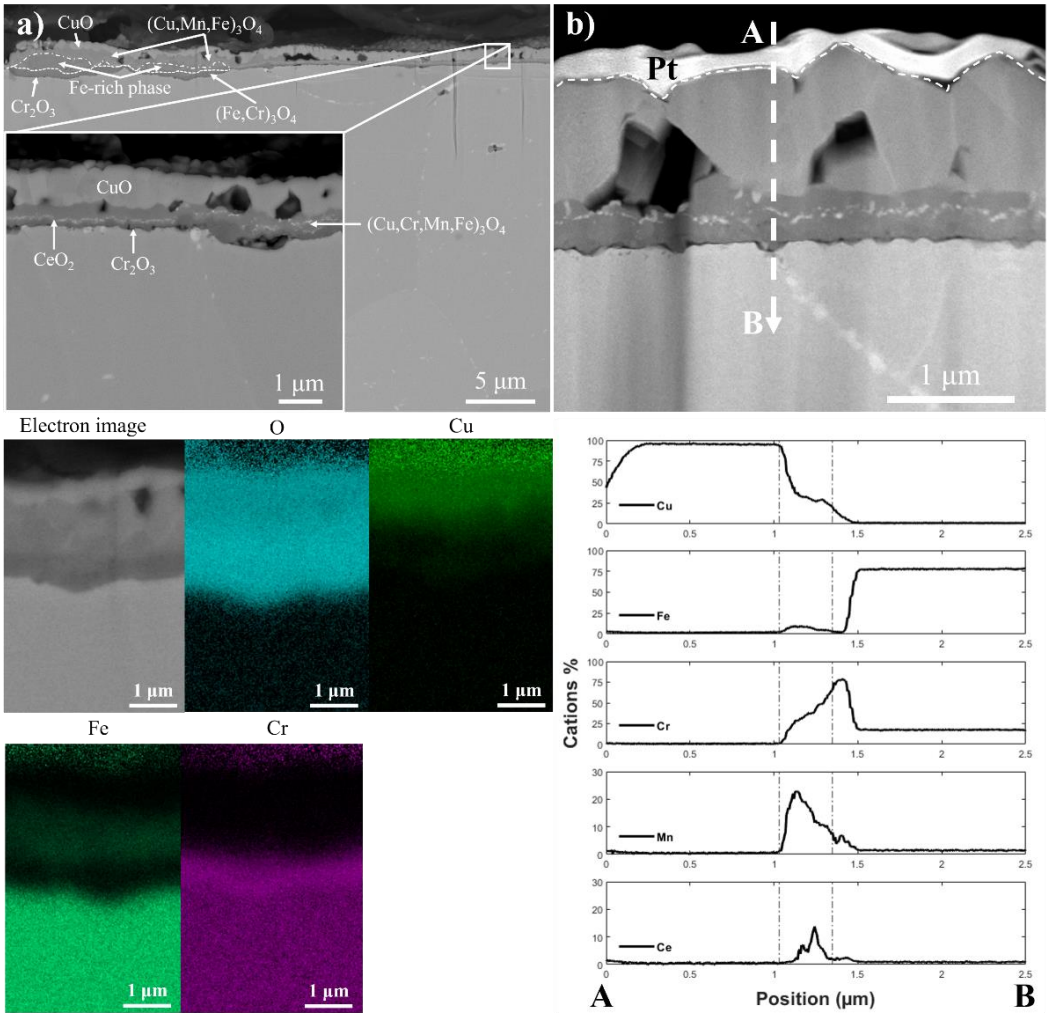

Figure 22: a) SEM-Back-scattered Electron (BSE) image of a BIB-milled cross-section of PVD Ce/Cu-coated 441 exposed for 1,000 h at 650 ℃ in air + 3% water vapour. The corresponding EDS analysis represents the chemical analysis of the nodules. b) STEM analysis of the PVD Ce/Cu-coated sample of 441 that was exposed at 650 ℃ in air + 3% H_2O for 1,000 h.

4.1.2.3 PVD Ce/MnCu coating

The analysis of the cross-section of the PVD Ce/MnCu-coated sample (Figure 23) reveals an oxide scale that comprises two microstructures. First, a homogeneous layer (~1 µm in thickness) that is composed of a $(Cu,Mn)_3O_4$ top layer and, closest to the metal, a thin Cr_2O_3 layer. Second, the nodules (~10 µm in thickness), which seem to have grown beneath the protective cap layer through Fe diffusion. The nodules are more numerous than in the case of the Ce/Cu-coated samples. The EDS chemical analysis shows that the Fe-rich phase is sandwiched between two Cu-rich layers, while Mn is only present at the top of the oxide. This is believed to be due to the deposition process, i.e., co-deposition of Mn and Cu, which led to a non-homogeneous mixture of elements. Small amounts of Cr and Fe are observed in the top layer. The formed layers are continuous and dense, resulting in a low rate of Cr evaporation throughout the exposure.

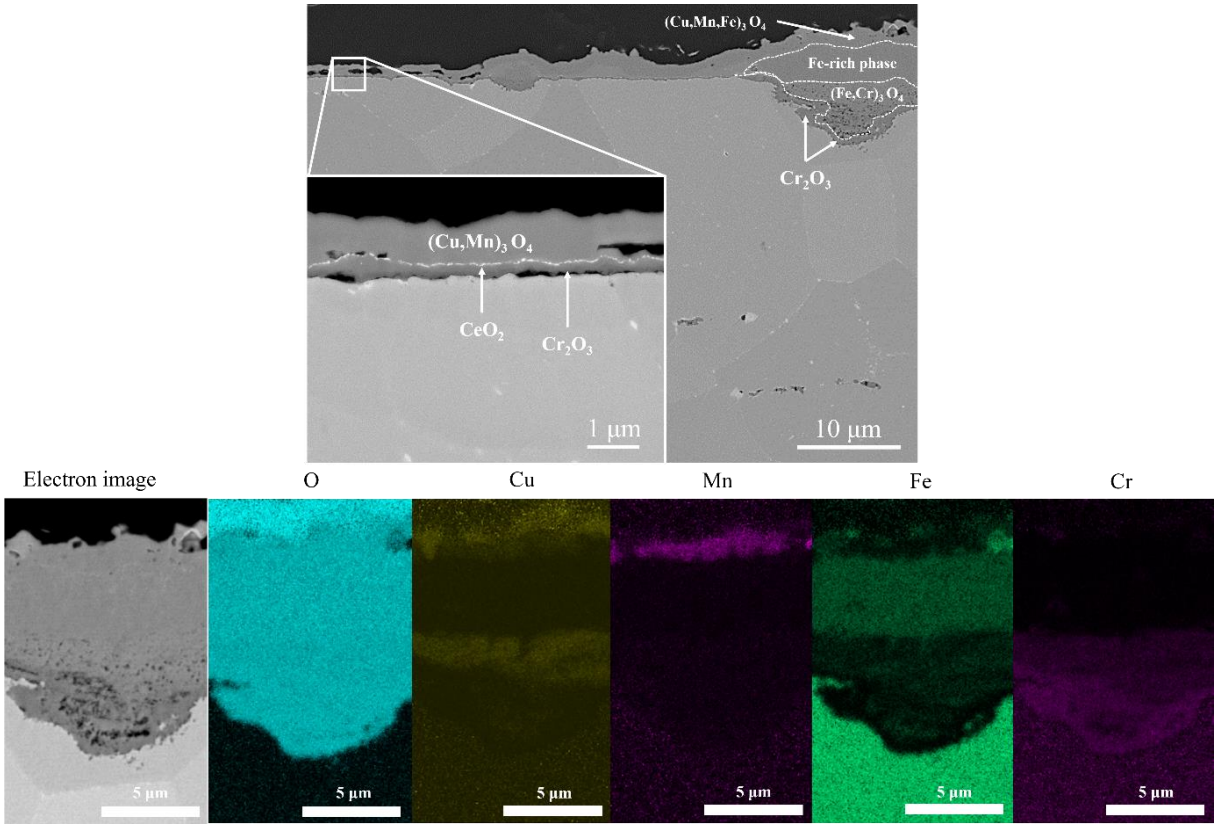

Figure 23: SEM-Back-scattered Electron (BSE) image of a BIB milled cross-section of PVD Ce/MnCu-coated 441 that was exposed for 1,000 h at 650℃ in air + 3% water vapour. The corresponding EDS analysis represents the chemical analysis of the nodules.

4.1.2.4 TS Mn/Co coating

The cross-section of the TS Mn/Co-coated sample (Figure 24) exhibits a 10 µm-thick $(Mn, Co)_3O_4$ spinel top layer. This corresponds to the initial coating thickness and composition when the coating has been sprayed onto the sample. After 1,000 h of exposure, no significant changes are observed. A thin chromia layer (~200 nm in thickness) is present closest to the metal. The EDS analysis did not reveal any signs of Fe diffusion within the protective oxide scale. A similar microstructure has been observed by *Molin et al.* [126] for coated Crofer 22 APU. A thicker chromia scale is observed, which is attributed to the higher porosity of their coating compared to the TS Mn/Co coating used in this work. Compared to the PVD Ce/Co-coated sample, the lack of a CeO_2 layer does not seem to impact negatively the oxide scale growth.

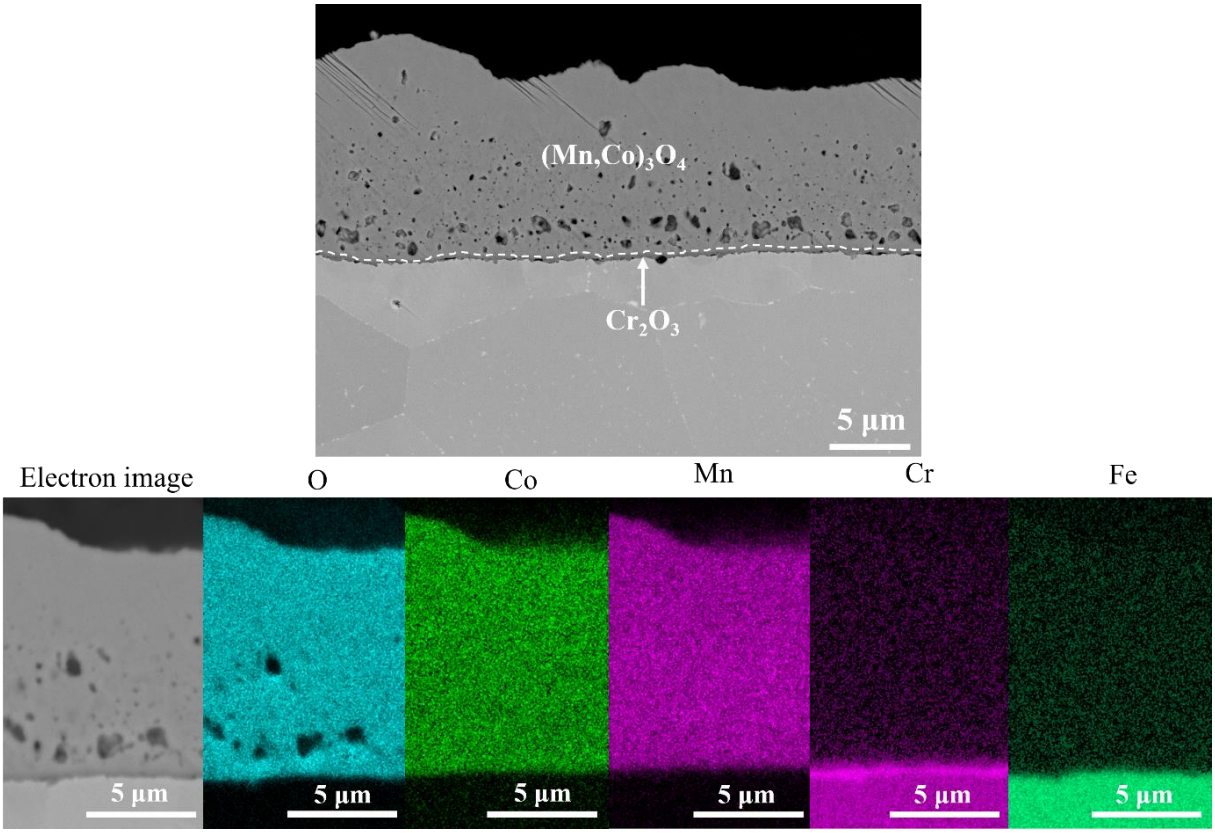

Figure 24: BIB-milled cross-section of TS Mn/Co coated sample of 441 that was exposed at 650 ℃ in humid air for 1,000 h, together with the corresponding EDS analysis.

4.1.2.5 TS Cu coating

The cross-section of the TS Cu-coated samples (see Figure 25) exhibits a thick protective CuO top layer (~10 µm) corresponding to the initial thickness of the coating. Underneath, there is a thick Fe-rich layer (~5 µm), which is followed by an $(Fe,Cr)_3O_4$ spinel and, lying closest to the metal, a thin chromia (~ 300 nm) layer. When compared to the PVD Ce/Cu-coated sample, it appears that the lack of a ceria layer promotes greater Fe ion diffusion. In this TS Cu-coated case, a thick Fe-rich layer has formed, while for the PVD Ce/Cu coating, there was a low level of Fe ion diffusion, which enriched the intermediate spinel. The higher porosity of the deposited coating could also explain the increased corrosion. The low level of Cr evaporation observed throughout the exposure is attributed to the thick oxide layers on top of the metal, which constitute a Cr barrier.

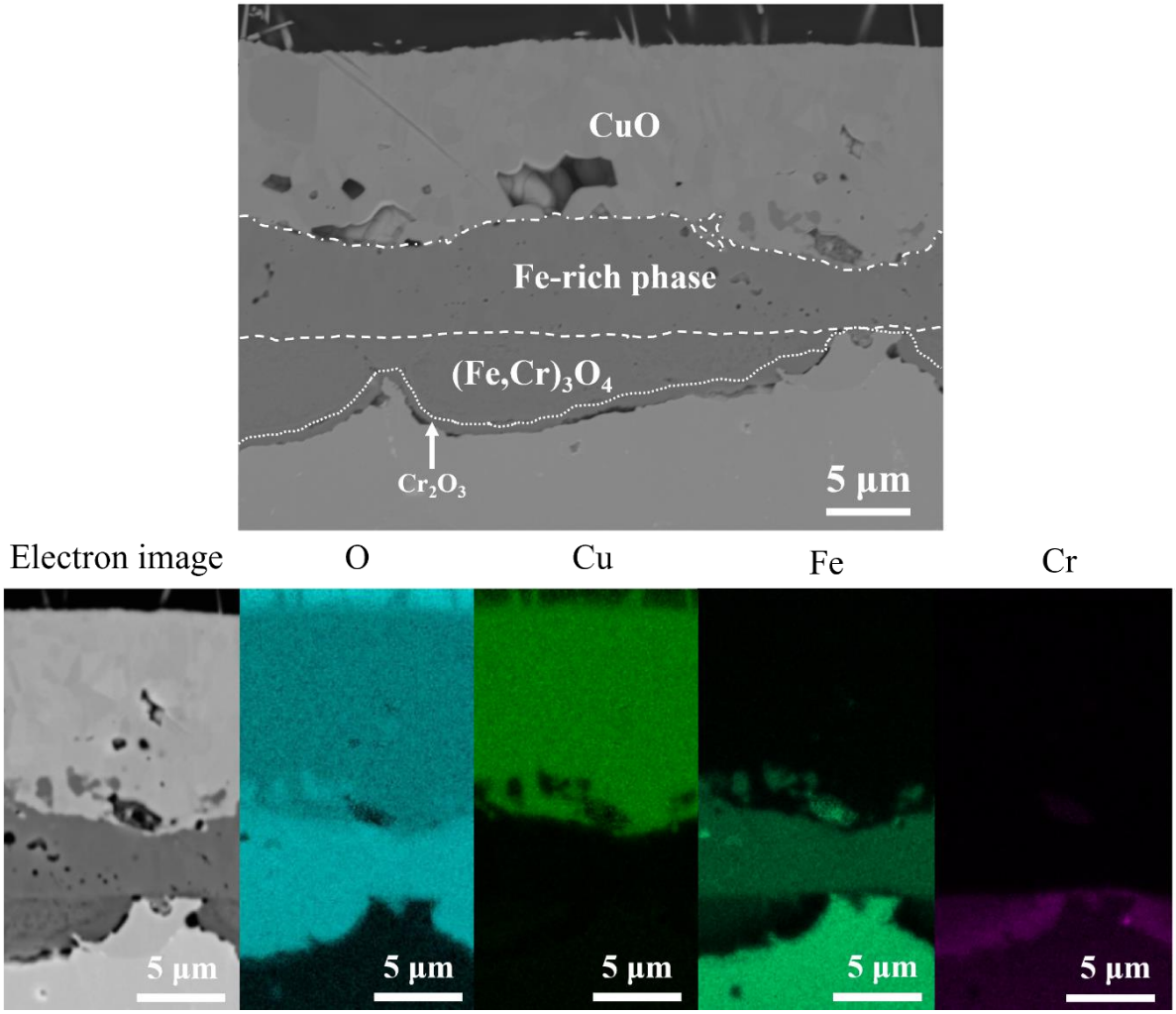

Figure 25: BIB-milled cross-section of a TS Cu-coated sample of 441 that was exposed at 650 ℃ in humid air for 1,000 h, together with the corresponding EDS analysis.

4.1.2.6 TS Mn/Cu coating

Microstructural analysis of the cross-section of the TS Mn/Cu-coated samples (see Figure 26) reveals a six-layer microstructure. The top layer comprises a CuO oxide layer, and underneath, a (Cu, Mn)$_3$O$_4$ layer and an Mn-rich layer are present. These three layers probably constitute the original coating. Beneath the top three layers, the cross-section shows the corrosion products: an iron-rich oxide layer; a (Fe, Cr)$_3$O$_4$ layer; and at the metal/oxide interface, a continuous Cr_2O_3 layer. The Fe-rich oxide layer seems to be relatively porous. One can assume that the Fe-rich oxide scale was formed by O^{2-} diffusion through the oxidised coating during the exposure, as seen previously for the TS Cu oxide. In contrast to the PVD Ce/MnCu coating, no nodules are visible. However, much-thicker oxides have been formed. The low level of Cr evaporation measured throughout the exposure is attributed to the thick layers present on top of the substrate, which constitute a Cr barrier.

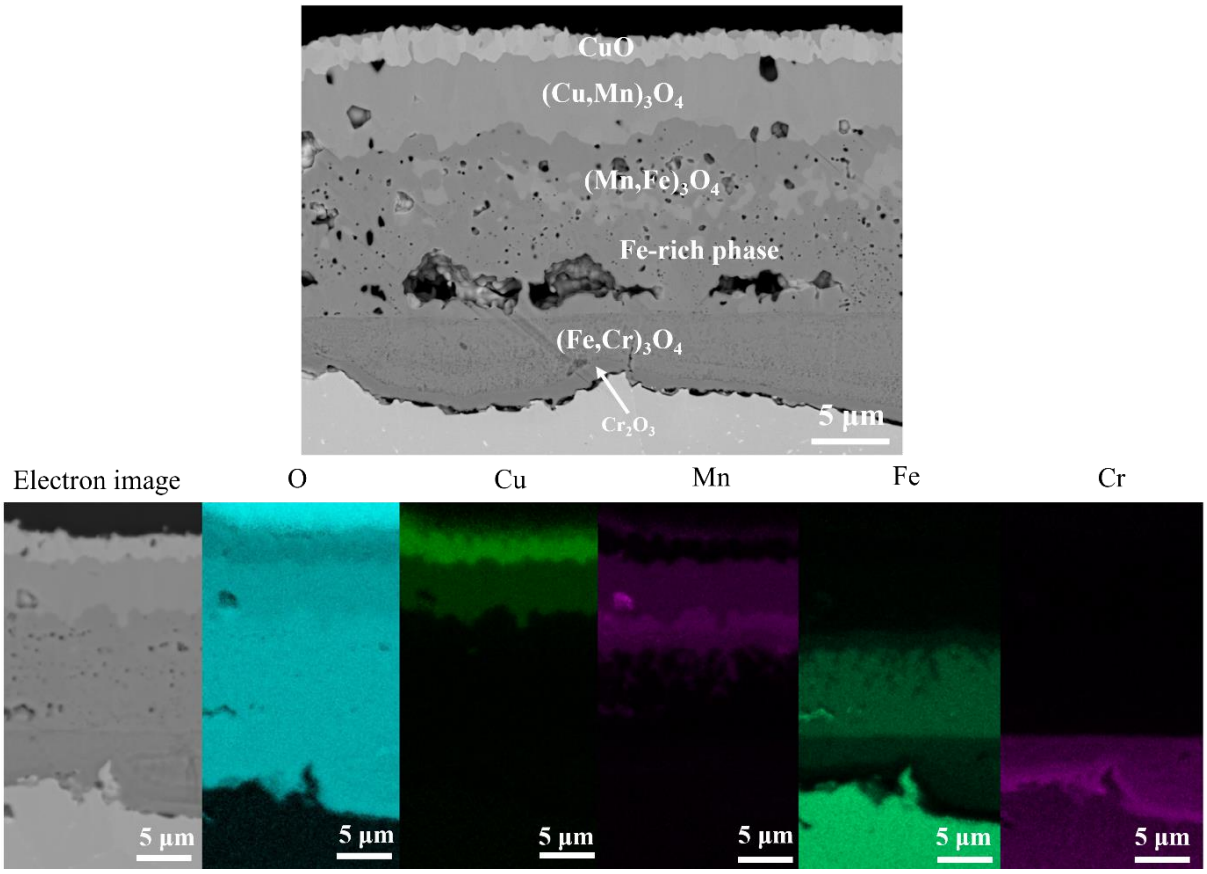

Figure 26: BIB-milled cross-section of a TS Mn/Cu-coated sample of 441 that was exposed at 650 °C in humid air for 1,000 h, with the corresponding EDS analysis.

4.1.3 Area-Specific Resistance measurements

A low ASR value was obtained for the PVD Ce/Co-coated samples (~ 3 mΩ·cm^2). *Falk-Windisch et al.* [84] recorded a similar value (~8 mΩ·cm^2) for PVD Ce/Co-coated Sanergy HT samples that were exposed to the same conditions for 500 h. This slight difference is considered within the experimental error. The PVD Ce/Cu-coated and Ce/MnCu-coated samples displayed slightly higher ASR values: the PVD Ce/Cu coating gave an ASR of 15 mΩ·cm^2, while the PVD Ce/MnCu coating gave 28 mΩ·cm^2 after 1,000 h of exposure in humid air. A plausible explanation for the slightly higher ASR value for Ce/MnCu, is somewhat the thicker chromia layer. *Goebel et al.* [127] investigated the importance of Cr_2O_3 thickness and its effect on the ASR. They concluded that chromia was the main contributor to electrical resistance. The PVD Ce/Cu-coated samples have a Cr_2O_3 thickness of roughly 200 nm, while the PVD Ce/MnCu-coated samples have an approximately 300-nm-thick Cr_2O_3 layer. Another possible explanation is the presence on the PVD Ce/MnCu-coated samples of nodules with a thicker oxide scale, which is believed to increase the overall resistance.

Overall, a thicker Cr_2O_3 scale coupled with nodules on top of the protective oxide is believed to be the main contributor to the higher ASR values.

The TS Mn/Co-coated samples had a low ASR, roughly 10 mΩ·cm^2, despite having a thicker oxide scale. The microstructural analysis shows a similar Cr_2O_3 thickness (see Figure 24) for both PVD Ce/Co and TS MCO. This correlates with the previous study [127] describing the prominent impact of chromia thickness on the ASR. The TS Cu coating gave the highest ASR value. On the other hand, the TS Mn/Cu coating had a similar ASR value to PVD Ce/MnCu, despite having a thicker oxide scale. The SEM micrographs of both coatings reveal similar Cr_2O_3 thicknesses.

Overall, the PVD Ce/Co-, PVD Ce/Cu-, and TS Mn/Co-coated samples have similar ASR values.

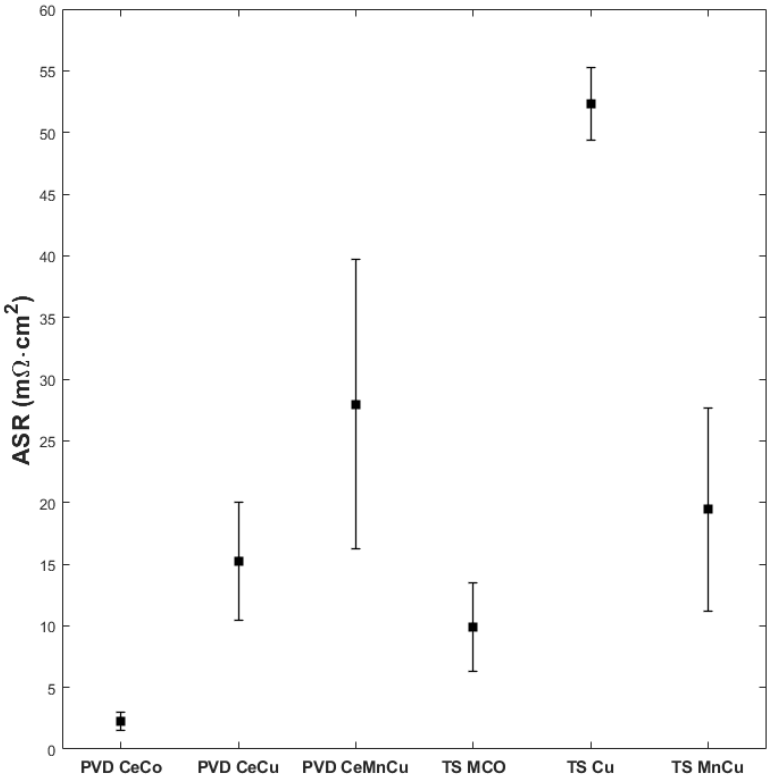

Figure 27: ASR measurements in air of samples that were exposed at 650℃ for 1,000 h in air + 3% H_2O. Error bars indicate standard deviation.

4.2 Novel coatings for protecting solid oxide fuel cell interconnects against the dual-atmosphere effect

As described in Section 2.4.4., the dual-atmosphere effect leads to rapid corrosion on the air-facing side of the uncoated sample. This effect is found to be the more-pronounced at 600°C. Mitigating the dual-atmosphere effect is crucial to increase the life-time of the interconnects. Previous research [21, 28, 128] has suggested a beneficial effect of a pre-oxidation step. The formation of a chromia layer on the fuel-side reduces hydrogen permeation and thus delays the onset of break-away but cannot stop it. Hence, coatings on the air-side or the fuel-side are the next step towards mitigating the dual-atmosphere effect and prolonging the interconnect life-time.

4.2.1 Visual Inspection

Figure 28 shows the optical images of the air-facing side of the samples exposed in dual atmosphere conditions for 3000 h An effect of the coatings can be observed in terms of delaying the onset of break-away oxidation (Figure 28). After 500 h of exposure, no signs of corrosion are observed.
After 1,000 h, the uncoated sample shows some nodules, while there are no observable signs of corrosion on the coated samples. The Ce/Co-coated samples exhibit some nodules after 2,000 h of exposure, while the remainder of the coated samples seem to retain the protective layer for 3,000 h. As will be discussed further, the SEM analysis shows that the samples coated on the fuel-side with Al_2O_3 and Al exhibit break-away corrosion that is not evident in an optical analysis.

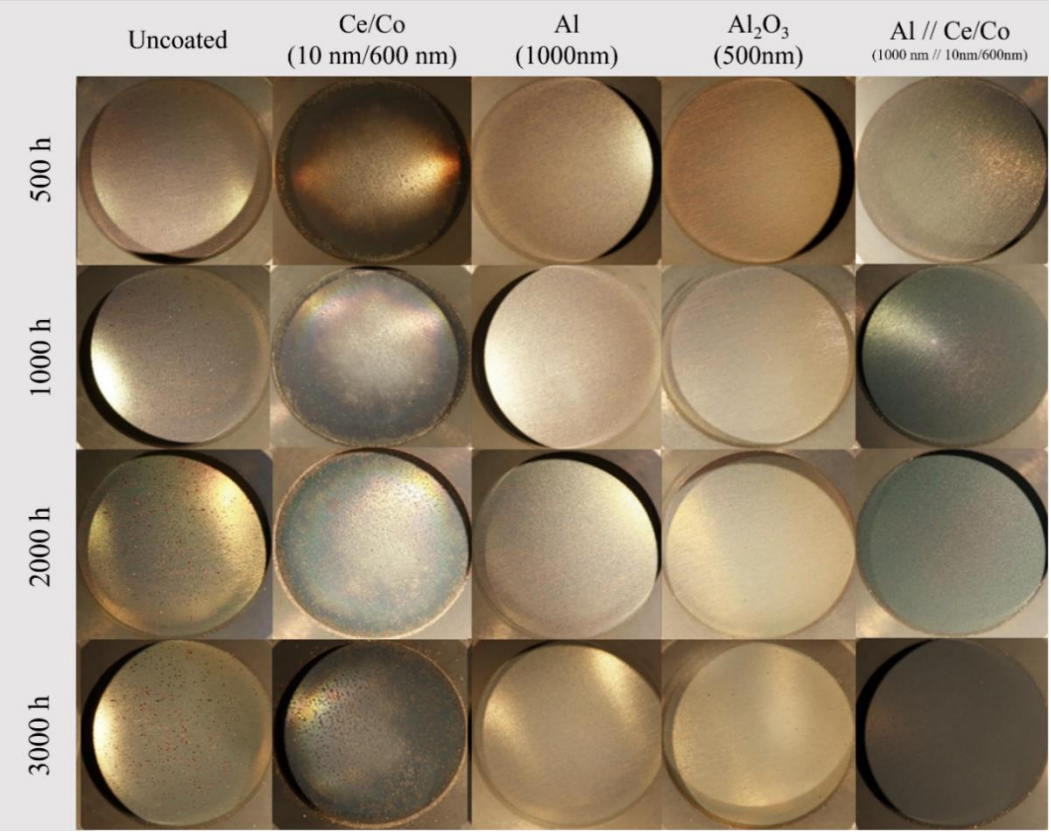

Figure 28: Photographs of the air-facing sides of AISI 441 coupons taken during discontinuous dual-atmosphere exposure (Ar-5% H_2 + 3% H_2O // Air + 3% H_2O) at 600 ℃.

4.2.2 Microstructural investigation

From the optical observations, the uncoated and Ce/Co-coated samples seem to be failing before Al- or Al_2O_3-coated samples. However, as stated before, SEM micrographs of the samples exposed for 3000 h (7000 h in the case of the Al//Ce/Co-coated sample), reveal corrosion products.

The top-view of the air-side of the uncoated sample (Figure 29a) shows large Fe_2O_3 nodules covering most of the surface. The nodules are roughly 300 μm in diameter, with well-defined whiskers on top. Previous studies [21, 29, 103] have also observed hematite nodules on samples of 441 and 430 exposed at temperatures between 600°C and 800°C under similar dual-atmosphere conditions. A protective oxide is present between the nodules. The plan-view micrograph of the fuel-side (Figure 29b) reveals an oxide scale covering the entire sample scale, together with the presence of small nodules (~2 μm) following the rolling direction. Previous studies [28, 30] have described the beneficial effect of pre-oxidation in delaying the onset of break-away oxidation. *Kurokawa et al.* [30] have shown that after a continuous chromia layer is formed, hydrogen permeation is drastically reduced because hydrogen permeability through the Cr_2O_3 scale is four orders of magnitude lower than through the un-oxidised FeCr alloy.

The plan-view image of the air-side of the Ce/Co-coated sample exhibits some localised Fe-

rich nodules (Figure 29c), which are roughly 150 μm in diameter with whiskers on top, while the remainder of the surface is covered with a protective oxide scale. It has been shown that regardless of whether the top layer is Co_3O_4, $(Co, Mn)_3O_4$ or $(Co, Mn, Fe)_3O_4$, the Cr evaporation rate at 650°C is one order of magnitude lower for Co- and Ce/Co-coated materials than it is for uncoated FeCr steel [84, 91, 129]. Thus, the depletion of Cr over time is less-pronounced than for the uncoated samples, which is expected to lead to less-severe break-away oxidation. The morphology of the fuel-side is comparable to that of the uncoated fuel-side (Figure 29b).

The top-view image of the air-side of the Al-coated sample exposed for 3,000 h (Figure 29e) depicts small nodules with "plate-shaped" features on top that cover most of the surface. The "plate-shaped" features differ from the full-grown whiskers observed on the uncoated and Ce/Co-coated samples. These small nodules seem to be thinner (~10 μm) than the large nodules observed for the uncoated (~25 μm) and Ce/Co-coated (~40 μm) samples. A protective oxide layer is present between the nodules. After 3,000 h of exposure, the small nodules are roughly 5 μm in diameter. The plan-view micrograph of the fuel-side (see Figure 29f) shows a uniform, Al-rich protective oxide covering the whole sample. After the pre-oxidation step (see Figure 30), the plan-view image of the Al-coated sample on the fuel-side depicts Fe-rich small nodules with "plate-shaped" features on top, following the rolling direction. These small nodules cover most of the sample surface and are roughly similar in size to the nodules seen after exposure, indicating that the Al-rich oxide on the fuel-side acts as an effective barrier to hydrogen permeation.

The combination of Al coating on the fuel-side and Ce/Co coating on the air-side is believed to be the most relevant with respect to mitigating the dual-atmosphere effect. The plan-view image of the air-side (see Figure 29g) depicts small Fe-rich nodules, similar to those seen in the Ce/Co-coated sample. These small nodules differ from those in the Al-coated sample, as an oxide layer covers them. However, they are fewer in number than in the Al-coated sample. The remainder of the sample is covered with a protective oxide layer. The SEM micrograph of the fuel-side (see Figure 29h) depicts a morphology similar to that of the Al-coated sample, with an Al-rich oxide covering the entire sample.

An alumina coating could be a viable alternative to a metallic Al coating, as it is already in an oxide state, given that no break-away oxidation was noted after pre-oxidation (see Manuscript II, Figure 6a). The micrograph of the air-side of the Al_2O_3-coated sample (see Figure 29i) shows a protective oxide scale with few Fe_2O_3 nodules. Smaller nodules (~4 μm) that are covered by the oxide layer are also observed. The plan-view image of the fuel-side (see Figure 29j) shows a protective Al_2O_3 scale covering the whole sample. Some micro-cracks can be observed, and these might allow hydrogen to diffuse into the bulk.

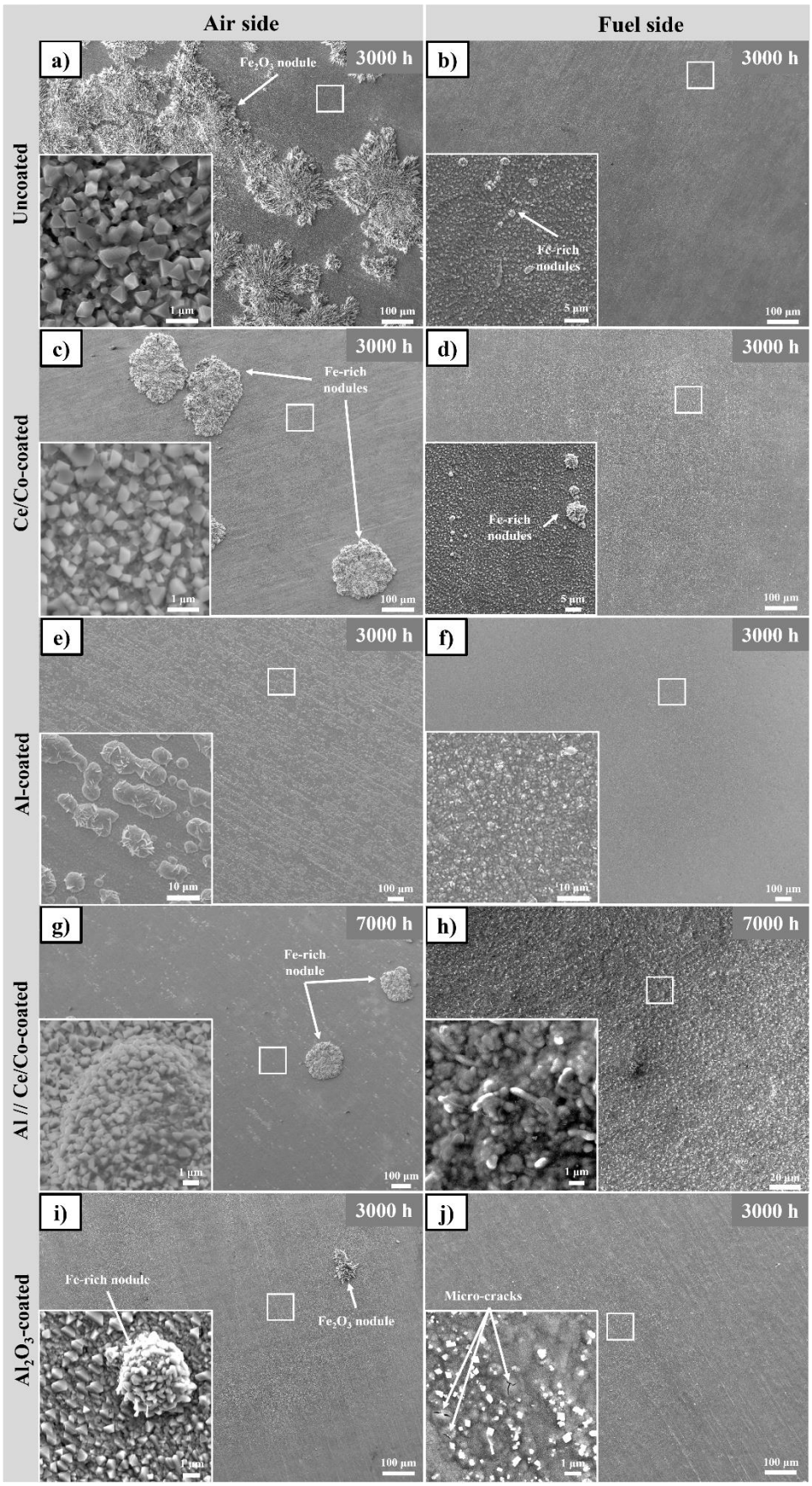

Figure 29: Plan-view SEM micrographs of uncoated, Ce/Co-, Al-, Al//Ce/Co- and Al_2O_3-coated AISI 441 samples exposed in a dual atmosphere (Ar-5% H_2 + 3% H_2O // Air + 3% H_2O) at 600 °C.

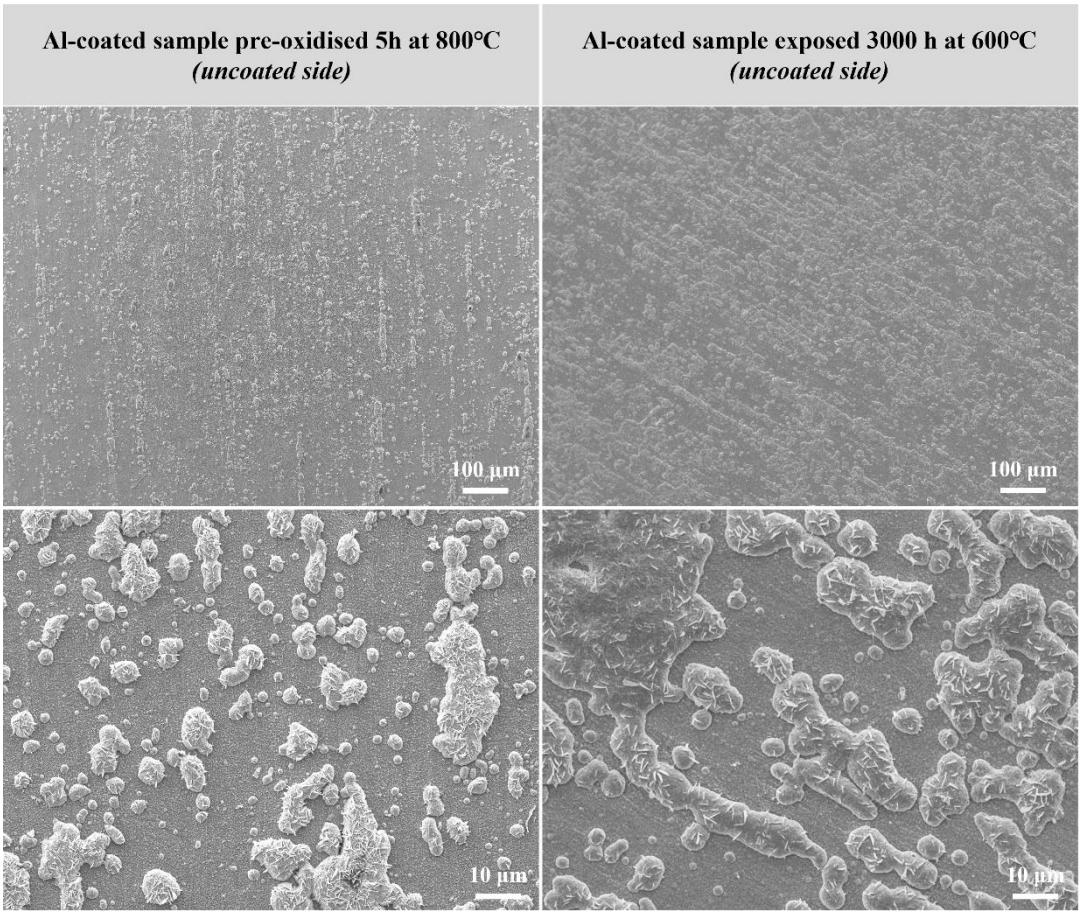

Figure 30: Comparison of the surface states of the Al-coated sample after 5 h of pre-oxidation at 800 °C and after 3,000 h of exposure at 600 °C under dual-atmosphere conditions.

4.2.3 Area-Specific Resistance measurements

The average ASR for Al_2O_3-coated samples exposed at 600℃ in a humid reducing atmosphere for 668 h was ~3.8 Ω·cm^2, as compared to ~100 mΩ·cm^2 for uncoated samples. This is in line with previous results [130, 131] describing how alumina acts as an insulator at high temperatures.

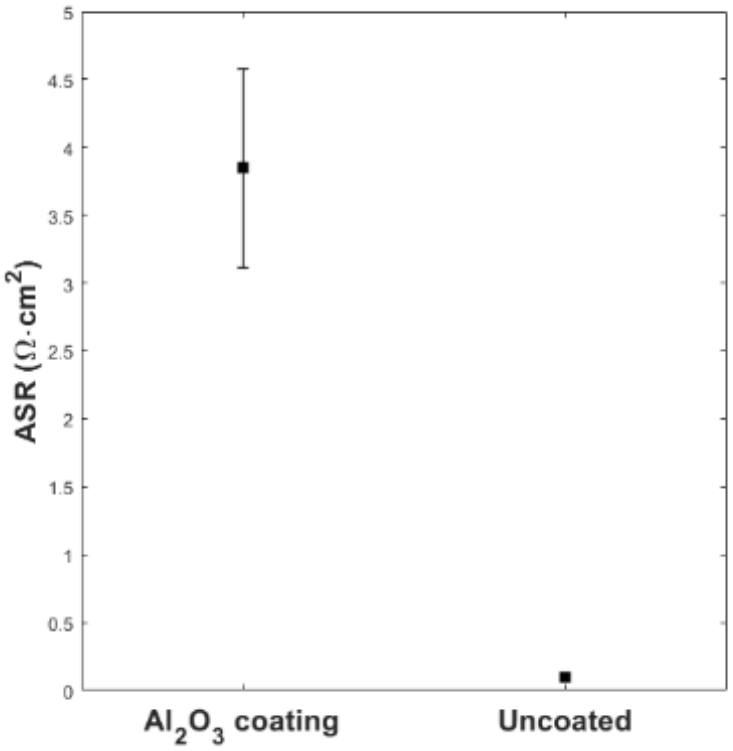

Figure 31: ASR measurements of a PVD Al_2O_3-coated sample and an uncoated sample, exposed in Ar – 5% H_2 – 3% H_2O with a flow rate of 120 sml·min^{-1} for 668 h at 600℃. The error bars represent the maximum and minimum values measured.

The use of alumina as coating poses major challenges as its insulating properties make its use as interconnect coating difficult.

5 Summary

The present work investigates two major aspects of the degradative mechanisms for ferritic stainless steels used as interconnect materials in SOFCs:

- The influence of Cu-based coatings on the oxide scale growth; and
- The effect of coatings on mitigating the dual-atmosphere effect on samples exposed at 600°C for up to 7,000 h.

We show that the PVD Ce/Cu coating gives the best corrosion protection among the Cu-based coatings investigated. It shows a similar mass gain and similar Cr(VI) evaporation as the state-of-the-art PVD Ce/Co coating after 1,000 h of exposure in air + 3% H_2O. The ASR measurements gave equivalent values for PVD Ce/Cu and PVD Ce/Co. However, the Cu-based coating seems to induce Fe diffusion, as an Fe enrichment is seen in the intermediate spinel for PVD Ce/Cu-coated samples, despite the presence of a CeO_2 layer, and Fe-rich layers are observed for the TS Cu-coated and TS Mn/Cu-coated samples. This has not been observed for Co-based coatings. Furthermore, PVD-deposited coatings exhibit the same efficiency in mitigating Cr(VI) evaporation as TS coatings, while being 10-times thinner.

Overall, PVD Ce/Cu coating could be an excellent alternative to the state-of-the-art PVD Ce/Co coating, as it exhibits similar corrosion characteristics. The use of copper instead of cobalt would also reduce the production costs for interconnects.

PVD coatings have proven to be efficient in a single atmosphere at low temperatures. However, no studies have demonstrated their effectiveness in a dual atmosphere at 600°C. This work shows that applying a coating on the fuel-side mitigates the dual-atmosphere effect. A PVD Ce/Co coating exposed in a dual atmosphere slightly improves the corrosion resistance, as compared to uncoated samples. Fewer, smaller, and more-localised nodules are present over the surface. A combination of Ce/Co coating on the air-side and Al coating on the fuel-side gave excellent results, after 7000 h of exposure, as it combined the corrosion properties seen for both coatings individually.

Al and Al_2O_3 coatings on the fuel-side gave good results. These coatings efficiently mitigate the dual-atmosphere effect and the oxide scale formed during pre-oxidation exhibits only minimal changes during the course of the 3000h exposure. However, the use of metallic Al or Al_2O_3 coatings poses new challenges, as alumina is known to be a poor electrical conductor.

References

1. Leggett, J., *Global warming: the Greenpeace report*. 1990: Oxford University Press.
2. Masson-Delmotte, V., et al., *Global warming of 1.5 C.* An IPCC Special Report on the impacts of global warming of, 2018. **1**(5).
3. Programme, U.N.E., *Emissions Gap Report 2020*. 2020.
4. Ritchie, H. and M. Roser, *Energy.* Our World in Data, 2020.
5. Basu, R.N., J. Mukhopadhyay, and A.D. Sharma. *High Temperature Fuel Cell*. in *Proc Indian Natn Sci Acad*. 2015.
6. Yamamoto, O., *Solid oxide fuel cells: fundamental aspects and prospects.* Electrochimica Acta, 2000. **45**(15-16): p. 2423-2435.
7. Wang, Y., et al., *A review of polymer electrolyte membrane fuel cells: Technology, applications, and needs on fundamental research.* Applied energy, 2011. **88**(4): p. 981-1007.
8. Staffell, I., A. Ingram, and K. Kendall, *Energy and carbon payback times for solid oxide fuel cell based domestic CHP.* International Journal of Hydrogen Energy, 2012. **37**(3): p. 2509-2523.
9. Stambouli, A.B. and E. Traversa, *Fuel cells, an alternative to standard sources of energy.* Renewable and sustainable energy reviews, 2002. **6**(3): p. 295-304.
10. Brandon, N., *Solid oxide fuel cell lifetime and reliability: critical challenges in fuel cells*. 2017: Academic Press.
11. Battelle, *Manufacturing cost analysis of 1 kW and 5kW solid oxide fuel cell (SOFC) for auxillary power applications.* 2014.
12. Smith, L., et al., *Comparative environmental profile assessments of commercial and novel material structures for solid oxide fuel cells.* 2019. **235**: p. 1300-1313.
13. Stambouli, A.B. and E. Traversa, *Solid oxide fuel cells (SOFCs): a review of an environmentally clean and efficient source of energy.* Renewable and sustainable energy reviews, 2002. **6**(5): p. 433-455.
14. Shaigan, N., et al., *A review of recent progress in coatings, surface modifications and alloy developments for solid oxide fuel cell ferritic stainless steel interconnects.* Journal of Power Sources, 2010. **195**(6): p. 1529-1542.
15. Quadakkers, W., et al., *Metallic interconnectors for solid oxide fuel cells–a review.* Materials at high temperatures, 2003. **20**(2): p. 115-127.
16. Froitzheim, J. and J.-E. Svensson, *Multifunctional nano-coatings for SOFC interconnects.* Ecs Transactions, 2011. **35**(1): p. 2503.
17. Trebbels, R., T. Markus, and L. Singheiser, *Investigation of chromium vaporization from interconnector steels with spinel coatings.* Journal of Fuel Cell Science and Technology, 2010. **7**(1).
18. Froitzheim, J., et al., *Long term study of Cr evaporation and high temperature corrosion behaviour of Co coated ferritic steel for solid oxide fuel cell interconnects.* Journal of Power Sources, 2012. **220**: p. 217-227.
19. Hou, P.Y. and J. Stringer, *The effect of reactive element additions on the selective oxidation, growth and adhesion of chromia scales.* Materials Science and Engineering: A, 1995. **202**(1): p. 1-10.
20. Birks, N., G.H. Meier, and F.S. Pettit, *Introduction to the high temperature oxidation of metals*. 2006: Cambridge university press.
21. Alnegren, P., et al., *Severe dual atmosphere effect at 600 C for stainless steel 441.* Journal of Power Sources, 2016. **301**: p. 170-178.
22. Boaro, M. and A.S. Aricò, *Advances in medium and high temperature solid oxide fuel cell technology*. Vol. 574. 2017: Springer.
23. Petric, A. and H. Ling, *Electrical conductivity and thermal expansion of spinels at elevated temperatures.* Journal of the American Ceramic Society, 2007. **90**(5): p. 1515-1520.
24. Directorate-General for Internal Market, I., Entrepreneurship and SMEs and E. Commission. *https://ec.europa.eu/growth/sectors/raw-materials/areas-specific-interest/critical-raw-materials_en*. 2020.

25. Farjana, S.H., N. Huda, and M.P. Mahmud, *Life cycle assessment of cobalt extraction process.* Journal of Sustainable Mining, 2019. **18**(3): p. 150-161.
26. Alnegren, P., et al., *Temperature dependence of corrosion of ferritic stainless steel in dual atmosphere at 600–800 C.* Journal of Power Sources, 2018. **392**: p. 129-138.
27. Gannon, P. and R. Amendola, *High-temperature, dual-atmosphere corrosion of solid-oxide fuel cell interconnects.* Jom, 2012. **64**(12): p. 1470-1476.
28. Goebel, C., et al., *The effect of pre-oxidation parameters on the corrosion behavior of AISI 441 in dual atmosphere.* international journal of hydrogen energy, 2018. **43**(31): p. 14665-14674.
29. Gunduz, K.O., et al., *The effect of hydrogen on the breakdown of the protective oxide scale in solid oxide fuel cell interconnects.* Corrosion Science, 2021. **179**: p. 109112.
30. Kurokawa, H., et al., *Hydrogen permeation through Fe-16Cr alloy interconnect in atmosphere simulating SOFC at 1073 K.* Journal of The Electrochemical Society, 2004. **151**(8): p. A1264.
31. Rufner, J., et al., *Oxidation behavior of stainless steel 430 and 441 at 800 C in single (air/air) and dual atmosphere (air/hydrogen) exposures.* International Journal of Hydrogen Energy, 2008. **33**(4): p. 1392-1398.
32. Skilbred, A.W.B. and R. Haugsrud, *The effect of dual atmosphere conditions on the corrosion of Sandvik Sanergy HT.* International Journal of Hydrogen Energy, 2012. **37**(9): p. 8095-8101.
33. Larminie, J., A. Dicks, and M.S. McDonald, *Fuel cell systems explained*. Vol. 2. 2003: J. Wiley Chichester, UK.
34. Kirubakaran, A., S. Jain, and R.K. Nema, *A review on fuel cell technologies and power electronic interface.* Renewable and Sustainable Energy Reviews, 2009. **13**(9): p. 2430-2440.
35. Roach, J. *https://news.microsoft.com/innovation-stories/hydrogen-datacenters/*. 2020.
36. Powell, M., et al., *Demonstration of a highly efficient solid oxide fuel cell power system using adiabatic steam reforming and anode gas recirculation.* Journal of Power Sources, 2012. **205**: p. 377-384.
37. Ni, M., M.K.H. Leung, and D.Y.C. Leung, *Technological development of hydrogen production by solid oxide electrolyzer cell (SOEC).* International journal of hydrogen energy, 2008. **33**(9): p. 2337-2354.
38. Singhal, S.C. and K. Kendall, *High-temperature solid oxide fuel cells: fundamentals, design and applications*. 2003: Elsevier.
39. Göbel, C., *Strategies to Mitigate the Degradation of Stainless-Steel Interconnects Used in Solid Oxide Fuel Cells*. 2020: Chalmers Tekniska Hogskola (Sweden).
40. Harumi, Y. and H. Teruhisa, *"Cathode"*, in *High temperature solid oxide fuel cells - fundamentals, design and applications.*, C.S. Subhash and K. Kevin, Editors. 2003, Elsevier.
41. Ji, Y., J. Kilner, and M. Carolan, *Electrical properties and oxygen diffusion in yttria-stabilised zirconia (YSZ)–La0. 8Sr0. 2MnO3±δ (LSM) composites.* Solid State Ionics, 2005. **176**(9-10): p. 937-943.
42. Yang, C.-C.T., W.-C.J. Wei, and A. Roosen, *Electrical conductivity and microstructures of La0. 65Sr0. 3MnO3–8 mol% yttria-stabilized zirconia.* Materials Chemistry and Physics, 2003. **81**(1): p. 134-142.
43. Singhal, S.C., *Solid oxide fuel cells: past, present and future*, in *Solid Oxide Fuels Cells: Facts and Figures*. 2013, Springer. p. 1-23.
44. Fergus, J., et al., *Solid oxide fuel cells: materials properties and performance*. 2016: CRC press.
45. Kendall, K. and M. Kendall, *High-temperature solid oxide fuel cells for the 21st century: fundamentals, design and applications*. 2015: Elsevier.
46. Z, C. and W. J-H, *"Anodes"*, in *Solid oxide fuel cells: materials properties and performance*, J. Fergus, et al., Editors. 2009, Taylor & Francis Group.
47. Sverdrup, E.F., A.D. Glasser, and D.H. Archer, *Fuel cell comprising a stabilized zirconium oxide electrolyte and a doped indium or tin oxide cathode*. 1971, Google Patents.
48. Zhang, J. and D.P. Wilkinson, *"Interconnects"*, in *Solid oxide fuel cells: materials properties and performance*, J. Fergus, et al., Editors. 2009, Taylor & Francis Group: Florida.
49. Young, D.J., *High temperature oxidation and corrosion of metals*. Vol. 1. 2008: Elsevier.
50. Kofstad, P., *High temperature corrosion.* Elsevier Applied Science Publishers, Crown House, Linton Road, Barking, Essex IG 11 8 JU, UK, 1988., 1988.
51. Ellingham, H.J.T., *Reducibility of oxides and sulphides in metallurgical processes.* J. Soc.

Chem. Ind, 1944. **63**(5): p. 125-160.
52. Wagner, C., *Beitrag zur theorie des anlaufvorgangs.* Zeitschrift für physikalische Chemie, 1933. **21**(1): p. 25-41.
53. Evans, H., A. Donaldson, and T. Gilmour, *Mechanisms of breakaway oxidation and application to a chromia-forming steel.* Oxidation of Metals, 1999. **52**(5): p. 379-402.
54. Schütze, M., D. Renusch, and M. Schorr, *Chemical-mechanical failure of oxide scales on 9% Cr steels in air with H2O.* Materials at High Temperatures, 2005. **22**(1-2): p. 113-120.
55. Smart, L.E. and E.A. Moore, *Solid state chemistry: an introduction*. 2012: CRC press.
56. Asteman, H., *Water Vapour induced active oxidation of stainless steel.* 2002.
57. Gindorf, C., L. Singheiser, and K. Hilpert, *Vaporisation of chromia in humid air.* Journal of Physics and Chemistry of Solids, 2005. **66**(2-4): p. 384-387.
58. Hilpert, K., et al., *Chromium vapor species over solid oxide fuel cell interconnect materials and their potential for degradation processes.* Journal of the Electrochemical Society, 1996. **143**(11): p. 3642.
59. Ebbinghaus, B.B., *Thermodynamics of gas phase chromium species: the chromium oxides, the chromium oxyhydroxides, and volatility calculations in waste incineration processes.* Combustion and Flame, 1993. **93**(1-2): p. 119-137.
60. Froitzheim, J., et al., *Investigation of chromium volatilization from FeCr interconnects by a denuder technique.* Journal of The Electrochemical Society, 2010. **157**(9): p. B1295-B1300.
61. Niewolak, L., et al., *Potential suitability of ferritic and austenitic steels as interconnect materials for solid oxide fuel cells operating at 600 C.* Journal of power sources, 2010. **195**(22): p. 7600-7608.
62. Kendall, K., et al., *Interconnects.* High-Temperature Solid Oxide Fuel Cells 21st Century; Elsevier: London, UK, 2016: p. 195-254.
63. Niewolak, L., et al., *Sigma-phase formation in high chromium ferritic steels at 650 C.* Journal of alloys and compounds, 2015. **638**: p. 405-418.
64. *Alloy Phase Diagrams*. ASM Handbook. Vol. 3. 2016.
65. Sachitanand, R., et al., *Evaluation of the oxidation and Cr evaporation properties of selected FeCr alloys used as SOFC interconnects.* 2013. **38**(35): p. 15328-15334.
66. Ardigo, M.R., et al., *Effect of water vapor on the oxidation mechanisms of a commercial stainless steel for interconnect application in high temperature water vapor electrolysis.* Oxidation of metals, 2013. **79**(5): p. 495-505.
67. Grolig, J.G., J. Froitzheim, and J.-E. Svensson, *Coated stainless steel 441 as interconnect material for solid oxide fuel cells: Oxidation performance and chromium evaporation.* Journal of Power Sources, 2014. **248**: p. 1007-1013.
68. Cheng, F., et al., *Performance of CoNiO spinel oxide coating on AISI 430 stainless steel as interconnect for intermediate temperature solid oxide fuel cell.* international journal of hydrogen energy, 2017. **42**(17): p. 12477-12484.
69. Fergus, J. and Y. Zhao, *Low-chromium alloys for solid oxide fuel cell interconnects.* ECS Transactions, 2011. **35**(1): p. 2447.
70. Stanislowski, M., et al., *Chromium vaporization from high-temperature alloys: I. Chromia-forming steels and the influence of outer oxide layers.* Journal of the Electrochemical Society, 2007. **154**(4): p. A295.
71. Froitzheim, J., et al., *Development of high strength ferritic steel for interconnect application in SOFCs.* Journal of Power Sources, 2008. **178**(1): p. 163-173.
72. Yamamoto, K., *Y, Kimura, F. C-. Wei, Y. Mishima.* Mater. Sci. Eng. A, 2002. **329**: p. 249-254.
73. Froitzheim, J.H., *Ferritic steel interconnectors and their interactions with Ni base anodes in solid oxide fuel cells (SOFC)*. 2008, Lehrstuhl für Werkstoffe der Energietechnik (FZ Jülich).
74. Holt, A. and P. Kofstad, *Electrical conductivity of Cr2O3 doped with TiO2.* Solid State Ionics, 1999. **117**(1-2): p. 21-25.
75. Hou, P. and J. Stringer, *The effect of reactive element additions on the selective oxidation, growth and adhesion of chromia scales.* Materials Science and Engineering: A, 1995. **202**(1-2): p. 1-10.
76. Stringer, J., *The reactive element effect in high-temperature corrosion.* Materials Science and Engineering: A, 1989. **120**: p. 129-137.

77. Pint, B., *Experimental observations in support of the dynamic-segregation theory to explain the reactive-element effect.* Oxidation of metals, 1996. **45**(1): p. 1-37.
78. Naumenko, D., B. Pint, and W.J.O.o.M. Quadakkers, *Current thoughts on reactive element effects in alumina-forming systems: In memory of John Stringer.* 2016. **86**(1-2): p. 1-43.
79. Cotell, C., et al., *The influence of implanted yttrium on the mechanism of growth of Cr/sub 2/O/sub 3/on Cr.* Journal of the Electrochemical Society, 1987. **134**(7): p. 1871-1872.
80. Przybylski, K., A. Garratt-Reed, and G.J. Yurek, *Grain boundary segregation of yttrium in chromia scales.* Journal of the Electrochemical Society, 1988. **135**(2): p. 509.
81. Whittle, D. and J. Stringer, *Improvements in high temperature oxidation resistance by additions of reactive elements or oxide dispersions.* Philosophical Transactions of the Royal Society of London. Series A, Mathematical and Physical Sciences, 1980. **295**(1413): p. 309-329.
82. Quadakkers, W., et al., *Differences in growth mechanisms of oxide scales formed on ODS and conventional wrought alloys.* Oxidation of Metals, 1989. **32**(1): p. 67-88.
83. Fontana, S., S. Chevalier, and G.J.O.o.m. Caboche, *metallic interconnects for solid oxide fuel cell: Performance of reactive element oxide coating during 10, 20 and 30 months exposure.* 2012. **78**(5-6): p. 307-328.
84. Falk-Windisch, H., et al., *Co-and Ce/Co-coated ferritic stainless steel as interconnect material for intermediate temperature solid oxide fuel cells.* Journal of Power Sources, 2017. **343**: p. 1-10.
85. Puranen, J., et al., *Characterization of high-velocity solution precursor flame-sprayed manganese cobalt oxide spinel coatings for metallic SOFC interconnectors.* Journal of thermal spray technology, 2013. **22**(5): p. 622-630.
86. Hu, Y.-Z., et al., *Evolution of microstructure during annealing of Mn1. 5Co1. 5O4 spinel coatings deposited by atmospheric plasma spray.* International journal of hydrogen energy, 2014. **39**(25): p. 13844-13851.
87. Puranen, J., et al., *Influence of powder composition and manufacturing method on electrical and chromium barrier properties of atmospheric plasma sprayed spinel coatings prepared from MnCo2O4 and Mn2CoO4+ Co powders on Crofer 22 APU interconnectors.* International Journal of Hydrogen Energy, 2014. **39**(30): p. 17246-17257.
88. Gannon, P., et al., *Enabling inexpensive metallic alloys as SOFC interconnects: An investigation into hybrid coating technologies to deposit nanocomposite functional coatings on ferritic stainless steels.* International Journal of Hydrogen Energy, 2007. **32**(16): p. 3672-3681.
89. Alvarez, E., et al., *Oxidation kinetics of manganese cobaltite spinel protection layers on Sanergy HT for solid oxide fuel cell interconnect applications.* International Journal of Applied Ceramic Technology, 2011. **8**(1): p. 33-41.
90. Quadakkers, W., et al., *Compatibility of perovskite contact layers between cathode and metallic interconnector plates of SOFCs.* Solid State Ionics, 1996. **91**(1-2): p. 55-67.
91. Stanislowski, M., et al., *Reduction of chromium vaporization from SOFC interconnectors by highly effective coatings.* Journal of Power Sources, 2007. **164**(2): p. 578-589.
92. Mahato, N., et al., *Progress in material selection for solid oxide fuel cell technology: A review.* Progress in Materials Science, 2015. **72**: p. 141-337.
93. Huang, K., P.Y. Hou, and J.B. Goodenough, *Reduced area specific resistance for iron-based metallic interconnects by surface oxide coatings.* Materials Research Bulletin, 2001. **36**(1-2): p. 81-95.
94. Sanchez, M.G., et al., *Scored 2: 0-Steel coatings for reducing degradation.* Report. University of Birmingham, 2017.
95. Reddy, M.J., J.-E. Svensson, and J. Froitzheim, *Reevaluating the Cr Evaporation Characteristics of Ce/Co Coatings for Interconnect Applications.* ECS Transactions, 2021. **103**(1): p. 1899.
96. Holt, A. and P. Kofstad, *Electrical conductivity and defect structure of Cr2O3. I. High temperatures (> ~ 1000° C).* Solid State Ionics, 1994. **69**(2): p. 127-136.
97. Holt, A. and P. Kofstad, *Electrical conductivity and defect structure of Cr2O3. II. Reduced temperatures (< ~ 1000 C).* Solid State Ionics, 1994. **69**(2): p. 137-143.
98. Latu-Romain, L., et al., *Chromia scale thermally grown on pure chromium under controlled p (O2) atmosphere: I. Spallation investigation using photoelectrochemical techniques at a*

mesoscale. Oxidation of Metals, 2018. **90**(3): p. 255-266.
99. Latu-Romain, L., et al., *Towards the growth of stoichiometric chromia on pure chromium by the control of temperature and oxygen partial pressure.* Corrosion Science, 2017. **126**: p. 238-246.
100. Horita, T., et al., *Oxide scale formation on alloy interconnects in CH4 fuels for solid oxide fuel cells.* ECS Proceedings Volumes, 2005. **2005**(1): p. 1822.
101. Navrotsky, A. and O. Kleppa, *The thermodynamics of cation distributions in simple spinels.* Journal of Inorganic and nuclear Chemistry, 1967. **29**(11): p. 2701-2714.
102. Zhao, Y. and J. Fergus, *High temperature oxidation behavior of stainless steel 441 in dual atmosphere-effects of flow rate and humidity.* ECS Transactions, 2009. **16**(44): p. 57.
103. Li, J., et al., *Investigation of anomalous oxidation behavior of SUS430 alloy in solid oxide fuel cell dual atmosphere.* Journal of the Electrochemical Society, 2017. **164**(14): p. C945.
104. Ardigo, M., et al., *Dual atmosphere study of the K41X stainless steel for interconnect application in high temperature water vapour electrolysis.* International Journal of Hydrogen Energy, 2015. **40**(15): p. 5305-5312.
105. Kurokawa, H., K. Kawamura, and T. Maruyama, *Oxidation behavior of Fe–16Cr alloy interconnect for SOFC under hydrogen potential gradient.* Solid State Ionics, 2004. **168**(1-2): p. 13-21.
106. Young, D., et al., *Temperature dependence of oxide scale formation on high-Cr ferritic steels in Ar–H2–H2O.* Corrosion Science, 2011. **53**(6): p. 2131-2141.
107. Sanchez, L., M. Hierro, and F. Perez, *Effect of chromium content on the oxidation behaviour of ferritic steels for applications in steam atmospheres at high temperatures.* Oxidation of Metals, 2009. **71**(3): p. 173-186.
108. Yen, S. and Y. Tsai, *Critical hydrogen concentration for the brittle fracture of AISI 430 stainless steel.* Journal of the Electrochemical Society, 1996. **143**(9): p. 2736.
109. Yang, Z., et al., *Anomalous corrosion behavior of stainless steels under SOFC interconnect exposure conditions.* electrochemical and solid-state letters, 2003. **6**(10): p. B35.
110. Yang, Z., et al., *Oxidation behavior of ferritic stainless steels under SOFC interconnect exposure conditions.* Journal of the Electrochemical Society, 2004. **151**(12): p. B669.
111. Higginson, R. and G. Green, *Whisker growth morphology of high temperature oxides grown on 304 stainless steel.* Corrosion Science, 2011. **53**(5): p. 1690-1693.
112. Leistikow, S., I. Wolf, and H. Grabke, *Effects of cold work on the oxidation behavior and carburization resistance of Alloy 800.* Materials and Corrosion, 1987. **38**(10): p. 556-562.
113. Grabke, H., et al., *Effects of grain size, cold working, and surface finish on the metal-dusting resistance of steels.* Oxidation of Metals, 1998. **50**(3): p. 241-254.
114. Holcomb, G.R., et al., *Dual-environment effects on the oxidation of metallic interconnects.* Journal of Materials Engineering and Performance, 2006. **15**(4): p. 404-409.
115. Lundberg, M.W., et al., *Novel multilayered PVD-coating in a roll to roll mass production process.* ECS Transactions, 2013. **57**(1): p. 2203.
116. Sand, T., *High Temperature Corrosion Behaviour of Ni-base Alloys and FeCrAl Alloys–The Influence of Water Vapour*. 2019: Chalmers Tekniska Hogskola (Sweden).
117. Fournier-Salaün, M.-C. and P. Salaün, *Quantitative determination of hexavalent chromium in aqueous solutions by UV-Vis spectrophotometer.* Central European Journal of Chemistry, 2007. **5**(4): p. 1084-1093.
118. Egerton, R.F., *Physical principles of electron microscopy*. 2005: Springer.
119. Zhou, W., et al., *Fundamentals of scanning electron microscopy (SEM)*, in *Scanning microscopy for nanotechnology*. 2006, Springer. p. 1-40.
120. Egerton, R., *An introduction to microscopy*, in *Physical Principles of Electron Microscopy*. 2016, Springer. p. 1-26.
121. Smart, L.E. and E.A. Moore, *Solid state chemistry: an introduction*. 2016: CRC press.
122. Grolig, J.G., *Coated Ferritic Stainless Steels as Interconnects in Solid Oxide Fuel Cells.* 2013.
123. Grolig, J.G., J. Froitzheim, and J.-E. Svensson, *Coated stainless steel 441 as interconnect material for solid oxide fuel cells: Evolution of electrical properties.* Journal of Power Sources, 2015. **284**: p. 321-327.
124. Canovic, S., et al., *Oxidation of Co-and Ce-nanocoated FeCr steels: A microstructural*

investigation. Surface and Coatings Technology, 2013. **215**: p. 62-74.
125. Talic, B., et al., *Diffusion couple study of the interaction between Cr2O3 and MnCo2O4 doped with Fe and Cu.* Solid State Ionics, 2019. **332**: p. 16-24.
126. Molin, S., et al., *Low temperature processed MnCo2O4 and MnCo1. 8Fe0. 2O4 as effective protective coatings for solid oxide fuel cell interconnects at 750 C.* Journal of Power Sources, 2016. **336**: p. 408-418.
127. Goebel, C., et al., *Does the conductivity of interconnect coatings matter for solid oxide fuel cell applications?* Journal of Power Sources, 2018. **383**: p. 110-114.
128. Reisert, M., et al. *Preformed Oxide Scale Chemistry and Its Influence on Local Metal Loss During Dual Atmosphere Corrosion*. in *TMS 2020 149th Annual Meeting & Exhibition Supplemental Proceedings*. 2020. Springer.
129. Falk-Windisch, H., et al., *Chromium vaporization from mechanically deformed pre-coated interconnects in Solid Oxide Fuel Cells.* Journal of Power Sources, 2015. **297**: p. 217-223.
130. Matsumura, T., *The electrical properties of alumina at high temperatures.* Canadian Journal of Physics, 1966. **44**(8): p. 1685-1698.
131. Insley, R.H., *Electrical properties of alumina ceramics*, in *Alumina chemicals: Science and technology handbook*. 1990, The American Ceramic Society Westerville, OH. p. 293-297.

Appended Publications 1 - 2

Publication 1

Efficiencies of cobalt- and copper-based coatings applied by different deposition processes for applications in intermediate-temperature solid oxide fuel cells

M. Tomas[a], V. Asokan[a], J. Puranen[b], J-E. Svensson[a] and J. Froitzheim[a]

[a]Energy and Materials, Chalmers University of Technology
Kemivägen 10, 41296 Gothenburg, Sweden
tommat@chalmers.se

[b]Elcogen OY
Niittyvillankuja 4, Vantaa 01510, Finland
jouni.puranen@elcogen.com

Abstract

Solid Oxide Fuel Cells (*SOFCs*) are electrochemical conversion devices that produce electricity directly by oxidising a fuel. The interconnects between the individual cells need to be coated to limit chromium evaporation from the steel and to preserve electrical conductivity. Physical Vapour Deposition (PVD)-coated samples with Ce/Co, Ce/Cu, and Ce/MnCu, and Thermal Spray (TS)-coated Mn/Co, Cu and Mn/Cu and AISI 441 steel samples were exposed at 650°C for up to 1,000 h. The PVD Ce/Co and Ce/Cu coatings, as well the TS Mn/Co coating exhibited the formation of thin protective Cr_2O_3 scales underneath the coating. These samples also exhibited the lowest area-specific resistance (ASR) values. The remainder of the samples exhibited much higher mass gains and higher ASR values. Cr(VI) evaporation measurements showed that all the coatings behaved approximately the same despite the PVD coatings being only about one-tenth of the thickness of the TS coatings.

KEYWORDS: SOFC, interconnect, Cu coatings, PVD, Thermal Spray, area specific resistance

Introduction

As a consequence of increased electricity consumption, power production has become one of the most important issues in Society today [1]. Many systems exist to produce more-sustainable electricity, e.g., solar panels, wind turbines, geothermal, and fuel cells. Fuel Cell (FC) technologies are promising because they exhibit high levels of efficiency, low levels of emissions (NO_x, SO_x, CO_2, etc.), and are versatile. There most-common types of FCs are Proton-Exchange Membrane Fuel Cells (PEMFCs) and Solid Oxide Fuel Cells (SOFCs) [2]. While PEMFCs use platinum as a catalyst for the reaction to occur at a sufficiently rapid pace, SOFCs operate at high temperatures (≥500°C) and, thus, do not need expensive catalysts. These systems have different advantages and disadvantages.

On the one hand, PEMFCs have the major drawback that they can only operate with high-purity H_2 as fuel [3]. On the other hand, SOFCs operate at high temperatures, entailing longer start-up times. However, SOFCs are extremely versatile in terms of the fuels that they can use. Given their high electrical efficiency (>60%), low levels of emissions, and fuel flexibility, they represent a promising technology for future energy applications [4-7]. However, poor stability and high cost have limited the commercialisation of SOFCs. One of the key components of an SOFC is the interconnect [8]. Several cells are connected in series to form an FC stack, which forms the core of the FC system. Each cell is electrically connected *via* an interconnect. The interconnects have to fulfil the following requirements: a thermal expansion coefficient (TEC) close to that of the ceramic parts of the cell; low electrical resistance; impermeable to gases; easy to shape; and stability in both high and low pO_2 environments (air on the cathode side and fuel on the anode side) [9, 10]. Reduction of the operating temperature of the cell from 1000°C to 850°C–600°C, depending on the FC system, allows the use of Ferritic Stainless Steels (FSS) [10]. However, FSS suffer from two major issues under SOFC operating conditions: a) Cr(VI) evaporation from the steel, which poisons the cathode [11]; and b) the growth of a Cr_2O_3 layer, which reduces the electrical conductivity [12]. Nevertheless, steels such as Crofer 22 APU have been used successfully in recent years due to their low production costs, as compared to ceramic interconnects, such as $LaCrO_3$. When exposed to high temperature and a humid atmosphere, ($CrO_2(OH)_2$) evaporates from the metallic interconnect. To mitigate Cr(VI) vapourisation, the interconnects have to be coated. In the last few years, various coatings have been studied and proposed. Commonly used are manganese (Mn)- and cobalt (Co)-based spinel coatings (Mn/Co), and modified forms of these are considered to be state-of-the-art coatings for this application [13-16]. Instead of applying Mn/Co directly to the steel, a thin metallic layer (600-nm-thick) of Co can be applied [17, 18]. This layer will be

oxidised to form Co_3O_4 and will be enriched with Mn through diffusion from the steel substrate during stack operation at high temperatures. Previous research [19] has shown that the steel strip can be pre-coated with metallic Co and pressed into the desired interconnect shape without increasing Cr(VI) vapourisation. This allows for the mass production of coated interconnects, which reduces the production cost and the eventual price of the interconnects. When oxidised, interconnects form a Cr_2O_3 layer at the metal/oxide interface and a $(Cr, Mn)_3O_4$ spinel top layer that is moderately conductive in the temperature range of the SOFC. As alternatives to Co, different copper-based coatings have been investigated [20-23]. These copper-based coatings behave differently depending on the atmosphere and the deposition process used. In a humid atmosphere, Cu-based coatings decrease corrosion resistance at high temperature (around and above 800°C) and result in rapid oxidation. *Petric et al.* [24] have shown that copper spinel oxides are highly conductive, with the highest conductivity being detected for $Cu_{1.3}Mn_{1.7}O_4$ at 225 $S \cdot cm^{-1}$ at 750°C. They concluded that the best candidates for interconnects are ferrite spinels, such as $CuFe_2O_4$, and manganite spinels, such as $Mn_xCo_{3-x}O_4$ or $Cu_xMn_{3-x}O_4$. The utilisation of copper rather than cobalt confers several advantages. For example, the European Union classifies Co as a critical raw material [25]. In addition, cobalt mining is frequently associated with exploitation and child labour [26]. Furthermore, copper is cheaper (10 USD/kg for Cu vs. 70 USD/kg for Co) and less toxic (in dust form) than cobalt (in dust form), and therefore entails a lower risk for health issues [26, 27].

The coatings investigated in the present work are coated Ce/Cu, Ce/MnCu, and Ce/Co (as a reference) coatings. Furthermore, the PVD-applied coatings are compared to a series of TS coatings: TS Cu, TS Mn/Cu oxide, and TS Mn/Co oxide. The aim of this study was to compare the efficiencies of these coatings with respect to the suppression of Cr evaporation and protection against corrosion. Furthermore, two different deposition processes were compared.

Experimental

The characteristics and compositions of the materials used in this study are listed in TABLE *VI*I and TABLE *VII*I, respectively.

AISI 441 steel was chosen as the substrate, and the samples were coated on both sides. All the samples produced by Physical Vapour Deposition (PVD) were coated by Sandvik Materials Technology AB and contained a cerium (Ce) layer closest to the substrate [28]. The TS-generated samples were coated by Kuopion Konepaja Oy [13, 15, 29, 30]. PVD Ce/Co-coated samples with coated edges were also investigated, to compare the Cr evaporation levels with the TS coatings.

TABLE I. Characteristics of the materials used. The coating was applied to the substrate sheets, and the samples were cut out of the steel sheets in the form of 1.5 cm × 1.5 cm coupons.

Material	Deposition process	Coating	
		Inner	Outer
AISI 441	PVD	20 nm Ce	600 nm Cu
AISI 441	PVD	20 nm Ce	600 nm Mn/Cu
AISI 441	PVD	20 nm Ce	600 nm Co
AISI 441	TS	10 µm Cu oxide	
AISI 441	TS	10 µm Mn/Cu oxide	
AISI 441	TS	10 µm Mn/Co oxide	
AISI 441	None	Uncoated	

TABLE II. Composition of the substrate steel material in weight %, as specified by the manufacturer.

Materials	Fe	Cr	C	Mn	Si	Ni	Ti	Nb	Al	N	P	S
AISI 441 Batch: 89893	Bal.	17.53	0.016	0.40	0.59	0.15	0.172	0.41	0.007	0.015	0.024	<0.001

Exposures were carried out in horizontal tube furnaces in air that contained 3% water vapour using an air flow of 6,000 $S \cdot min^{-1}$ for up to 1,000 h. The mass gain was recorded each week throughout the exposure in a separate experiment. The samples were weighted using a METTLER TOLEDO XP6 scale accurate to the tenth of a microgram.

Cr Evaporation

Cr(VI) vapourisation is a significant issue for the longevity of the FC stack. Therefore, it is necessary to quantify the rate of Cr evaporation during the exposure. The Cr vapourisation was measured for all samples using the denuder technique, which allows *in situ* determination of Cr evaporation. A detailed description of the Cr-evaporation measurement procedure can be found elsewhere [31]. Two sets of three samples were exposed in a tubular furnace for 6 weeks, and Cr evaporation measurements were performed on each week.

Electron Microscopy

Cross-sections of coated AISI 441 samples exposed for 24 h and 1,000 h were prepared using the Leica EM TIC 3X Broad Ion Beam (BIB) with an acceleration voltage of 8 kV. The resulting cross-sections were analysed using the JEOL 7800F Prime SEM and FEI Titan 80-300 TEM. SEM Imaging was performed with an acceleration voltage of 10 kV, and Energy Dispersive x-ray (EDX) analysis was carried out with an acceleration voltage of 15 kV. The TEM analysis was performed on a lift-out lamella from the surface realised using the FEI Versa3D Focused Ion Beam (FIB).

Area-Specific Resistance (ASR) Measurement

The samples exposed for 1,000 h were mounted in a ProboStat™ (NorECs, Norway) measurement cell using a platinum [10] wire and grid to contact the sample electrodes. The resistance was measured by the 2-point, 4-wire method at 650°C in air. The ASR was monitored to check for semi-conductive behaviour as the samples cooled down. The electrical resistance is characterised by the ASR, which is the measured resistance (R) multiplied by the contact area (A). The measured values are divided by two to account for both surfaces of the sample. A sputter mask of 10×10 mm^2 was placed on a pre-oxidised sample, and the sample was then sputtered with gold for 30 minutes using the Quorum 150 sputter coater and a sputter current of 60 mA. This procedure was then repeated for the reverse side of the sample. The sputtering step was used to produce electrodes with a defined area and to ensure adequate contacts between the sample and the platinum electrodes.

Results & Discussion

Gravimetric Analysis

Figure 32a shows the average mass gains of the materials exposed at 650°C in humid air for 1,000 h. The uncoated samples exhibited a paralinear behaviour. After 1 week of exposure, the uncoated sample showed a slight increase in mass to $0.069 \cdot 10^{-2}$ mg·cm^{-2}, which was followed by a mass loss corresponding to -0.021 mg·cm^{-2} after 1,000 h of exposure. *Tedmon et al.* [32] have explained this phenomenon in terms of a combination of parabolic growth and mass loss due to vapourisation. In the initial stages of the oxidation process, when the rate of scale growth is significantly higher than the rate of vapourisation, the mass gain follows an approximately parabolic oxidation behaviour. However, once the oxide scale has reached a limiting thickness, the oxide-scale growth rate decreases to become equal to the rate of Cr vapourisation from the oxide scale. At this point, the oxide scale thickness remains constant, and a continuous loss of mass is observed.

All of the coated samples exhibited rapid mass gains during the first 24 h of exposure, and thereafter this levelled off to give slow mass gains. The PVD Ce/Cu-coated samples show mass gains that were very similar to those of the PVD Ce/Co-coated samples. After 24 h, the measured mass gain for PVD Ce/Cu-coated samples was 0.18 mg·cm^{-2}; this matches well with the theoretical value for converting 600 nm Cu into CuO (~0.13 mg·cm^{-2}).

In comparison, the PVD Ce/Co-coated samples displayed a mass gain of 0.25 mg·cm^{-2} after 24 h, which also matches well with the theoretical value (~ 0.19 mg·cm^{-2}). After 1,000 h of exposure, the mass gain was 0.21 mg·cm^{-2} for PVD Ce/Cu and 0.26 mg·cm^{-2} for PVD Ce/Co. These results agree very well with the data reported previously by *Falk-Windisch et al.* [33].

The Ce/MnCu-coated samples displayed a rapid mass gain (0.67 mg·cm^{-2}) during the first 24 h of exposure, and this continued to increase to 0.99 mg·cm^{-2} after 1 week of exposure (168 h), after which it levelled off for the remainder of the exposure period.

The TS Mn/Co coating displayed an initial mass gain of 0.31 mg·cm^{-2}. Thereafter, the mass gain of the sample remained almost constant, in similarity to the PVD Ce/Co and Ce/Cu coatings after 1,000 h. This indicates that the TS Mn/Co coating is almost fully oxidised at the beginning of the exposure.

This is not the case for either the TS Cu or TS Mn/Cu coatings, which exhibited a strong mass gain in the first 24 h of exposure (~2 mg·cm^{-2}), and thereafter a slowing of the rate of mass gain. After the first week, the mass gain was minimal throughout the remainder of the exposure.

It seems likely that during deposition not all of the coating was oxidised, such that a part remained in a metallic state. When exposed at high temperature, the metallic part of the coating became oxidised, causing the rapid mass gain observed in the early hours of the exposure. The TS Mn/Cu coating exhibited a slightly higher mass gain than the TS Cu coating.

Cr Evaporation Measurements

The cumulative Cr-evaporation for uncoated and coated AISI 441 samples exposed for 1,000 h at 650°C is plotted as a function of time in Figure 32b. Uncoated samples displayed a very high accumulated Cr-vapourisation level of about 0.08 $mg \cdot cm^{-2}$ after 1,000 h of exposure in humid air. This is in line with previous results from *Falk-Windisch et al.* [34]. In contrast, Ce/Cu-coated samples exhibited a lower Cr-evaporation level, at around $7 \cdot 10^{-3}$ $mg \cdot cm^{-2}$ on average, after 1,000 h of exposure in 3% water vapour. The Ce/MnCu-coated samples displayed a Cr-vapourisation level of $7.5 \cdot 10^{-3}$ $mg \cdot cm^{-2}$ on average after 1,000 h of exposure. The Cr(VI) evaporation measured for the Ce/Co-coated samples was $4.4 \cdot 10^{-3}$ $mg \cdot cm^{-2}$ on average after 1,000 h of exposure. However, this difference should not be over-interpreted, as all the values are very low. A recently published study [35] has shown that samples with coated edges have significantly lower Cr-evaporation levels than the same samples with uncoated edges. To account for this and to compare the PVD coatings (uncoated edges) with the TS coatings with coated edges, a set of Ce/Co-coated samples with coated edges was measured. After 1,000 h of exposure, the Ce/Co samples with coated edges exhibited a Cr(VI)-evaporation level of $1.3 \cdot 10^{-3}$ $mg \cdot cm^{-2}$ after 1,000 h of exposure. Thus the real value for the Ce/Co-coated edges coating is only one-third of the value measured for the uncoated edges, which is in accordance with previous results [35]. The same factor should be applied to the other PVD coatings with uncoated edges. The TS Cu-coated samples displayed a Cr(VI)-evaporation level of $0.3 \cdot 10^{-3}$ $mg \cdot cm^{-2}$ after 1,000 h of exposure, while the TS Mn/Cu-coated samples exhibited a Cr-vapourisation level of $0.062 \cdot 10^{-3}$ $mg \cdot cm^{-2}$ after 1,000 h of exposure. Those values are very similar, and both coatings should be considered equivalent in terms of their capacities to mitigate Cr(VI) evaporation. The reference TS Mn/Co-coated samples showed a Cr-vapourisation rate of $0.06 \cdot 10^{-3}$ $mg \cdot cm^{-2}$ after 1,000 h of exposure, which is similar to the values obtained for the TS Cu- and TS Mn/Cu-coated samples [17, 36].

In summary, PVD coatings are as good as TS coatings with respect to mitigating Cr evaporation when the edges are coated, while the coating thickness is thinner by a factor of 10 for the PVD coatings (~1 μm for PVD compared to ~10 μm for TS). This demonstrates the high efficiency

of converting a thin metallic coating into a protective oxide at high temperatures.

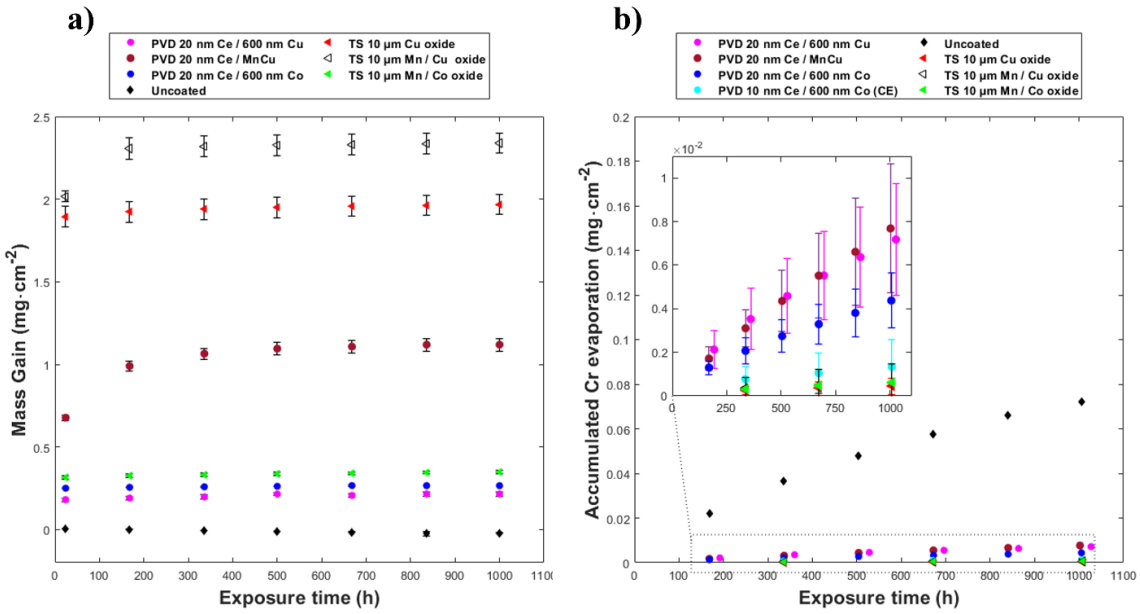

Figure 32. a) Average mass gains and b) Cumulative Cr-evaporation level as a function of time for PVD Ce/Cu-coated samples (magenta circles), PVD Ce/MnCu-coated samples (brown circles), PVD Ce/Co-coated samples (blue circles), TS Cu-coated samples (red triangles), TS Mn/Cu-coated samples (empty triangles), and uncoated samples (black diamonds), all of which were exposed for 1,000 h at 650°C in air that contained 3% water vapour. Error bars indicate standard deviation.

Microstructural Investigation

1. *PVD 20 nm Ce / 600 nm Co*

A cross-section of the Ce/Co-coated sample is depicted in Figure 33. Figure 33a shows the microstructure of the sample after 24 h of exposure. The top layer is composed of a homogeneous Co_3O_4 spinel, which has a thickness of approximately 1 µm thick, and some pores are evident in this cap layer. A Cr_2O_3 layer is present closest to the metal and is approximately 200 nm in thickness. At the spinel/chromia interface, a thin CeO_2 layer can be observed. After 1,000 h of exposure, the sample microstructure is very similar to that at 24 h. The main difference is the diffusion, in the latter, of Mn from the bulk to the cap layer to form a $(Co, Mn)_3O_4$ spinel layer. The chemical analyses at 24 h of exposure and 1,000 h of exposure support this observation. Low-level diffusion of Mn (roughly 5 at%) is apparent after 1,000 h of exposure.

These results accord with the mass gain measurements. After the first 24 h of exposure, the sample mass gain increasing slightly during the remainder of the exposure period, which is in

agreement with the previous findings of *Falk-Windisch et al.* [33] for samples exposed under the same conditions.

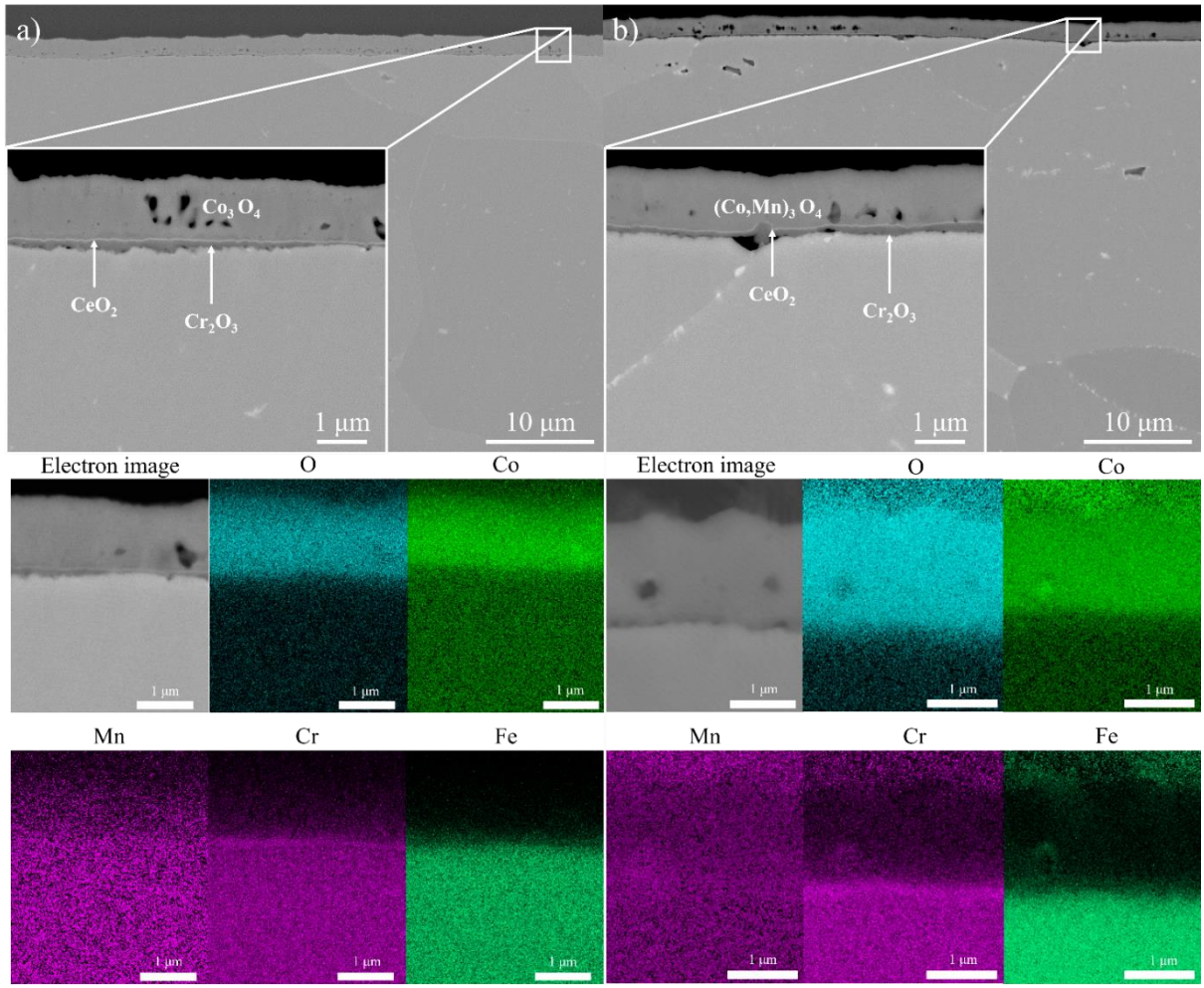

Figure 33. a) SEM-Backscattered Electron (BSE) image of a BIB-milled cross-section of the PVD Ce/Co-coated AISI 441 exposed for 24 h at 650°C in air + 3% water vapour. b) SEM-BSE image of a BIB-milled cross-section of the PVD Ce/Co-coated AISI 441 exposed for 1,000 h at 650°C in air + 3 % water vapour, together with the corresponding EDS analysis.

2. PVD 20 nm Ce / 600 nm Cu

The SEM micrographs and the corresponding EDX analysis of a cross-section of an exposed Ce/Cu-coated sample are shown in Figure 34. Figure 34a depicts the sample microstructure after 24 h of exposure. A homogeneous oxide scale mainly covers the surface at an overall thickness of approximately 1 µm. The oxide scale consists of three layers. The top layer has been identified as CuO, the middle layer as a thin spinel oxide, and the third layer as a very thin Cr_2O_3 layer at the metal/oxide interface. Apart from the base oxide, a few oxide nodules (roughly 2 µm in thickness) are spread haphazardly over the surface. These nodules appear to grow an Fe-rich phase under the CuO top layer. Underneath this Fe-rich layer, a $(Fe,Cr)_3O_4$

layer is present, and a Cr_2O_3 layer is found at the metal/oxide interface. Some pores can be seen beneath the CuO cap layer within the nodules.

Figure 34b shows the microstructure of a Ce/Cu-coated sample after 1,000 h of exposure. The microstructure is very similar to that seen after 24 h of exposure. The main difference is the presence, in the latter, of an intermediate spinel underneath the CuO cap layer. Overall, the oxide layers formed on the Ce/Cu coating are homogeneous but contain more pores than those formed on the Ce/Co coating [33]. Within the steel, mainly along the grain boundaries, Nb and Si were observed, indicating the presence of laves phases. The high degree of similarity between the microstructures observed for the 24 h and 1,000 h exposures is in line with the observed mass gain curve. The increase in mass within the first 24 h is due to oxidation of the metallic Cu layer and the formation of nodules. The slight increase in sample mass after 24 h of exposure is attributed to the growth of the intermediate layer resulting from the diffusion of Mn, Cr, and Fe and the formation of a Cr_2O_3 layer at the metal/oxide interface.

For a more detailed investigation of the base oxide, EDS analysis on STEM image was performed (Figure 34c). The findings are in line with the SEM observations. There is a relatively pure CuO cap layer of roughly 1 μm in thickness, followed by a thin spinel layer (~300 nm) with high levels of Cu (~40 cation%), Cr (~30 cation%) and Mn (~20 cation%), as well as the presence of Fe in small quantities. *Talic et al.* [37] have suggested that there is faster diffusion of Cr when Cu is present within the spinel. This might explain the high concentration of Cr within the intermediate spinel detected in the TEM elemental analysis. Within the spinel layer, CeO_2 (white line) is evident (see Figure 34c). Closest to the metal, a Cr_2O_3 layer has been formed, which is slightly thicker at the grain boundaries.

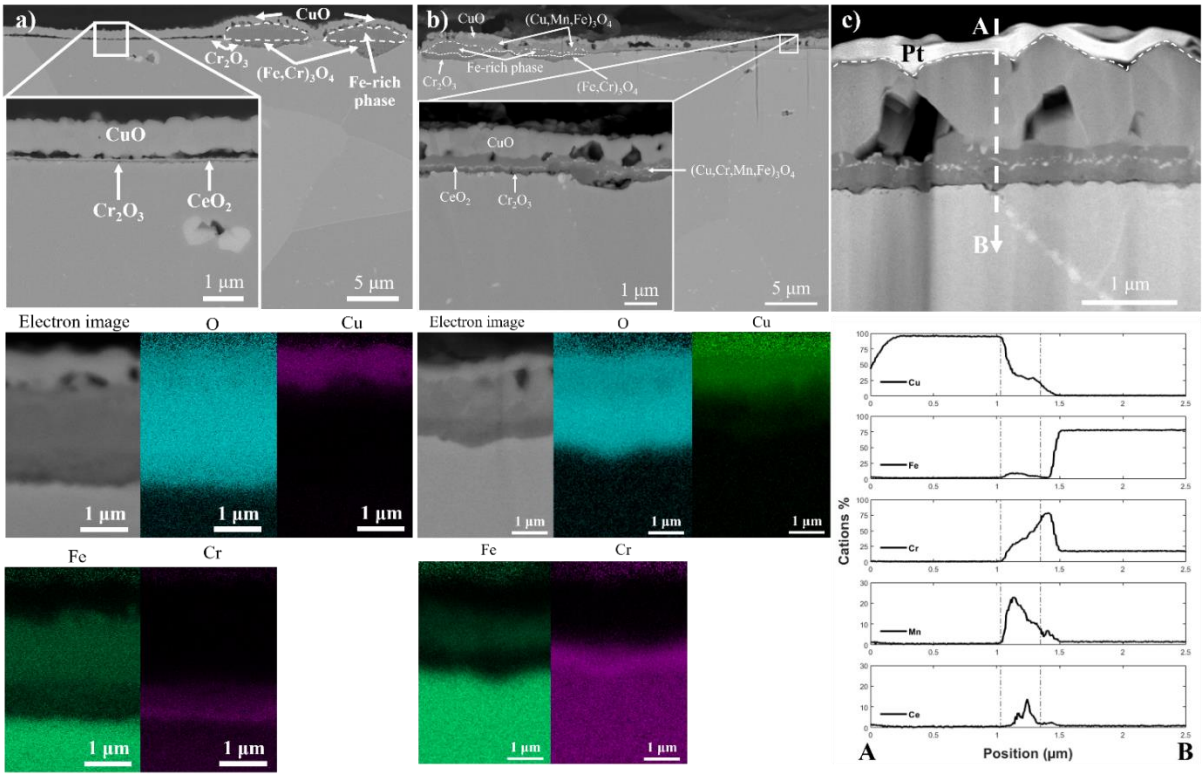

Figure 34. a) SEM-Backscattered Electron (BSE) image of a BIB-milled cross-section of the PVD Ce/Cu-coated AISI 441 exposed for 24 h at 650°C in air + 3% water vapour. b) SEM- BSE image of a BIB-milled cross-section and c) STEM analysis of the PVD Ce/Cu-coated AISI 441 exposed for 1,000 h at 650°C in air + 3% water vapour. For a) and b), the corresponding EDS analysis represents the chemical analysis of the nodules.

3. PVD 20-nm Ce / MnCu

The microstructural analysis of the Ce/MnCu-coated sample is shown in Figure 35. Figure 35a represents the sample exposed for 24 h, and Figure 35b depicts the sample exposed for 1,000 h. In both cases, in similarity to the Ce/Cu-coated sample, the oxide scale comprises two microstructures. A thin homogeneous part with thickness of about 1 µm is interrupted by nodules that are up to 10 µm in thickness. However, in the case of Ce/MnCu, the nodules are more numerous than in the case of Ce/Cu. The mass gain curve indicates some oxide growth after 24 h of exposure (~0.3 $mg \cdot cm^{-2}$), and this correlates with the micrographs that show that the nodules cover most of the sample. Figure 35a shows that after 24 h of exposure, the homogeneous area displays a top layer composed of an $(Mn,Cu)_3O_4$ spinel layer, and closest to the metal, a Cr_2O_3 layer is identified. The nodule exhibits a top layer composed of Cu and Mn, an Fe-rich oxide middle layer, and a $(Fe,Cr)_3O_4$ layer underneath. An internal oxidation zone is partially encapsulated by a Cr_2O_3 layer (see Figure 35a).

After 1,000 h of exposure, the homogeneous area (see Figure 35b) shows two different layers. The top layer appears to be a $(Cu,Mn,Fe)_3O_4$ spinel layer. Meanwhile, the oxide layer at the

metal/oxide interface was identified as Cr_2O_3. The chemical analysis of the homogeneous layer indicates that the concentration of Cu is higher at the chromia scale interface, whereas the concentration of Mn is higher in the top layer. Fe is also present in the top layer, indicating Fe diffusion from the bulk to the cap layer. The nodules show a microstructure that is similar to the homogeneous area but with a different chemical distribution. It appears that the Fe-rich oxide is sandwiched between two Cu-rich layers, while Mn is only present at the top of the oxide. This phenomenon might be attributable to the deposition process (co-deposition of Cu and Mn), which generates a non-homogeneous mix of the elements. The chemical analysis revealed small amounts of Cr and Fe in the top layer. A chromia layer was identified closest to the substrate. A thin ceria layer was observed at the cap layer / chromia interface (insert in Figure 35b). Laves phases are present inside the bulk, and some Si and Nb are observed along the grain boundaries. The formed layers are continuous and dense, with the consequence that there is a low rate of Cr evaporation throughout the exposure.

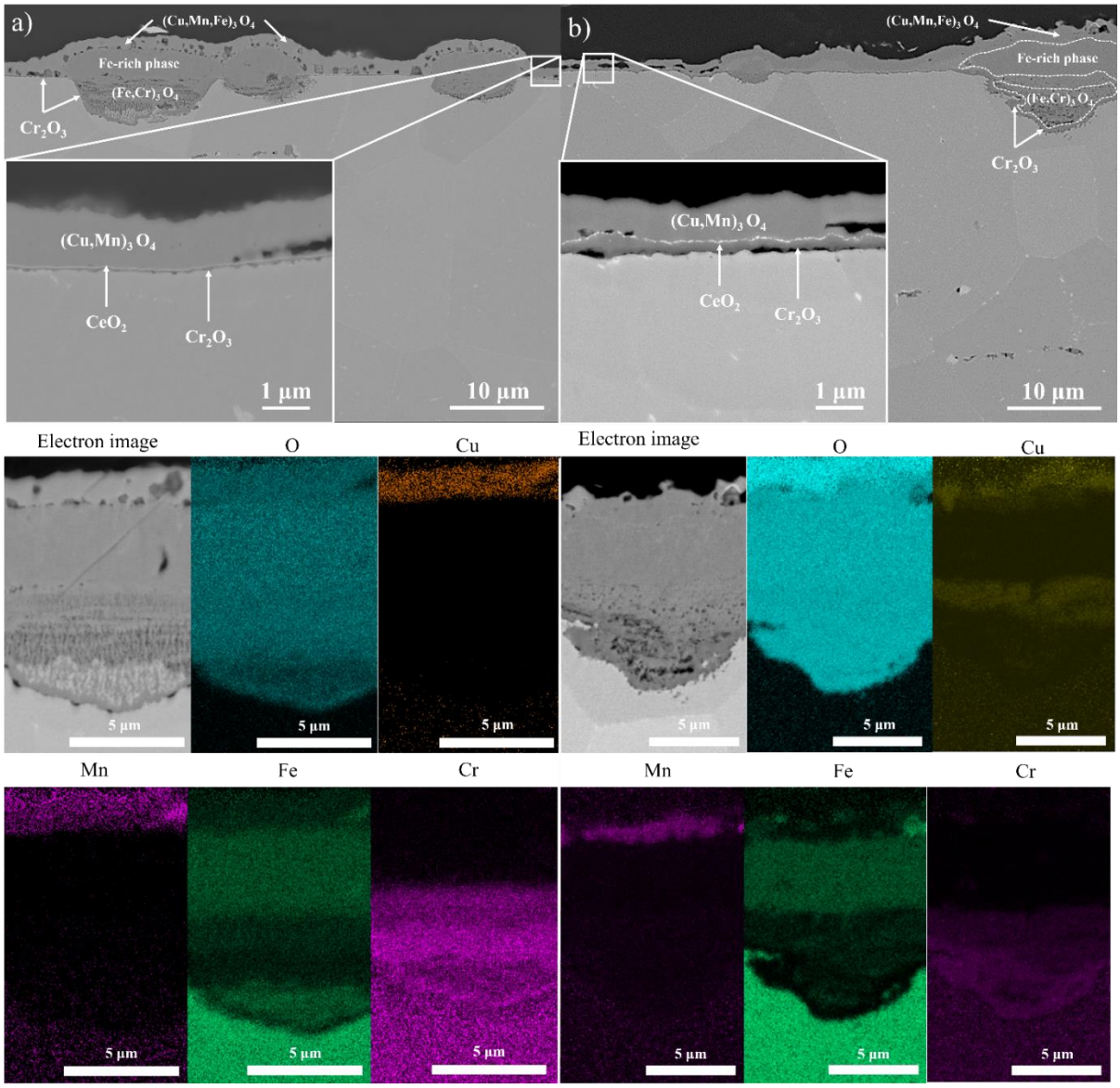

Figure 35. a) SEM-Backscattered Electron (BSE) image of a BIB-milled cross-section of the PVD Ce/MnCu-coated AISI 441 exposed for 24 h at 650°C in air + 3% water vapour. b) SEM- BSE image of a BIB-milled cross-section of the PVD Ce/MnCu-coated AISI 441 exposed for 1,000 h at 650°C in air + 3% water vapour. The corresponding EDS analysis represents the chemical analysis of the nodules.

4. TS Mn/Co

Figure 36 depicts the microstructure of the TS Mn/Co-coated sample in the absence of exposure, and after 24 h and 1,000 h of exposure, together with the corresponding EDS analysis. Figure 36a shows a cross-section of the as-received material. The initial thickness is about 10 µm, and the coating has a rough surface. After 24 h of exposure (see Figure 36b), a homogeneous and thick (~10 µm) $(Mn,Co)_3O_4$ spinel layer can be observed on top, while a very thin Cr_2O_3 layer (of around 200 nm) is visible at the metal/oxide interface. The Mn/Co layer is relatively porous, possibly due to the deposition process [29]. After 1,000 h of exposure, the

microstructure did not change significantly. The thickness of the top Mn/Co layer remained the same, and the thickness of the chromia beneath was essentially identical in appearance. No other corrosion products were detected. This is in accordance with the mass gain measurements, which were stable throughout the exposure. The lack of a ceria layer does not seem to affect the oxide scale growth, which is still in the same range as those of the PVD-coated samples, which contain a CeO_2 layer. The very low rate of Cr evaporation can be explained by the relatively thick top Mn/Co layer.

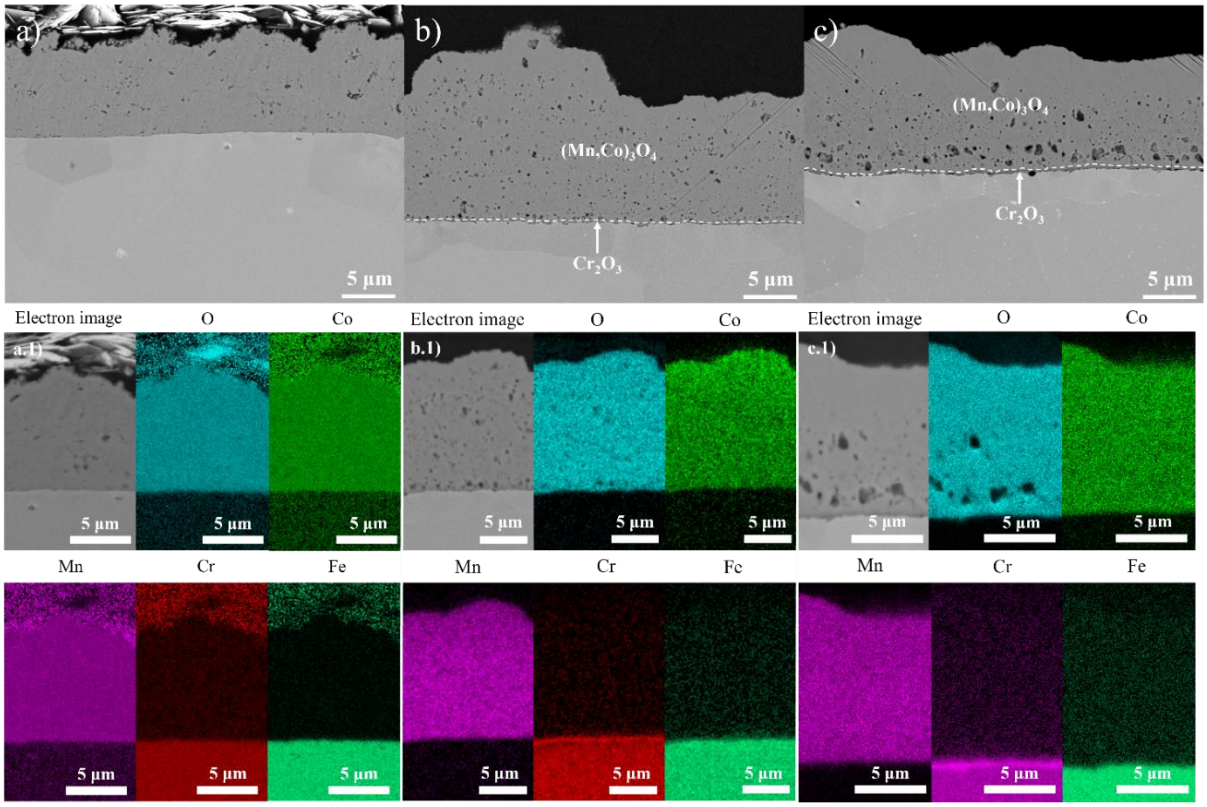

Figure 36. a) BIB-milled cross-section of the TS Mn/Co-coated sample in the absence of exposure. b) BIB-milled cross-section of the TS Mn/Co-coated sample exposed at 650°C in humid air for 24 h. c) BIB-milled cross-section of the TS Mn/Co-coated sample exposed at 650°C in humid air for 1,000 h, together with the corresponding EDS analysis.

5. *TS Cu*

Figure 37 depicts the microstructural analysis of the TS Cu oxide coating at different exposure times and the corresponding EDS analysis. The as-coated sample (see Figure 37a) displays a roughly 10-µm-thick coating. EDS analysis showed that part of the coating was still in a metallic state, which is in accordance with the previous assumption regarding the large increase in mass gain at the beginning of the exposure. After 24 h of exposure (see Figure 37b), the cross-section displayed a top layer of CuO. Beneath it, an Fe-rich oxide layer can be found,

followed by an $(Fe,Cr)_3O_4$ spinel layer, and at the metal/oxide interface, a thin Cr_2O_3 layer. The total final thickness is around 20 µm, which is twice as thick as the initial thickness. The CuO top layer is about 10 µm in thickness, which corresponds to the initial thickness of the deposited oxide. The corresponding EDS analysis confirmed the presence of an iron-rich intermediate oxide layer. After 1,000 h of exposure (see Figure 37c), the microstructure did not change, and the oxide layers remained virtually identical. The oxide layers were dense and homogeneous. This is in accordance with the mass gain observation. The high mass gain observed within the first 24 h can be explained by the thick Fe-rich oxide layer formed between the CuO layer and the $(Fe,Cr)_3O_4$ layer. The low level of Cr evaporation observed throughout the exposure is due to the thick oxide layers on top of the metal, which constitute a Cr barrier.

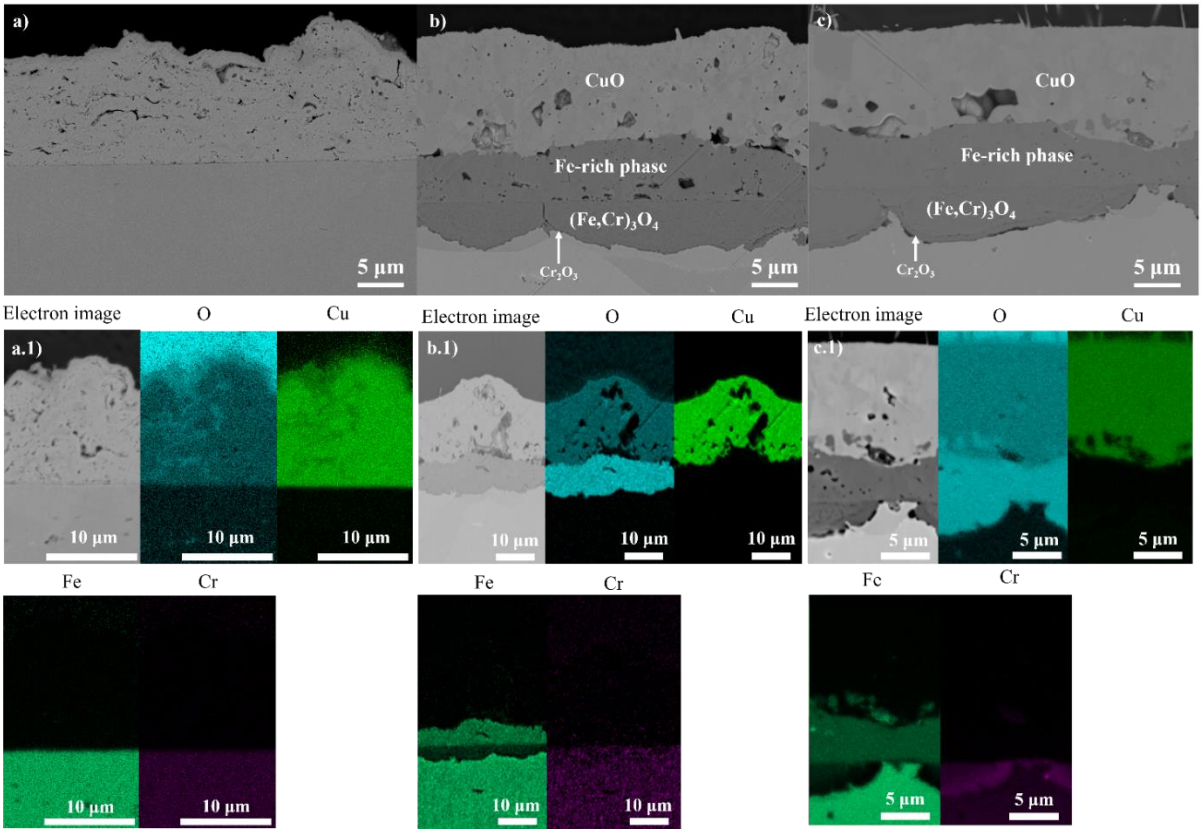

Figure 37. a) BIB-milled cross-section of the TS Cu-coated sample without exposure. b) BIB-milled cross-section of the TS Cu-coated sample exposed at 650°C in humid air for 24 h. c) BIB-milled cross-section of TS Cu-coated sample exposed at 650°C in humid air for 1,000 h with the corresponding EDS analysis.

6. TS Mn/Cu

The cross-sections of the TS Mn/Cu-coated sample are depicted in Figure 38. Figure 38a exhibits a 10-µm-thick as-received coating. The EDS analysis shows that not all of the coating is oxidised. This might explain in part the high mass gain at the beginning of the exposure. After 24 h of exposure (see Figure 38b), the micrograph shows six different types of oxides: the top layer is constituted of a CuO oxide layer, while beneath it lie a (Cu, $Mn)_3O_4$ layer and an Mn-rich layer. The presence of these three phases could be linked to the deposition process, i.e., TS powder-precursor. Beneath the top three layers, the cross-section exhibits the corrosion products: an iron-rich oxide layer, a $(Fe,Cr)_3O_4$ layer, and finally, at the metal/oxide interface, a continuous Cr_2O_3 layer. The Fe-rich oxide layer seems to be relatively porous. One can assume that the Fe-rich oxide scale was formed by the mean diffusion of O^{2-} ions through the oxidised coating during the exposure, as seen before for the TS Cu oxide. The presence of the Fe-rich oxide layer after 24 h of exposure could explain the high mass gain at the start of the exposure. After 1,000 h of exposure (see Figure 38c), the microstructure is similar to that seen after 24 h of exposure. The main difference is the diffusion, in the latter, of Fe into the Mn-rich oxide layer to form a $(Mn,Fe)_3O_4$ spinel. The low level of Cr evaporation measured throughout the exposure is attributed to the thick layers present on top of the substrate, which reduces the Cr diffusion rate.

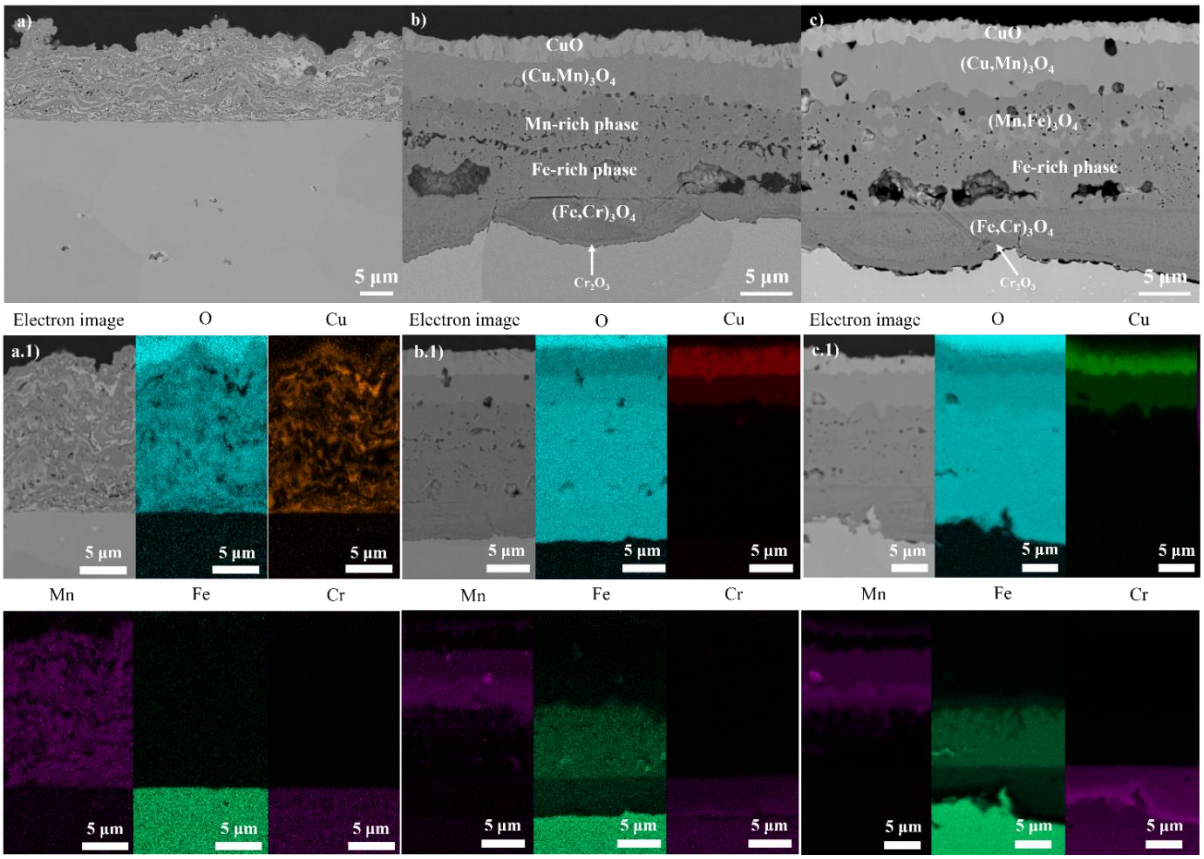

Figure 38. a) BIB-milled cross-section of TS Mn/Cu-coated sample without exposure. b) BIB-milled cross-section of the TS Mn/Cu-coated sample exposed at 650°C in humid air for 24 h. c) BIB-milled cross-section of the TS Mn/Cu-coated sample exposed at 650°C in humid air for 1,000 h with the corresponding EDS analysis.

Area-specific Resistance Measurements

Figure 39 shows the ASR measurements performed on coated samples exposed for 1,000 h at 650°C in air + 3 % water vapour.

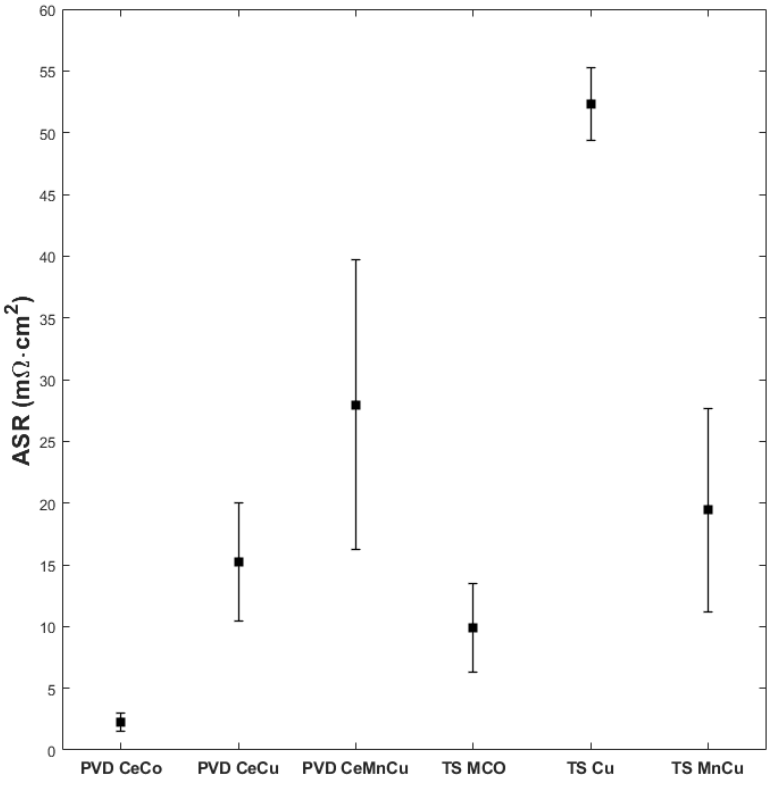

Figure 39: ASR measurements in air for samples exposed at 650°C for 1,000 h in air + 3% H_2O. Error bars indicate standard deviation.

The PVD Ce/Co-coated samples exhibited an ASR of about 3 mΩ·cm^2 after 1,000 h of exposure at 650°C. Previous research conducted on Sanergy HT Ce/Co-coated samples [33] showed that Ce/Co-coated samples displayed ASR values of around 8 mΩ·cm^2 after 500 h of exposure at 650°C in air + 3% water vapour. This difference is considered to be marginal. PVD Ce/Cu-coated samples showed an ASR of about 15 mΩ·cm^2 after the 1,000 h of exposure, while the Ce/MnCu coating exhibited an ASR of about 28 mΩ·cm^2. Those results are in line with those of the microstructural analysis. The PVD Ce/Cu-coated samples formed a very thin Cr_2O_3 layer (of roughly 200 nm), while the Ce/MnCu-coated samples formed large oxide nodules with a slightly thicker chromia scale (approximately 300 nm) underneath. As reported previously [38], the ASR mainly reflects the thickness of the Cr_2O_3 layer. For the PVD Ce/Cu coating, the presence of an intermediate spinel layer does not seem to affect significantly the

conductivity of the interconnect. Earlier studies [24] have shown that manganite spinels, such as $MnCo_2O_4$ (60 $S \cdot cm^{-1}$ at 800°C) or $Cu_{1.3}Mn_{1.7}O_4$ (225 $S \cdot cm^{-1}$ at 750°C) are the most conductive spinels, and a CuO oxide layer is known to be conductive at high temperature (2×10^3 $S \cdot cm^{-1}$ at 700°C ; 10^5 $S \cdot cm^{-1}$ at 1,000°C) [39-41]. Thus, these oxides are three orders of magnitude more conductive than chromia, which have conductivities in the range of 0.001–0.05 $S \cdot cm^{-1}$, and thus do not significantly contribute to the overall resistance [42-44]. PVD Ce/MnCu-coated samples exhibit somewhat higher ASR values, as a significant part of the surface (>50%) is covered with Fe-rich nodules.

The TS Mn/Co coating exhibited a low ASR value, comparable to that of the PVD Ce/Cu coating. This accords with the observation of a thin Cr_2O_3 layer underneath the coating. In contrast, the TS Cu coating had the highest ASR value, which could be related to a somewhat thicker Cr_2O_3 layer or the thick Fe-rich intermediate oxide scale. The TS Mn/Cu coating exhibited an ASR of 19 $m\Omega \cdot cm^2$ on average, despite the formation of a rather thick oxide layer.

Overall, the PVD Ce/Co coating exhibits a lower ASR than the TS Mn/Co coating. However, since both samples exhibit very low ASR values, it is not clear whether this difference is significant.

Summary

The present study has focused on Cu-based coatings on AISI 441 steel. The coatings were manufactured using two different deposition methods: PVD and TS. The PVD coatings were deposited as a metallic coating and oxidised during the first stage of the exposure. The TS coatings consisted of a mostly oxidised coating sprayed on top of the substrate. In this study, uncoated, PVD Ce/Cu-, PVD Ce/MnCu-, PVD Ce/Co (as a reference for PVD coatings), TS Cu-, TS Mn/Cu- and TS Mn/Co- (as reference for TS coatings) coated samples were analysed.

Uncoated samples have the highest level of Cr(VI) evaporation. The observed difference between the PVD and TS coatings can be attributed to the uncoated edges of the PVD-coated samples. It is concluded that all the coated samples have essentially identical Cr evaporation rates, despite their different thicknesses. The PVD Ce/Co- and Ce/Cu-coated samples, as well as the TS Mn/Co-coated sample, have ASR values <15 $m\Omega \cdot cm^2$. The PVD Ce/MnCu-coated samples display a somewhat higher ASR after 1,000 h of exposure. This is attributed to the nodules on top of the scale. The TS Mn/Cu-coated sample has a similar ASR to the PVD Ce/MnCu-coated sample, while TS Cu coating gives the highest ASR values.

PVD Ce/Cu coating is a good candidate to replace the state-of-the-art PVD Ce/Co coating. It offers a low level of Cr(VI) evaporation and thin, adherent, and conductive oxide scales. At intermediate temperatures, PVD Ce/Cu-coated samples form a conductive CuO top layer, a conductive $(Cu,Cr,Mn,Fe)_3O_4$ intermediate spinel, and a very thin (1 μm) Cr_2O_3 layer at the metal/oxide interface. The formation of oxide nodules does not seem to influence the overall conductivity or the corrosion properties of the coated steel.

Acknowledgments

This work was conducted at the Swedish High Temperature Corrosion Centre (HTC) at Chalmers University of Technology. This work was performed in part at the Chalmers Material Analysis Laboratory, CMAL. The authors are grateful for funding by the Swedish Energy Agency through grant 2015-009652 and the Fordonsstrategisk forskning och innovation (FFI) program.

References

1. Beretta, G.P., *World energy consumption and resources: an outlook for the rest of the century.* International journal of environmental technology and management, 2007. **7**(1-2): p. 99-112.
2. Carrette, L., K.A. Friedrich, and U.J.C. Stimming, *Fuel cells: principles, types, fuels, and applications.* 2000. **1**(4): p. 162-193.
3. Bvumbe, T.J., et al., *Review on management, mechanisms and modelling of thermal processes in PEMFC.* Hydrogen and Fuel Cells, 2016. **1**(1): p. 1-20.
4. Powell, M., et al., *Demonstration of a highly efficient solid oxide fuel cell power system using adiabatic steam reforming and anode gas recirculation.* Journal of Power Sources, 2012. **205**: p. 377-384.
5. Brandon, N., *Solid oxide fuel cell lifetime and reliability: critical challenges in fuel cells*. 2017: Academic Press.
6. Staffell, I., A. Ingram, and K. Kendall, *Energy and carbon payback times for solid oxide fuel cell based domestic CHP.* International Journal of Hydrogen Energy, 2012. **37**(3): p. 2509-2523.
7. Stambouli, A.B. and E. Traversa, *Solid oxide fuel cells (SOFCs): a review of an environmentally clean and efficient source of energy.* Renewable and sustainable energy reviews, 2002. **6**(5): p. 433-455.
8. Mah, J.C., et al., *Metallic interconnects for solid oxide fuel cell: a review on protective coating and deposition techniques.* 2017. **42**(14): p. 9219-9229.
9. Jeffrey W. Fergus, R.H., Xianguo Li, David P. Wilkinson, Jiujun Zhang, *Solid Oxide Fuel Cells: Materials Properties and Performance*. 2009: Taylor & Francis Group LLC.
10. Mahato, N., et al., *Progress in material selection for solid oxide fuel cell technology: A review.* Progress in Materials Science, 2015. **72**: p. 141-337.
11. Hilpert, K., et al., *Chromium vapor species over solid oxide fuel cell interconnect materials and their potential for degradation processes.* 1996. **143**(11): p. 3642-3647.
12. Stanislowski, M., et al., *Chromium vaporization from high-temperature alloys I. Chromia-forming steels and the influence of outer oxide layers.* 2007. **154**(4): p. A295-A306.
13. Molin, S., et al., *Low temperature processed MnCo2O4 and MnCo1. 8Fe0. 2O4 as effective protective coatings for solid oxide fuel cell interconnects at 750 C.* Journal of Power Sources, 2016. **336**: p. 408-418.
14. Zanchi, E., et al., *Electrophoretic co-deposition of Mn1. 5Co1. 5O4, Fe2O3 and CuO: Unravelling the effect of simultaneous addition of Cu and Fe on the microstructural, thermo-mechanical and corrosion properties of in-situ modified spinel coatings for solid oxide cell interconnects.* Journal of the European Ceramic Society, 2022. **42**(7): p. 3271-3281.
15. Puranen, J., et al., *Characterization of high-velocity solution precursor flame-sprayed manganese cobalt oxide spinel coatings for metallic SOFC interconnectors.* Journal of thermal spray technology, 2013. **22**(5): p. 622-630.
16. Shaigan, N., et al., *A review of recent progress in coatings, surface modifications and alloy developments for solid oxide fuel cell ferritic stainless steel interconnects.* Journal of Power Sources, 2010. **195**(6): p. 1529-1542.
17. Kurokawa, H., et al., *Chromium vaporization of bare and of coated iron–chromium alloys at 1073 K.* Solid State Ionics, 2007. **178**(3-4): p. 287-296.
18. Trebbels, R., T. Markus, and L. Singheiser, *Investigation of chromium vaporization from interconnector steels with spinel coatings.* Journal of Fuel Cell Science and Technology, 2010. **7**(1).
19. H. Holmberg, M.W.L., J. Westlinder, *Recent Development in Pre-coating of Stainless Steel Strips for Interconnects at Sandvik Materials Technology*, in *10th European SOFC Forum*. 2012.
20. Grolig, J.G., et al., *Copper Based Conversion Coatings on Ferritic Stainless Strip Steel as Solid Oxide Fuel Cell Interconnects: Oxidation Performance and Chromium Evaporation.* ECS Transactions, 2013. **57**(1): p. 2339-2347.

21. Waluyo, N.S., et al., *Protective coating based on manganese–copper oxide for solid oxide fuel cell interconnects: plasma spray coating and performance evaluation.* Ceramics International, 2018. **44**(10): p. 11576-11581.
22. Tomas, M., et al., *Cu-Based Coatings for IT-SOFC Applications.* ECS Transactions, 2019. **91**(1): p. 2291.
23. Lv, Y., S. Geng, and Z. Shi, *Evaluation of electroplated copper coating on ferritic stainless steel for solid oxide fuel cells interconnects.* Journal of Alloys and Compounds, 2017. **726**: p. 269-275.
24. Petric, A. and H. Ling, *Electrical conductivity and thermal expansion of spinels at elevated temperatures.* Journal of the American Ceramic Society, 2007. **90**(5): p. 1515-1520.
25. Directorate-General for Internal Market, I., Entrepreneurship and SMEs and E. Commission. *https://ec.europa.eu/growth/sectors/raw-materials/areas-specific-interest/critical-raw-materials_en*. 2020.
26. Prause, L., *Conflicts related to resources: The case of cobalt mining in the Democratic Republic of Congo*, in *The Material Basis of Energy Transitions*. 2020, Elsevier. p. 153-167.
27. Farjana, S.H., N. Huda, and M.P. Mahmud, *Life cycle assessment of cobalt extraction process.* Journal of Sustainable Mining, 2019. **18**(3): p. 150-161.
28. Lundberg, M.W., et al., *Novel multilayered PVD-coating in a roll to roll mass production process.* ECS Transactions, 2013. **57**(1): p. 2203.
29. Pawlowski, L., *The science and engineering of thermal spray coatings*. 2008: John Wiley & Sons.
30. Sidhu, T., S. Prakash, and R. Agrawal, *State of the art of HVOF coating investigations-A review.* Marine Technology Society Journal, 2005. **39**(2).
31. Froitzheim, J., et al., *Investigation of chromium volatilization from FeCr interconnects by a denuder technique.* Journal of The Electrochemical Society, 2010. **157**(9): p. B1295-B1300.
32. Tedmon Jr, C., *The effect of oxide volatilization on the oxidation kinetics of Cr and Fe-Cr alloys.* Journal of the Electrochemical Society, 1966. **113**(8): p. 766.
33. Falk-Windisch, H., et al., *Co-and Ce/Co-coated ferritic stainless steel as interconnect material for Intermediate Temperature Solid Oxide Fuel Cells.* Journal of Power Sources, 2017. **343**: p. 1-10.
34. Falk-Windisch, H., J.E. Svensson, and J. Froitzheim, *The effect of temperature on chromium vaporization and oxide scale growth on interconnect steels for Solid Oxide Fuel Cells.* Journal of Power Sources, 2015. **287**: p. 25-35.
35. Reddy, M.J., J.-E. Svensson, and J. Froitzheim, *Reevaluating the Cr Evaporation Characteristics of Ce/Co Coatings for Interconnect Applications.* ECS Transactions, 2021. **103**(1): p. 1899.
36. Talic, B., et al., *Effect of coating density on oxidation resistance and Cr vaporization from solid oxide fuel cell interconnects.* Journal of Power Sources, 2017. **354**: p. 57-67.
37. Talic, B., et al., *Diffusion couple study of the interaction between Cr2O3 and MnCo2O4 doped with Fe and Cu.* Solid State Ionics, 2019. **332**: p. 16-24.
38. Goebel, C., et al., *Does the conductivity of interconnect coatings matter for solid oxide fuel cell applications?* Journal of Power Sources, 2018. **383**: p. 110-114.
39. Meyer, B., et al., *Binary copper oxide semiconductors: From materials towards devices.* physica status solidi (b), 2012. **249**(8): p. 1487-1509.
40. Zoolfakar, A.S., et al., *Nanostructured copper oxide semiconductors: a perspective on materials, synthesis methods and applications.* journal of materials chemistry c, 2014. **2**(27): p. 5247-5270.
41. Samsonov, G.V., *The oxide handbook*. 2013: Springer Science & Business Media.
42. Huczkowski, P., et al., *Growth mechanisms and electrical conductivity of oxide scales on ferritic steels proposed as interconnect materials for SOFC's.* Fuel Cells, 2006. **6**(2): p. 93-99.
43. Crawford, J.A. and R.W. Vest, *Electrical conductivity of single-crystal Cr2O3.* Journal of Applied Physics, 1964. **35**(8): p. 2413-2418.
44. Holt, A. and P. Kofstad, *Electrical conductivity and defect structure of Cr2O3. I. High temperatures (> ~ 1000° C).* Solid State Ionics, 1994. **69**(2): p. 127-136.

Publication 2

Novel coatings for protecting solid oxide fuel cell interconnects against the dual-atmosphere effect

M. Tomas, A. Visibile, J-E. Svensson and J. Froitzheim

Energy and Materials, Chalmers University of Technology
Kemivägen 10, 41296 Gothenburg, Sweden

Abstract

A key component of a Solid Oxide Fuel Cell (SOFC) is the interconnect, which connects individual fuel cells in series to form a fuel cell stack to reach a desired electrical potential. The interconnect is exposed to air and fuel in parallel, these so-called dual-atmosphere conditions give rise to especially severe corrosion on the air-side. This work investigates coatings to mitigate this effect. Physical Vapour Deposition (PVD) CeCo-coated AISI 441 samples on the air-side and PVD metallic Al- and Al_2O_3-coated AISI 441 samples on the fuel-side were exposed under dual-atmosphere conditions for up to 7,000 h. The evolution of the corrosion products was followed every 1,000 h with an optical microscope. Scanning electron microscopy and energy-dispersive x-ray spectroscopy were performed on cross-sections of the samples after 3,000 h of exposure. The SEM analysis showed that coating on the air-side improved the sample's life-time by reducing the level of Cr evaporation even in a dual-atmosphere. The use of fuel-side coatings suppressed the dual-atmosphere effect since the coatings formed a barrier to hydrogen permeation. The best results were observed with metallic Al and Al_2O_3 coating on the fuel-side, which drastically reduced the dual-atmosphere effect. However, the poor conductivity of Al_2O_3 makes its use as a coating challenging.

KEYWORDS: Solid Oxide Fuel Cell, SOFC, interconnect, dual-atmosphere, coating, ASR, Alumina

Introduction

In the last few decades, Solid Oxide Fuel Cells (SOFCs) have attracted interest due to their high electrical efficiency levels (>60%), low emissions, and high fuel flexibility [1, 2]. SOFCs are considered a promising technology to address the demand for more sustainable energy, as they are valid systems to convert hydrogen or hydrocarbons from renewable sources to electrical energy. However, high production costs and limited life-times have made commercialisation difficult. A key component of an SOFC is the interconnect (IC), which connects the individual fuel cells in series to form a fuel cell stack, so as to reach the desired electrical potential. As fuel cell operating temperatures decreased, a switch from ceramic interconnects to Ferritic Stainless Steel (FSS) interconnects became feasible. The most important parameters to consider in relation to interconnects are: material stability in relation to high-temperature oxidation; and electrical resistance of the formed oxide. When oxidised, manganese (Mn)-containing ferritic stainless steels have been shown to form a $(Cr, Mn)_3O_4$ spinel top layer on top of the semi-conductive chromia scale in the temperature range of the SOFC [3]. The use of low-cost, commercially available stainless steels, such as AISI 441, instead of tailor-made alloys may provide substantial cost savings but may also lead to faster degradation of the interconnect. Two well-known degradation processes are active when an FSS interconnect is exposed at high temperature: (a) Cr(VI) evaporation from the steel, which poisons the cathode [4]; and (b) growth of a Cr_2O_3 layer, which reduces the electrical conductivity [5, 6]. In the past decade, several coatings have been studied and proposed [6-13] as a way to mitigate these two phenomena. To reduce Cr(VI) evaporation, the most-heavily commercialised examples are the Mn- and cobalt (Co)-based spinel coatings (MCO coatings), which are considered the state-of-the-art for this purpose. An alternative strategy to obtain MCO coatings is to coat the substrate with metallic Co. This Co layer will oxidise to form Co_3O_4 and becomes enriched in Mn through diffusion from the steel substrate during stack operation [7, 8]. MCO coatings are highly effective, reducing Cr(VI) evaporation by a factor of more than 10 compared to uncoated samples [9]. Reactive Elements (REs) have been described by *Hou et al.* [10] as exerting beneficial effects on Cr_2O_3-forming alloys through: selective oxidation of chromium; reducing the Cr_2O_3 scale growth rate; or changing the transport mechanism from outward metal transport to inward oxygen diffusion. A clear difference in chromia thickness has been observed for samples coated with a thin layer of ceria, compared to samples without an RE layer [9, 11-13].

The so-called ‘dual-atmosphere effect’ is another typical degradation process for SOFCs,

especially when operated at intermediate temperatures [14, 15]. Chromia former stainless steels like AISI 441 or Crofer 22 APU, exposed at high temperature in single air or humid hydrogen gas, form a protective scale of Cr_2O_3 with a cap of $(Mn, Cr)_3O_4$ spinel above (if the alloy contains Mn) [16]. In a single condition, the diffusion of Cr toward the surface is faster than its consumption (scale growth and Cr evaporation) so the formation of the scale is ensured. Once a sample is exposed on one side to air, and on the other side to hydrogen (dual-atmosphere conditions), the outcome largely changes. *Yang et al*. [17, 18] noticed that an alloy exposed to a dual environment behaves differently from one exposed to a single atmosphere. Although it has been addressed that diffused hydrogen from the fuel-side affects the air-side oxidation, the mechanism behind the protective oxide scale breakdown is not fully clear. Moreover, the severity of the dual-atmosphere effect varies widely among studies [19-22]. At high temperatures (800°C - 850°C), several authors [17, 18, 23, 24] noticed an iron enrichment of the protective scale on the air-side. At lower temperatures (600°C -700 °C) the air-facing side of the sample undergoes severe corrosion with the formation of hematite nodules and later formation of a thick hematite scale [15, 25, 26]. Iron oxides are not protective, thus, the scale grows several orders of magnitude faster than chromium oxide leading to faster material degradation and loss of performance. This effect was found on various alloys [27] like AISI 441[14, 19, 28], AISI 430 [29, 30], Sanergy HT [31], and Crofer APU 22 [32], to cite the most used ones in terms of interconnect applications. Other authors [33] have stated the beneficial effect of a higher Cr concentration in the alloy may help reduce the dual-atmosphere effect by slowing down the hydrogen diffusion [18, 26]. Several explanations have been proposed to explain this phenomenon. *Rufner et al.* [21] suggested that the pO_2 on the air-side could be locally modified by the permeated hydrogen. *Yang et al.* [18] instead pointed out that it may be due to an increased number of cation vacancies close to the air-side, which leads to hydroxide species formation that enhances scale growth rate. Other authors [34, 35] proposed theories in which the lattice is distorted because of hydrogen presence. Recently *Gunduz et al.* [15] showed how the hydrogen diffusion into the alloy might affect the Cr diffusion, thus promoting non-protective Fe-oxide formation.

However, in those studies, the samples were not coated. Previous research [36] has demonstrated the effect of Ce/Co-coated samples exposed to a dual-atmosphere at 850°C. It has been established that Ce/Co coating helps to mitigate the dual-atmosphere effect at higher operating temperatures. However, samples exposed at 600°C suffer severe corrosion after a short period of time. This is in accordance with previous research that described the reverse temperature effect [19]. To the best of our knowledge, no previous studies were performed

with hydrogen-barrier coatings on the fuel-side. The main indication for the efficiency of fuel-side coatings comes from *Goebel et al.* [28], who examined the effect of pre-oxidation time and showed how this is particularly important at the fuel-side to reduce hydrogen diffusion into the material and to mitigate the dual-atmosphere effect.

In the present work, barrier coatings developed to reduce the dual-atmosphere corrosion for Intermediate-Temperature Solid Oxide Fuel Cells (IT-SOFCs) are presented for the first time (*Patent EP3256617B1*). The state-of-the-art Ce/Co coating on the air-side is exposed in combination with novel coatings on the fuel-side: metallic Al and Al_2O_3 deposited via Physical Vapour Deposition (PVD). Coating the fuel-side is expected to reduce the ingress of hydrogen into the alloy and to reduce the dual-atmosphere effect on the air-side. Uncoated samples that are pre-oxidised for 5 h at 800°C are exposed as a reference. All the coatings are exposed under simulated SOFC working conditions for 3,000 h.

Materials and methods

- Dual-atmosphere set-up

To simulate dual-atmosphere conditions, steel samples were simultaneously exposed in air +3% H_2O on one side and Ar – 5% H_2 – 3% H_2O on the other side, at 600°C. All the experiments were conducted in a dual-atmosphere using the experimental set-up described by *Alnegren et al.* [14]. The sample holder construction is based on a model provided by Montana State University, and further information on this set-up can be found elsewhere [21]. Gold rings were used to seal the circular samples to the set-up, to ensure gas-tightness.

- Sample characteristics and preparation

The compositions and characteristics of the materials used in this study are described in TABLE V and TABLE VI.

TABLE V. Compositions of the studied alloys (in wt%), as specified by the manufacturer.

Materials	Fe	Cr	C	Mn	Si	Ni	Ti	Nb	Al	N	P	S
AISI 441 Batch: 89893	Bal.	17.53	0.016	0.40	0.59	0.15	0.172	0.41	0.007	0.015	0.024	<0.001

Samples were coated by Sandvik Materials Technology AB using a proprietary PVD process. Coin-shaped samples (Ø 21 mm) were stamped out of a metal sheet using a hydraulic press. The experimental matrix and exposure characteristics are listed in TABLE VI. A cleaning procedure that consisted of washing for 20 minutes in acetone and 20 minutes in ethanol was performed before any thermal treatment. All the samples were then pre-oxidised at 800°C ± 5°C for 5 h in air + 3% H_2O with a ramp rate of 1°C·min^{-1}, under a flow of 280 mL·min^{-1}.

TABLE VI. Experimental matrix of the materials used and their exposure times.

Materials	Coating		Exposure time (h)
	Fuel-side	Air-side	
AISI 441	Al_2O_3 (~500 nm)	Uncoated	3,000
AISI 441	Al (~1,000 nm)	Uncoated	3,000
AISI 441	Al (~1,000 nm)	10 nm Ce / 600 nm Co	7,000
AISI 441	Uncoated	10 nm Ce / 600 nm Co	3,000
AISI 441	Uncoated	Uncoated	3,000

Al coating is protected by the patent number: *EP3256617B1*.

- Exposures

All samples were exposed to a humid dual-atmosphere. The following gases were used: Ar - 5% H_2 - 3% H_2O with a flow rate of 120 smL·min^{-1} on the fuel-side; and air + 3% H_2O with a flow rate of 8,800 smL·min^{-1}on the air-side. This resulted in an airflow speed of around 27 cm·s^{-1} inside the quartz tube; therefore, kinetically controlled, flow-independent chromium evaporation rates were achieved [37]. To adjust the humidity level to 3%, all gases were bubbled through water baths with temperature-controlled reflux condensers set to 24.4°C. All exposures were conducted at a temperature of 600°C ± 5°C. A ramp of 1°C·min^{-1} was used to heat up and cool down the samples, to minimise oxide spallation. The exposure was interrupted after 500 h, 1,000 h, 2,000 h, and 3,000 h, to document the evolution of the oxide scale. Selected samples were exposed for up to 7,000 h to assess life-time. All the experiments involving exposure for 3,000 h were repeated to ensure data reproducibility.

- Microscopy

Photographs of the samples were taken at different exposure times using a Nikon SMZ800 camera equipped with a ring light. For the cross-section analyses, the samples were cut with an oil-free, low-speed saw (Struers Minitom). Cross-sections of all the samples were then prepared using a Leica EM TIC 3X Broad Ion Beam (BIB) with an acceleration voltage of 8 kV and a current of 3 mA. The resulting cross-sections were analysed using the JEOL 7800F Prime SEM. Imaging was performed with an acceleration voltage of 10 kV, and Energy-Dispersive x-ray (EDX) analysis was performed with an acceleration voltage of 15 kV.

- Area-Specific Resistance (ASR) Measurement

The ASR measurement was used to determine the electrical resistance of the oxide. The ASR is the measured resistance (R) multiplied by the contact area (A). A sputter mask with dimensions of 10×10 mm^2 was placed on the dual-atmosphere-exposed sample, and the sample was then coated with platinum for 10 minutes using the Quorum 150 sputter coater and a sputtering current of 60 mA. This procedure was repeated for the reverse side of the sample. The sputtering step was used to produce electrodes with a defined area and to ensure good contact between the sample and the platinum electrodes. The exposed samples were then mounted in a ProboStat™ (NorECs, Norway) measurement set-up using a 1 cm^2 Pt wire and grid to contact the sample electrodes. The resistance was measured by the 2-point, 4-wire method at 600°C in air. The ASR was monitored in Ar – 5% H_2 during the cooling of the sample, to check for semi-conductive behaviour. One side of the sample was ground to measure the resistance of the coating alone.

Results & Discussion

1. Visualisation of the dual-atmosphere effect throughout the exposure

Figure 40 shows the evolution of all the samples exposed for up to 3,000 h to the dual-atmosphere conditions. During the first 500 h, there are no apparent signs of severe corrosion. The protective behaviour is attributed to the long duration of pre-oxidation treatment (5 h at 800°C), in line with the earlier works of *Goebel et al.* [28] and *Reisert et al.* [38], which showed a direct relationship between the length of the pre-oxidation step and the onset of breakaway corrosion. Nevertheless, after 1,000 h of exposure, the uncoated and Ce/Co-coated samples show signs of breakaway corrosion, while the other samples remain protective. The Ce/Co-coated sample appears to be slightly more protective than the uncoated sample. However, once the sample experiences 2,000 h of exposure, the Ce/Co-coated sample exhibits corrosion comparable to that of the uncoated sample. The samples with fuel-side coatings still show no visible sign of breakaway corrosion at this point. After 3,000 h of exposure, the uncoated and Ce/Co-coated samples display similar levels of corrosion, while the samples coated on the fuel-side do not show visible signs of breakaway oxidation and seem to behave in a similar manner. Nevertheless, as will be discussed below, their conditions are highly different.

The efficiency of the Ce/Co coating in terms of delaying corrosion has been demonstrated previously in a single atmosphere [9, 11, 12]. On the other hand, coatings of the fuel-side are expected to act as a barrier to the ingress of hydrogen in a manner similar to that shown for pre-oxidation [39, 40].

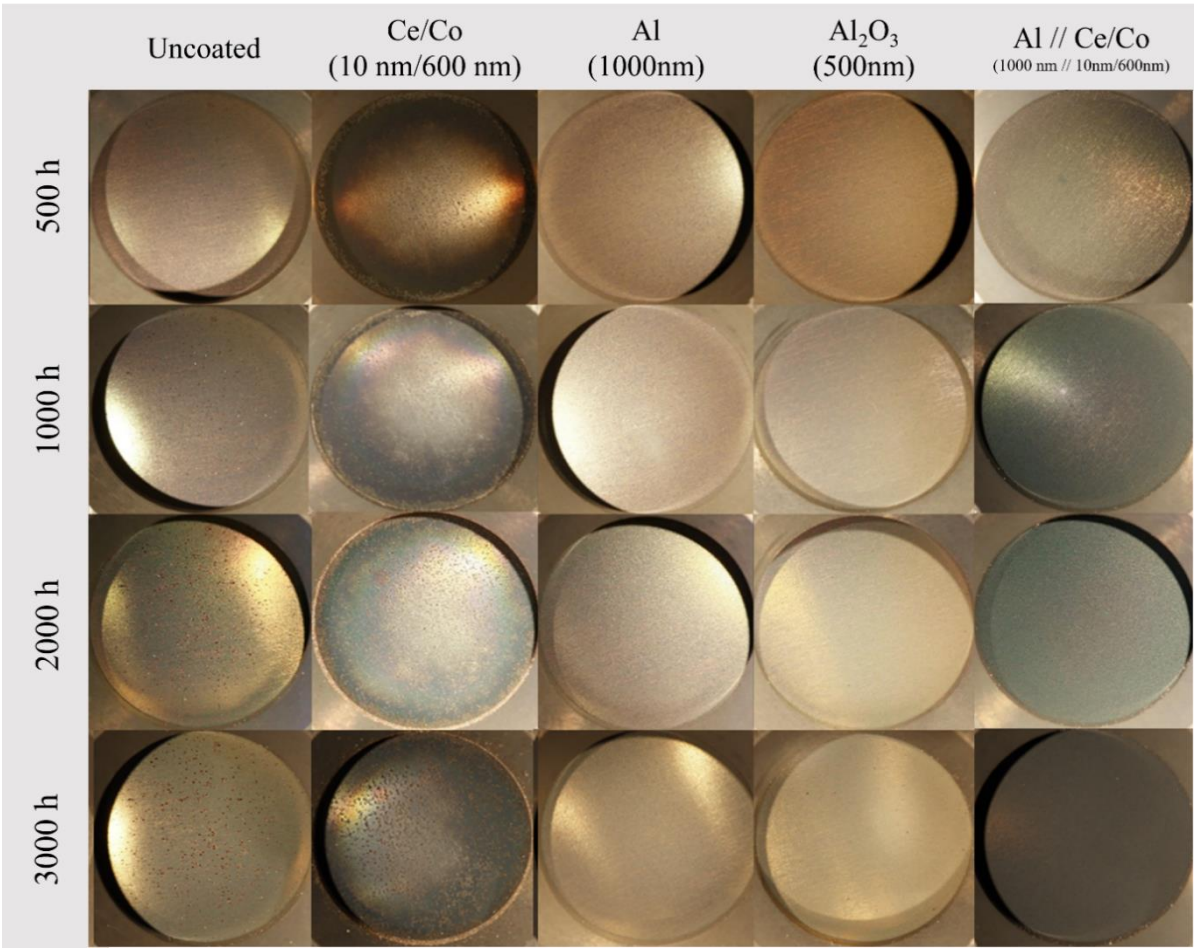

Figure 40: Photographs of the air-facing sides of AISI 441 coupons taken during exposure to a discontinuous dual-atmosphere (Ar-5% H_2 + 3% H_2O // Air + 3% H_2O) at 600°C.

2. Microstructural analysis

Uncoated sample exposed for 3,000 h

Figure 41 shows the SEM micrographs of the uncoated sample. The top-view of the air-side (see Figure 41a) and the fuel-side (see Figure 41b) after pre-oxidation, depict a homogeneous oxide scale covering the sample. No visible signs of breakaway oxidation can be observed on any of the samples after any of the exposures.

After 3,000 h of exposure, the air-side of the uncoated sample exhibits a surface that is partially covered with hematite nodules (see Figure 41c) that are roughly 300 μm in width. On top of these nodules, whiskers can be observed. Previous studies [21, 29] have also documented the presence of hematite nodules on 430 and 441 steel samples exposed to similar dual-atmosphere conditions. A protective oxide is observed between the nodules. The cross-section of the air-side (Figure 41d) confirms the observations made from Figure 41c, showing a nodule of Fe_2O_3 and a thin (< 1 μm) protective oxide scale comprised of $(Cr, Mn)_3O_4$ spinel and chromia. According to previous research [14, 41], this layer is mainly composed of $(Cr, Mn)_3O_4$ spinel and chromia. The thickness of the breakaway corrosion product is about 25 μm as a result of the poor protective behaviour of the iron-rich oxide. Beneath the Fe_2O_3 nodule, a $(Fe, Cr)_3O_4$ spinel layer is present, and an internal oxidation zone (IOZ). This degradation morphology has been reported in previous studies [14, 15]. The top-view micrograph of the fuel-side (see Figure 41e) depicts an oxide scale covering the sample's surface, together with the presence of extremely small nodules (~2 μm) following the rolling direction. This morphology is very similar to that observed after pre-oxidation (see Figure 41b). The cross-section of the fuel-side (Figure 41f) exhibits a protective, thin, dense, and homogeneous oxide scale, which has been identified as containing a $(Cr, Mn)_3O_4$ spinel and chromia.

Those observations accord with those made in previous studies [14, 28] showing that uncoated AISI 441 ferritic stainless steel suffers severe corrosion after 1,000 h of exposure at 600°C to the dual-atmosphere, even when it is pre-oxidised for 280 min. Fe-rich nodules are identified on the surface of the air-facing side of the sample. The pre-oxidation step aims to simulate the conditioning of the stack before operation. Furthermore, it is expected to provide a protective Cr_2O_3 layer that acts as a diffusion barrier to both oxidation of the alloy and the transport of hydrogen from the fuel-side to the air-side [18, 28]. *Kurokawa et al.* [42] exposed Fe-16Cr steel at 800°C and showed that after a continuous chromia layer has formed, the permeation of hydrogen was drastically reduced by four orders of magnitude.

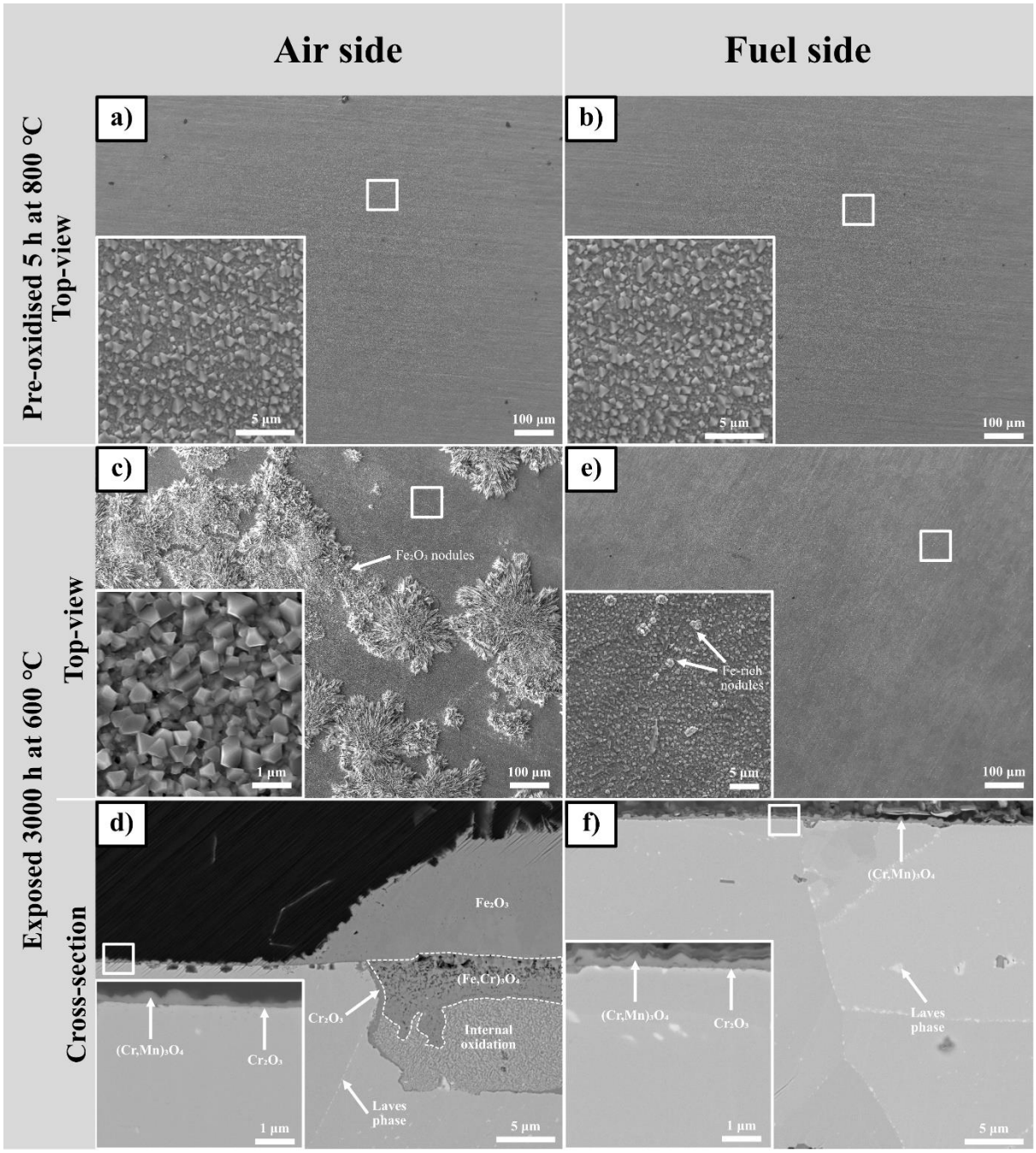

Figure 41: SEM micrographs representing: a) top-view of the air-side of the pre-oxidised sample; b) top-view of the fuel-side of the pre-oxidised sample; c) top-view of the air-side; d) cross-section of the air-side; e) top-view of the fuel-side; and f) cross-section of the fuel-side of 441 uncoated samples pre-oxidised for 5 h exposed to the dual-atmosphere (Ar-5% H_2 + 3% H_2O // Air + 3% H_2O) for 3,000 h at 600°C. Inset: higher-magnification image of selected scale regions.

10 nm Ce / 600 nm Co-coated sample exposed for 3,000 h

Figure 42 depicts SEM micrographs of the Ce/Co-coated sample. The plan-view of the air-side after pre-oxidation (see Figure 42a) shows a fully protective Co spinel covering the surface of the sample. No signs of breakaway corrosion are observed. The top-view of the fuel-side (uncoated) after the pre-oxidation treatment (see Figure 42b) exhibits an oxide scale that covers the entire surface of the sample, with no visible signs of breakaway corrosion.

After 3000h of exposure, the air-side of the sample exhibits some iron-rich nodules that are roughly 150 μm in width with whiskers on top, while the largest part of the surface is covered by a thin protective oxide scale (see Figure 42c), similar to that observed after pre-oxidation. There are no signs of spallation of the oxide scale on the sample, indicating good adherence of the oxidised coating. The cross-section of the air-side of the sample is shown in Figure 42d, and two different microstructures are evident: the nodules and the protective scale. The nodule consists of three distinct layers. The top layer comprises an $(Fe, Co)_3O_4$ spinel. EDS analysis shows that the top layer contains Fe (~20 at%), Co (~10 at%), and a low percentage of Cr (~5 at%). In this case, it appears that Fe diffused within the oxide scale even with the presence of a ceria layer. Underneath this layer, an Fe-rich oxide with thickness of about 20 μm is found. Below the original sample surface, there is an $(Fe, Cr)_3O_4$ spinel with thickness similar to that of the Fe-rich oxide phase observed previously. The overall thickness of the nodules is approximately 40 μm. The nodules are fewer but more localised and thicker than those observed in uncoated samples. The protective oxide scale comprises a very thin (~100 nm) $(Co,Cr)_3O_4$ spinel on top, which contains 10 at% of Co and 10 at% of Cr, followed by 1-μm-thick Co_3O_4 spinel with a thin (~200 nm) Cr_2O_3 layer. The presence of Cr in the top layer is attributed to Cr evaporation from the sample holder. *Skilbred et al.* [36] observed similar cubic-shaped grains on the top layer of Ce/Co-coated samples exposed to dual-atmosphere conditions at 850°C,. Furthermore, in their study, the cross-section depicts a thin Co_3O_4 layer followed by a thin Cr_2O_3 oxide scale. However, there are no signs of Fe-rich nodules. This is mainly attributed to the less-severe dual-atmosphere at high temperatures, as well as the short exposure time (150 h), which did not allow sufficient time for the breakaway [15]. Figure 41e depicts the top-view of the fuel-side of the sample exposed to H_2 + 3% H_2O, where some small nodules (~2 μm) are present. The surface state is identical to that observed right after the pre-oxidation step (see Figure 42b) and similar to that of the uncoated sample (Figure 41f). From the top-view analysis, these nodules appear to have grown underneath the top layer and do not seem to promote the breakdown of the oxide scale. Figure 42f represents the cross-section of the fuel-

side. The image shows a very thin (~100 nm), dense, and homogeneous $(Cr, Mn)_3O_4$ spinel and chromia layer. A similar morphology was observed by *Niewolak et al.* [3].

The superior resistance to the dual-atmosphere effect of the Ce/Co-coated sample, as compared to the uncoated sample, is in line with previous findings [11, 12, 43, 44] for samples exposed to a single atmosphere. It has been shown that regardless of whether the top layer is Co_3O_4, $(Co, Mn)_3O_4$ or $(Co, Mn, Fe)_3O_4$, the Cr evaporation rate at 650°C is significantly lower for Ce/Co-coated materials than for uncoated FeCr steel. Thus, the depletion of Cr from Ce/Co-coated materials over time is less extensive than from uncoated samples, which is expected to result in less-severe breakaway oxidation.

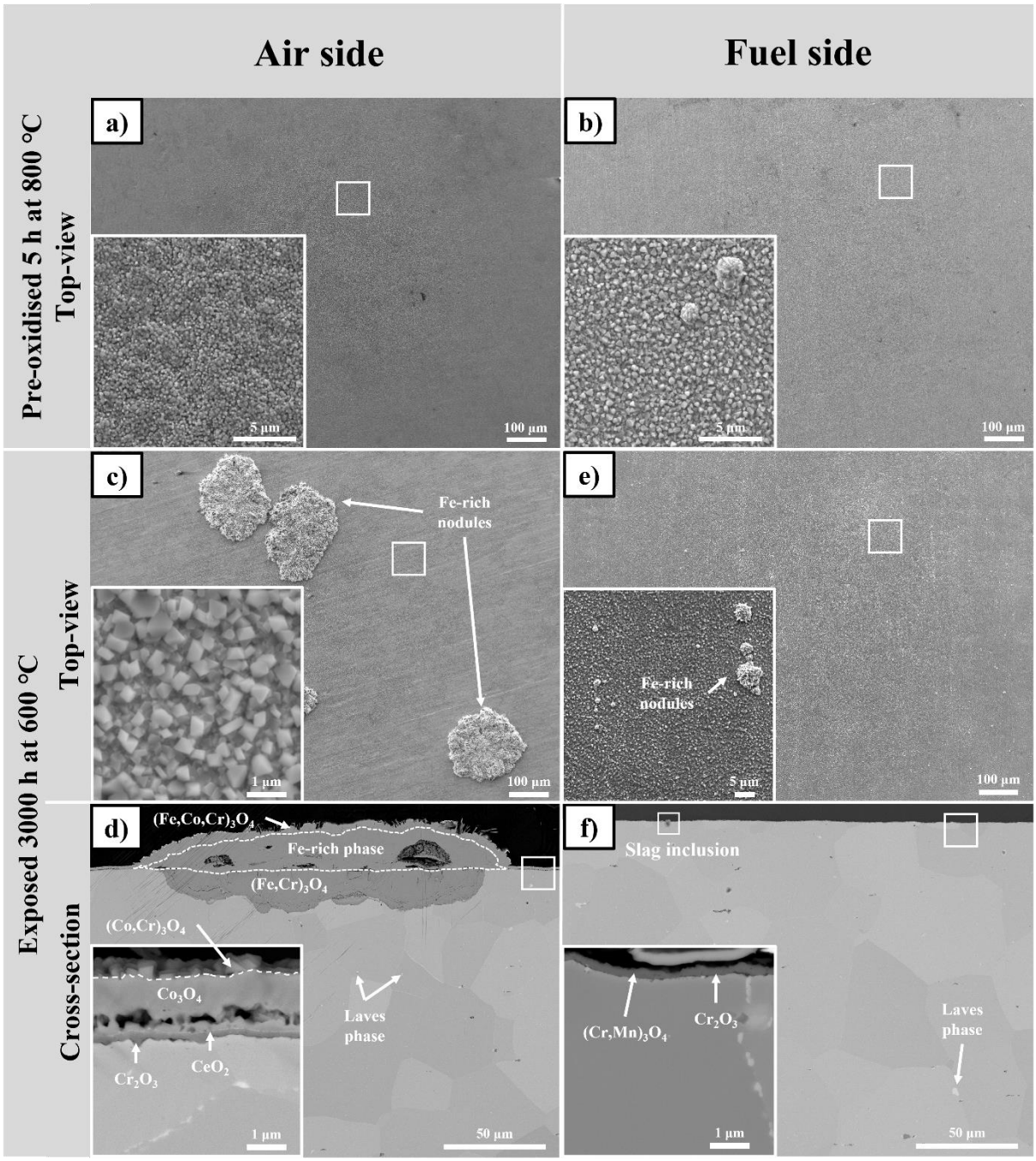

Figure 42: SEM micrographs representing: a) top-view of the air-side of the pre-oxidised sample; b) top-view of the fuel-side of the pre-oxidised sample; c) top-view of the air-side; d) cross-section of the air-side; e) top-view of the fuel-side; and f) cross-section of the fuel-side of the 10 nm Ce / 600 nm Co-coated 441 sample exposed to the dual-atmosphere (Ar-5% H_2 + 3% H_2O // Air + 3% H_2O) for 3,000 h at 600°C. Inset: higher magnification of selected scale regions.

Aluminium (~1,000 nm)-coated sample exposed for 3,000 h

Figure 43 shows the SEM micrographs of the sample with Al coating on the fuel-side. After pre-oxidation, the uncoated air-side of the sample (see Figure 43a) reveals a surface that is partially covered with small nodules, following the rolling direction of the sample. On top of these small nodules, some "plate-shaped" features, roughly 5 μm in width, can be observed. Between these small nodules, an oxide scale, similar to the one observed for the uncoated sample (see Figure 41a), is present. The fuel-facing side of the sample (see Figure 43b) depicts a surface that is fully covered with Al-rich oxide, with no visible signs of corrosion products.

After 3,000 h of exposure, the air-side of the sample is still covered with small nodules (see Figure 43c) that seem to be aligned with the rolling direction of the steel sheet. These nodules are much smaller than those on the uncoated and Ce/Co-coated samples, which explains they were not visible in the optical overview image (see Figure 40). On top of these nodules, "plate-shaped" features can be seen, which differ from the whiskers present on the uncoated and Ce/Co-coated samples. A protective oxide is present between the nodules. The morphology is identical to that observed after pre-oxidation (see Figure 43a), which indicates that the Al coating is protective against hydrogen permeation. Figure 43d depicts the cross-section of the air-side of the sample. The outer part of each small nodule consists of Fe_2O_3. These nodules appear to be thinner (~5 μm) than the nodules observed in the uncoated (~25 μm) and Ce/Co-coated (~40 μm) samples. Beneath the nodules, an $(Fe, Cr)_3O_4$ spinel was identified by EDS analysis. The protective layer present between the nodules is composed of a $(Cr, Mn)_3O_4$ spinel layer followed by a Cr_2O_3 layer. The protective scale is dense, homogeneous, and approximately 200 nm in thickness, similar to the scale reported for the uncoated sample. The plan-view of the fuel-side (see Figure 43e) depicts an Al-rich oxide phase that covers the entire surface of the sample, identical to that observed after pre-oxidation. The metallic aluminium coating has been oxidised during the pre-oxidation (5 h) step to an Al-rich oxide phase. The cross-section of the fuel-side (see Figure 43f) exhibits a very thin and homogeneous Al-rich scale. The surface is wavy, although the layer thickness is homogeneous at around 500 nm. The coating thickness was 1,000 nm, which upon oxidation to Al_2O_3 would have generated a layer thickness of around 1,300 nm. Therefore, some Al is "lost", which will be discussed in more detail below. No signs of spallation of the oxide scale have been recorded for the sample, indicating good adherence of the oxidised coating.

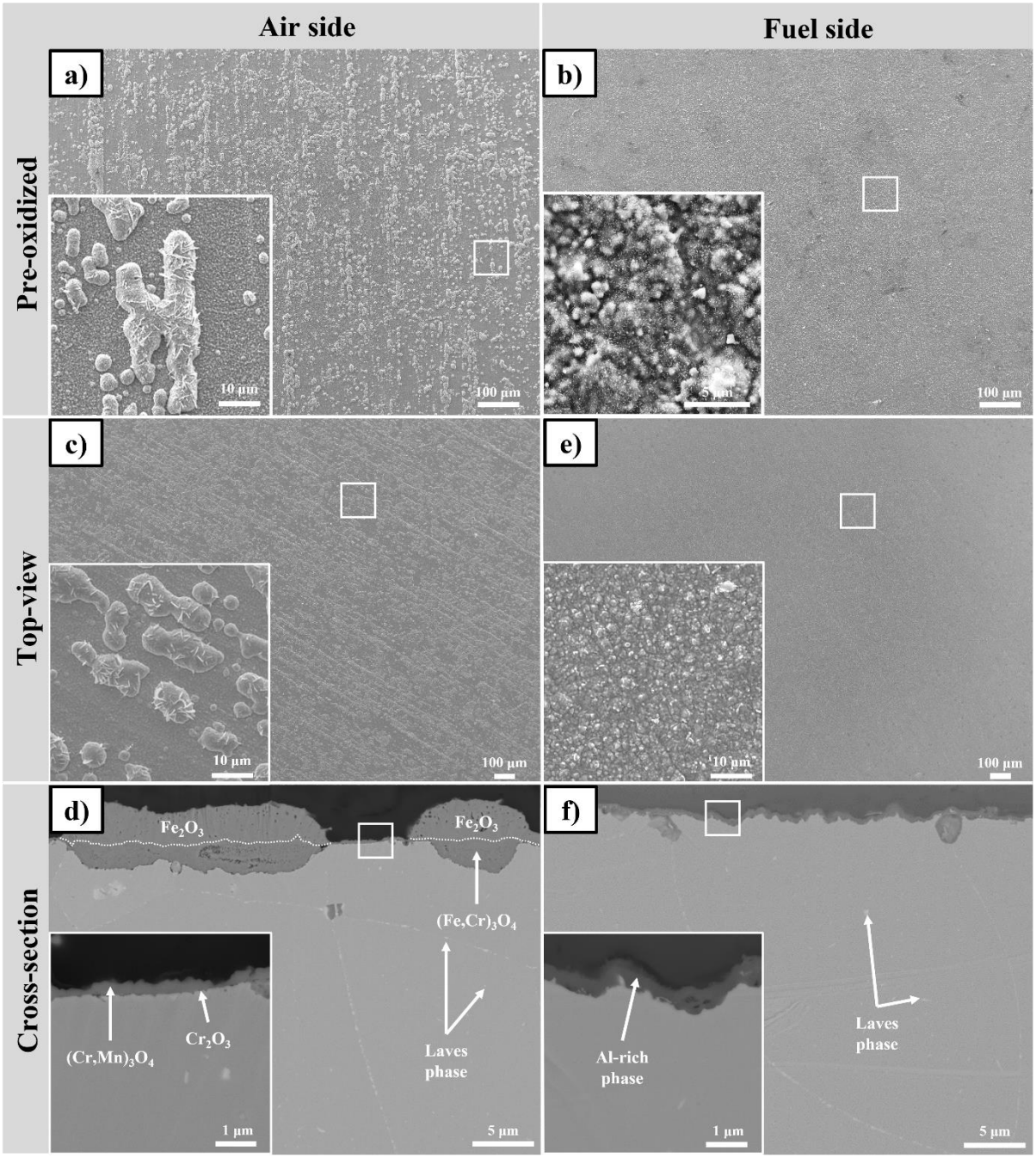

Figure 43: SEM micrographs representing: a) top-view of the air-side of the pre-oxidised sample; b) top-view of the fuel-side of the pre-oxidised sample; c) top-view of the air-side; d) cross-section of the air-side; e) top-view of the fuel-side; and f) cross-section of the fuel-side of the 441 aluminium (~1,000 nm)-coated sample exposed to the dual-atmosphere (Ar-5% H_2 + 3% H_2O // Air + 3% H_2O) for 3,000 h at 600°C.Inset: higher magnification of selected scale regions.

Aluminium (~1,000 nm) // 10 nm Ce / 600 nm Co-coated sample exposed for 7,000 h

Figure 44 shows the SEM micrographs of the Al // Ce/Co-coated sample that were exposed for 7,000 h in dual-atmosphere conditions. After the pre-oxidation step, the air-facing side of the sample (see Figure 44a) shows a protective Co-rich oxide that covers the entire surface and the presence of small nodules (~5 μm-thick) located under the oxide scale. The fuel-side of the sample (see Figure 44b) depicts a surface fully covered with an Al-rich oxide.

A longer exposure time was selected for this specific sample because optically it appeared to be completely protective after 3,000 hours. The top-view of the air-side of the sample (see Figure 44c) shows the presence of a few large Fe-rich nodules, comparable to the nodules observed on the Ce/Co-coated samples (see Figure 42c). The nodules are of equivalent size and are present at the same frequency in the two samples. Smaller nodules are visible and seem to be covered by an oxide scale and follow the rolling direction, as previously observed after pre-oxidation (see Figure 44a). The cross-section of the air-side (see Figure 5d) shows two different microstructures: a homogeneous 4-layer microstructure and a small-nodule microstructure. The outer layer of the homogeneous part consists of a $(Cr, Co)_3O_4$ spinel that contains approximately 19 at% of Cr and 15 at% of Co. The Cr in the top layer is believed to originate from the sample holder, which is a chromia former steel. The second layer consists of an almost-pure Co_3O_4 spinel that contains roughly 4 at% of Fe. The third layer is a $(Fe,Co)_3O_4$ spinel with 14 at% of Fe, 14 at% of Co, and low percentages of Cr and Mn (6 at% and 3 at%, respectively). Closest to the metal, a thin Cr_2O_3 layer is present. Overall, this 4-layer microstructure appears to be porous and is roughly 1 μm-thick. The second part consists of Fe-rich small nodules located underneath a $(Co,Cr)_3O_4$ spinel, and beneath this, a $(Fe,Cr)_3O_4$ spinel is present. The small-nodule morphology on the air-side of the Al//Ce/Co-coated sample differs from the morphology of the small nodules observed on the Ce/Co-coated sample, since an oxide layer covers them. The top-view of the fuel-side (see Figure 44e) does not show visible signs of severe corrosion and has the same morphology as that observed after pre-oxidation. The Al-rich layer is homogeneous and covers the sample. Figure 44f depicts the cross-section of the fuel-side. As specified in TABLE II, the oxide scale is much thinner than the nominal coating thickness (1,000 nm) and is less homogeneous as that observed on Al-coated sample. No signs of spallation of the oxidised coatings have been noted, indicating good adherence.

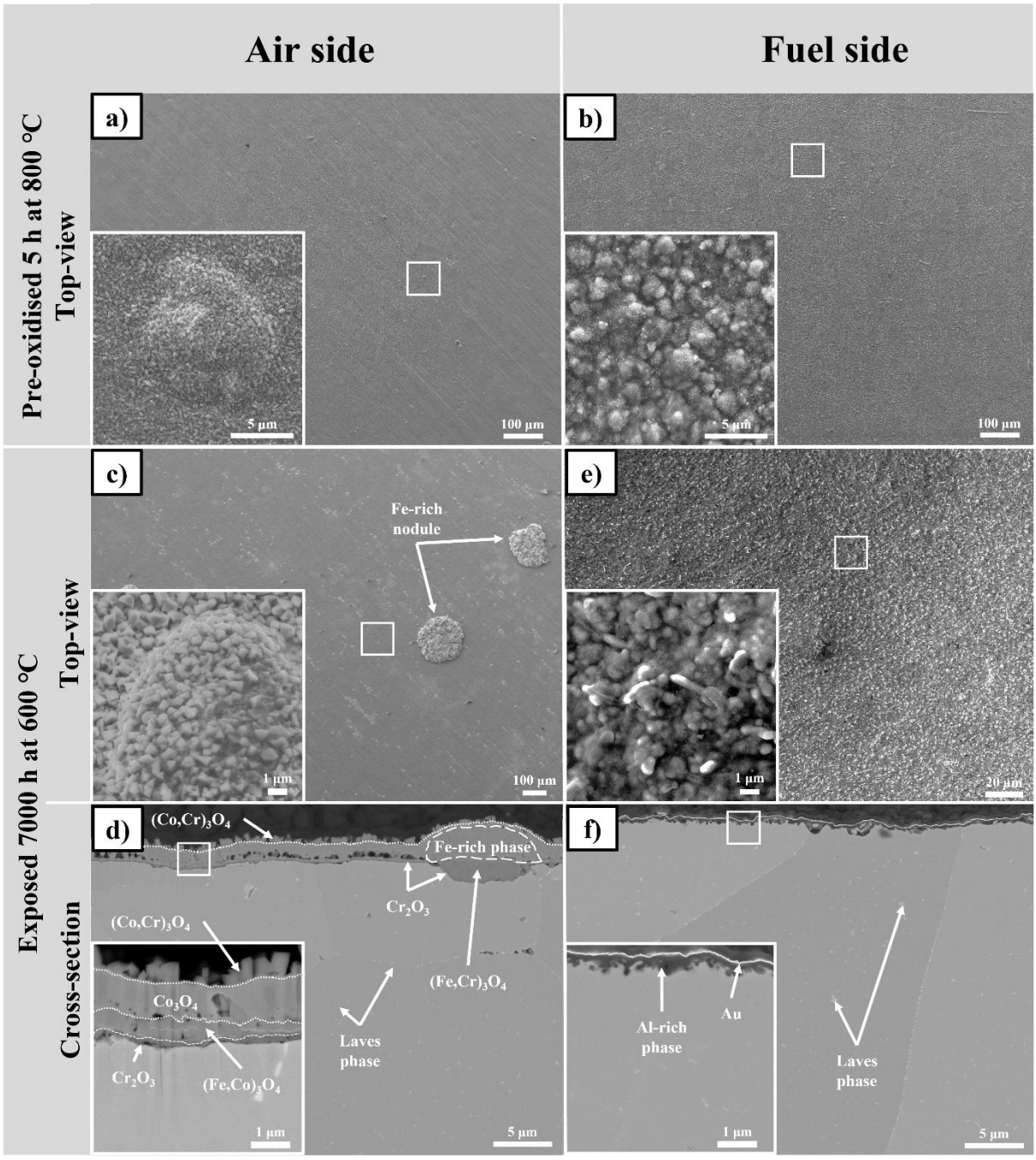

Figure 44: SEM micrographs representing: a) top-view of the air-side of the pre-oxidised sample; b) top-view of the fuel-side of the pre-oxidised sample; c) top-view of the air-side; d) cross-section of the air-side; e) top-view of the fuel-side; and f) cross-section of the fuel-side of the 441 sample with Al-coating on the fuel-side and Ce/Co-coating on the air-side, exposed to the dual-atmosphere (Ar-5% H_2 + 3% H_2O // Air + 3% H_2O) for 7,000 h at 600°C. Inset: higher magnification of selected scale regions.

Al_2O_3 (~500 nm)-coated sample exposed for 3,000 h

Figure 45 shows the SEM micrographs of the oxide scales on the air-side and fuel-side of the Al_2O_3-coated sample. After pre-oxidation, the uncoated air-facing side of the sample (see Figure 45a) shows an oxide scale that is covering the surface, similar to the uncoated sample (see Figure 41a), together with the presence of some small nodules that are around ~2 μm in thickness and still covered by the oxide scale. The fuel-side (see Figure 45b) shows a surface that is fully covered with Al_2O_3.

After 3,000 h of exposure, very few Fe_2O_3 nodules are present on the air-side (Figure 45c). Closer examination uncovers small nodules that are still covered with the oxide, as observed after pre-oxidation. The nodule size (~2 μm) is similar to that observed after pre-oxidation (see Figure 45a). The cross-section of the air-side (Figure 45d) shows a thin (~200 nm) and homogeneous $(Cr, Mn)_3O_4$ protective spinel and the presence of small $(Fe, Cr, Mn)_3O_4$ nodules, as previously seen in the top-view image (see Figure 41c) for uncoated samples. The plan-view of the fuel-side (Figure 45e) shows a protective Al_2O_3 oxide scale covering the sample, identical to that observed after pre-oxidation (see Figure 45b). However, small micro-cracks are visible on the sample surface after 3,000 h of exposure. The top layer of the fuel-side (Figure 45f) consists of a continuous Al_2O_3 oxide layer (~500 nm thick) and, closest to the metal, a thin $(Fe, Cr, Mn)_3O_4$ spinel (~200 nm in thickness). It is assumed that oxygen diffused through the micro-cracks and oxidised the steel underneath the protective Al_2O_3 layer. No signs of spallation of the oxide scale were recorded for the sample, indicating good adherence of the sputtered oxide. The desired phase for this application is α-Al_2O_3, as it has the lowest permeability to hydrogen [45-47]. However, the formation of α-Al_2O_3 is unlikely because it takes place at higher temperatures and usually with longer exposure times, and it is derived from the γ-Al_2O_3 phase [48, 49]. The Al_2O_3-coated sample on the fuel-side displays very few Fe_2O_3 nodules along the surface, indicating good protection against the dual-atmosphere effect. Previous research [50] has established the high density, low porosity, low number of defects and good stability of alumina.

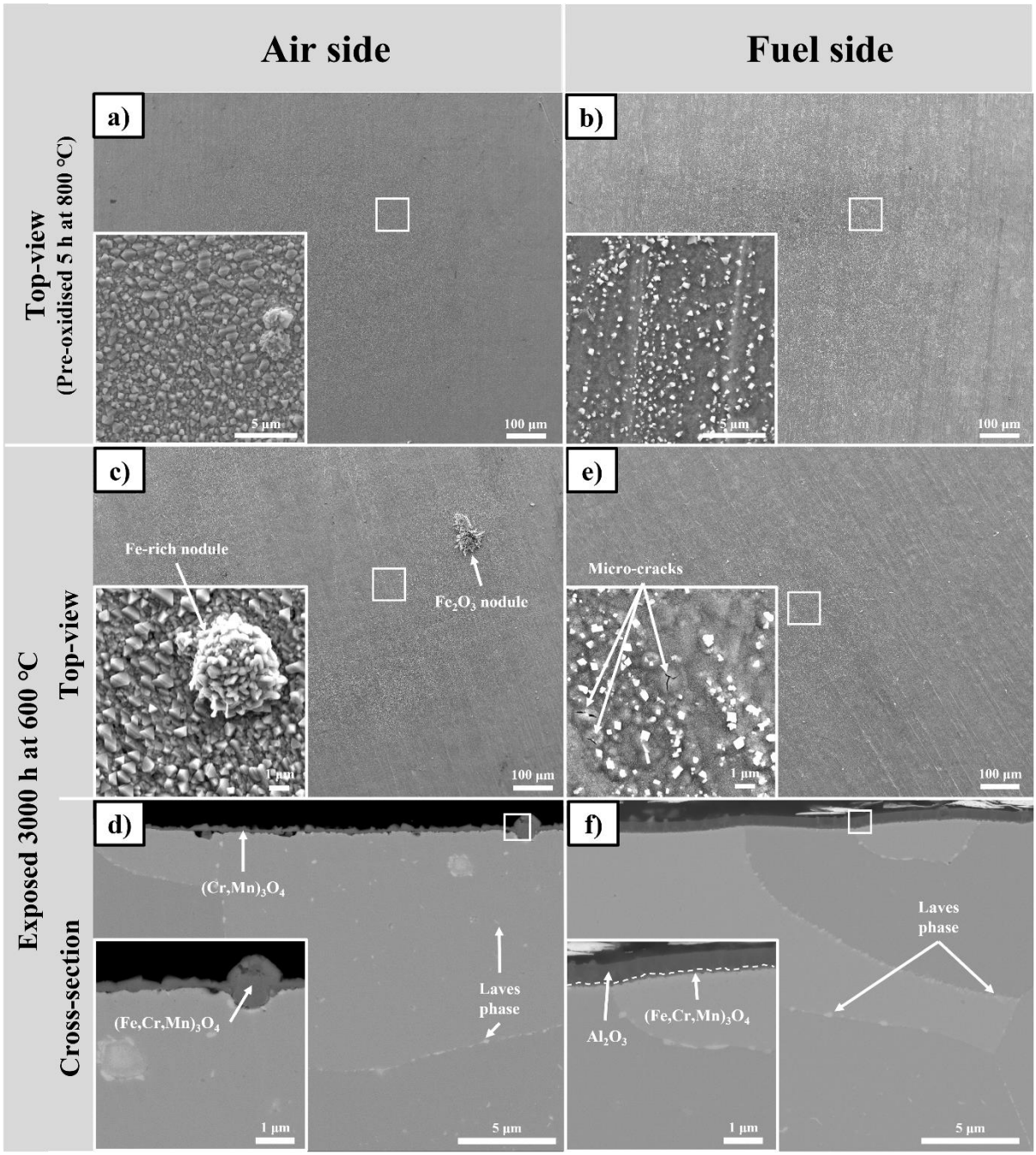

Figure 45: SEM micrographs representing: a) top-view of the air-side of the pre-oxidised sample; b) top-view of the fuel-side of the pre-oxidised sample; c) top-view of the air-side; d) cross-section of the air-side; e) top-view of the fuel-side; and f) cross-section of the fuel-side of the 441 Al_2O_3 (~500 nm)-coated sample exposed to the dual-atmosphere (Ar-5% H_2 + 3% H_2O // Air + 3% H_2O) for 3,000 h at 600°C. Inset: higher magnification of selected scale regions.

Initial interactions of the Al coatings and Al_2O_3 coatings with the substrate

The thickness of the Al coating observed here (see Figure 43f and Figure 44f) does not match the initial thickness of the Al coating (see TABLE VI). To investigate this further, the initial stages of the interactions of the Al and Al_2O_3 coatings were investigated. The samples were exposed at 800°C for 5 h, with a ramp rate of 1°C / min, in a tubular furnace under a humid airflow of 280 smL·min-1 (i.e., pre-oxidation parameters). Figure 46 shows cross-sections of the as-received Al-coated and Al_2O_3-coated samples. It is clear that the nominal thicknesses (see TABLE VI) match well with the observed thicknesses before exposure. Figure 46 shows that after 5 h of pre-oxidation at 800°C, the 1-µm-thick Al coating has shrunk to a thickness of approximately 500 nm, while the thickness of the Al_2O_3 coating is unchanged.

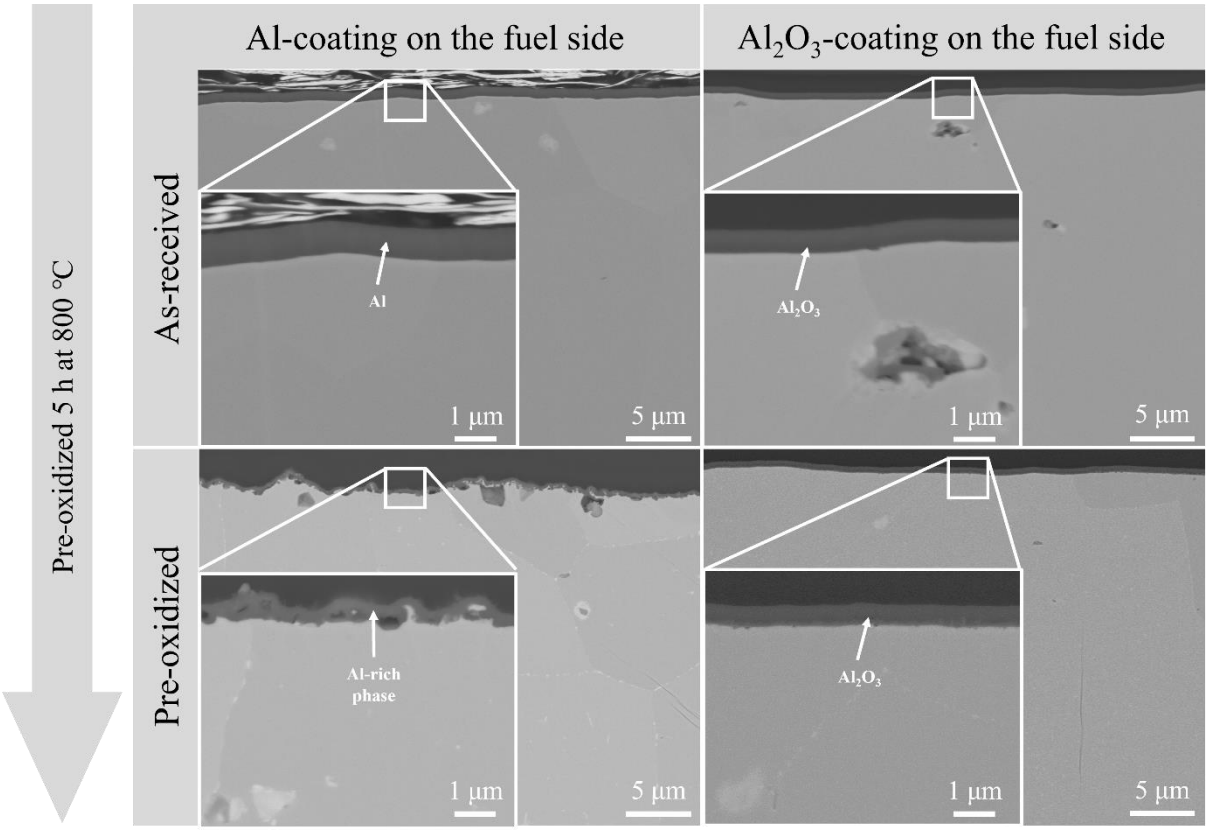

Figure 46: Effect of the pre-oxidation step on metallic Al coating. Top panel: As-received Al-coated and Al_2O_3-coated 441 steel. Bottom panel: The same surface after 5 h of pre-oxidation with up and down ramp rates of 1°C / min in humid (3% water vapour) laboratory air at 800°C.

To quantify the inter-diffusion of Al within the alloy, a line-scan analysis was conducted on the Al-coated 441 sample that was pre-oxidised for 5 h. The analysis revealed that after 5 h of pre-oxidation at 800°C, the Al had diffused into the alloy (to a depth of ~15 µm). Figure 47 displays the line-scan with the atomic percentage concentrations for the relevant species from

the surface to the bulk. A high concentration of Al is seen for a depth of up to 2 µm into the bulk. It stabilises at around 5 at% at 3 µm to 10 µm depth within the substrate and decreases thereafter. The EDS line-scan shows the presence of Fe within the top layer (at ~10 at%). The analysis was repeated twice to ensure reproducibility. This proves that Al diffuses inside the alloy during the pre-oxidation steps.

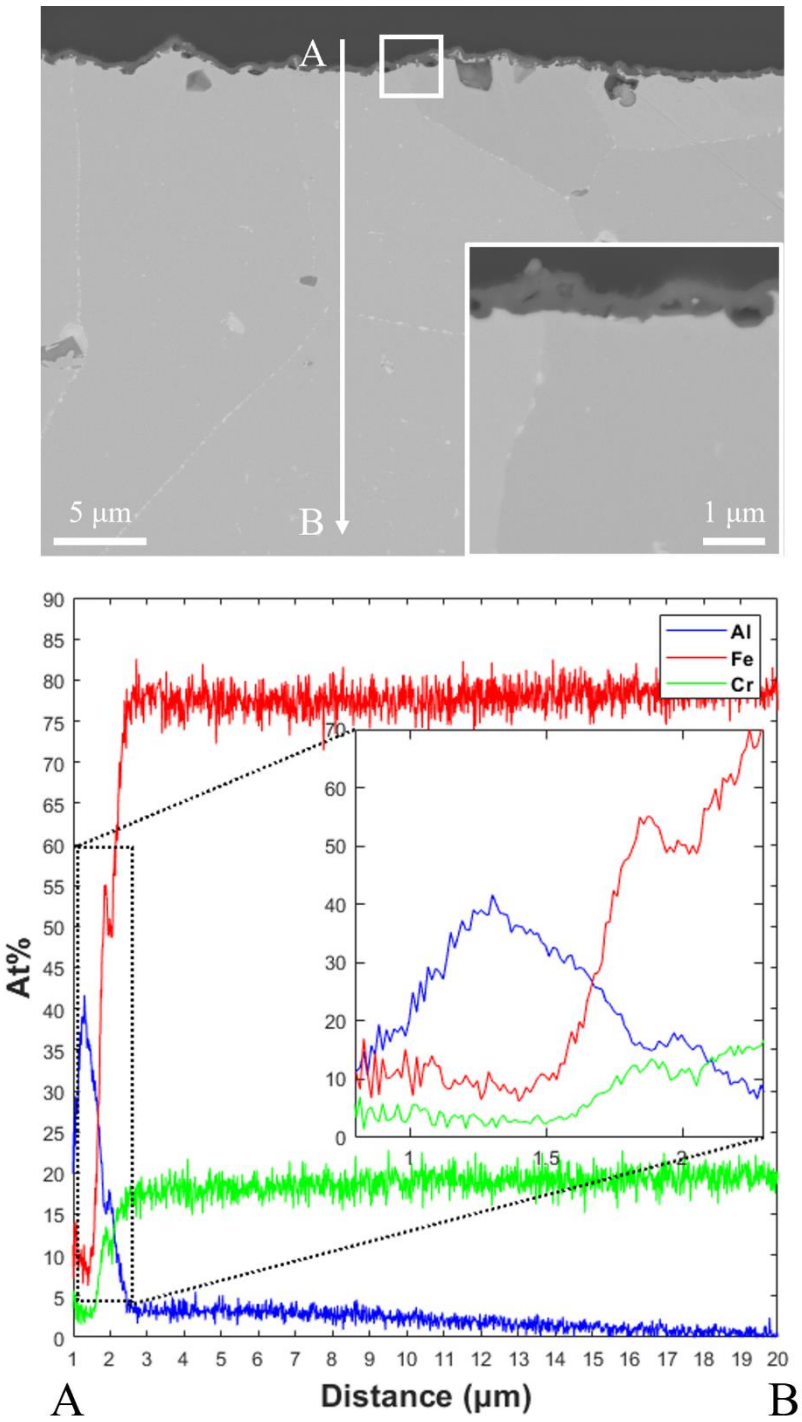

Figure 47: SEM micrograph representing the line-scan analysis used to determine the inter-diffusion of Al within the sample for an Al-coated 441 sample exposed for 5 h in humid air (3% water vapour) at 800°C with up and down ramp rates of 1°C / min.

Investigation of the conductivity of the alumina coating

The electrical conductivity of the coated interconnects directly influences the final performance of a fuel cell. Therefore, the conductivity value must be kept as low as possible and should increase as little as possible over time. A value of <100 $m\Omega \cdot cm^2$ is commonly reported as an acceptable threshold for ASR [51]. Since Al_2O_3 is known to be a poor conductor [52-54], the oxide scale resistance of the Al_2O_3-coated sample was investigated at 600°C in Ar – 5% H_2, to simulate the fuel-side atmosphere. The ASR of the uncoated sample was measured as a reference. The oxide layer formed at the air-side during exposure was ground off to evaluate the resistance of the fuel-side oxide plus coating only. Oxidation on the ground-side interface might give somewhat misleading values. Nevertheless, there was a significant difference: for the uncoated material, a value of 100 $m\Omega \cdot cm^2$ was recorded, while for the Al_2O_3-coated sample, a value of 3.8 $\Omega \cdot cm^2$ was obtained, which is much higher than what is considered to be an acceptable ASR. Impurities (originating from the sample heat treatment or ambient conditions) have marked effects on both types of conduction (ionic and electronic), which could explain the large dispersion of the measured values in this work [55, 56]. Thus, the high ASR values recorded at 600°C are in complete accordance with the results of previous research [55-57] describing alumina as an insulator at this temperature. Although it is an excellent barrier to hydrogen permeation, Al_2O_3 seems to be unsuitable for interconnect applications if anode-side contacting cannot be designed in a way to circumvent the insulating Al_2O_3 layer.

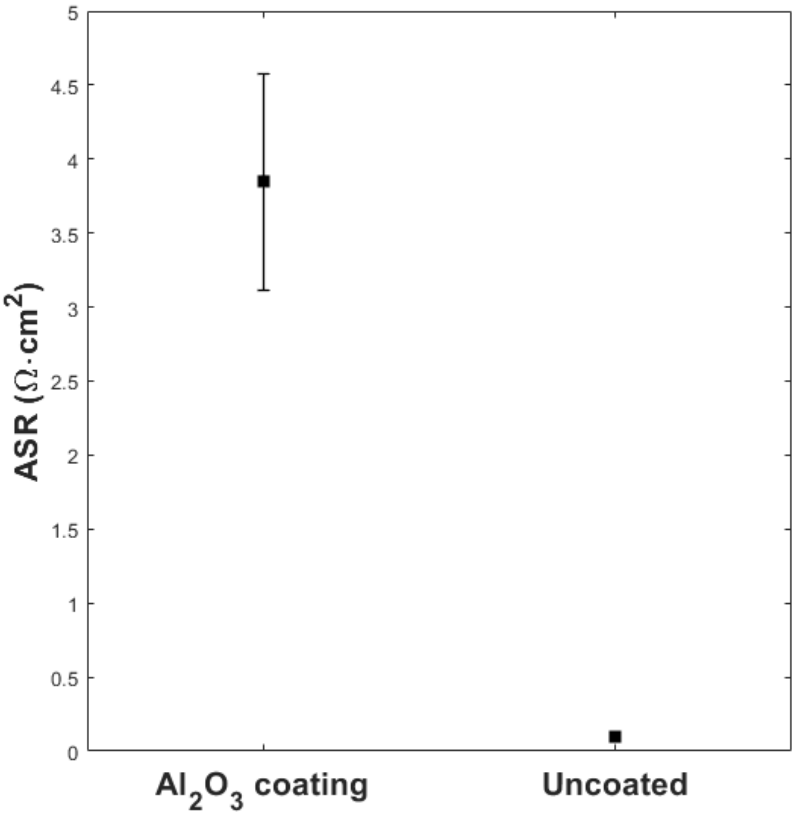

Figure 48: ASR measurements of PVD Al_2O_3-coated sample and uncoated sample, exposed to Ar – 5% H_2 – 3% H_2O with a flow rate of 120 smL·min^{-1} for 668 h at 600°C. The error bars represent the maximum and minimum values measured.

Conclusion

Air-side and fuel-side coatings have been studied in this work to evaluate their protective properties with respect to mitigating dual-atmosphere corrosion of FeCr steel at 600°C. The main findings are that:

- CeCo-coated samples on the air-side exhibit a more localised breakaway oxidation than uncoated samples;
- Metallic Al-coated samples exhibit excellent protection against hydrogen permeation, despite the initial breakaway oxidation that occurs during the pre-oxidation step;
- Al_2O_3-coated samples display the highest level of protection against the dual-atmosphere effect; and
- The combination of Ce/Co and Al coatings confer an excellent protection against the dual-atmosphere effect.

The metallic aluminium and Al_2O_3 coatings seem to be the best candidate barriers against hydrogen permeation. However, ASR measurements on alumina show very poor conductivity of this coating, making its use as a coating for SOFC interconnects challenging.

References

1. Powell, M., et al., *Demonstration of a highly efficient solid oxide fuel cell power system using adiabatic steam reforming and anode gas recirculation.* Journal of Power Sources, 2012. **205**: p. 377-384.
2. Stambouli, A.B., E.J.R. Traversa, and s.e. reviews, *Solid oxide fuel cells (SOFCs): a review of an environmentally clean and efficient source of energy.* 2002. **6**(5): p. 433-455.
3. Niewolak, L., et al., *Mechanisms of oxide scale formation on ferritic interconnect steel in simulated low and high pO2 service environments of solid oxide fuel cells.* Oxidation of metals, 2014. **82**(1): p. 123-143.
4. Horita, T., et al., *Accelerated Degradation of SOFC Cathodes by Cr Vapors*, in *SOLID OXIDE FUEL CELLS 11 (SOFC-XI)*. 2009. p. 2881-2888.
5. Stanislowski, M., et al., *Chromium vaporization from high-temperature alloys I. Chromia-forming steels and the influence of outer oxide layers.* 2007. **154**(4): p. A295-A306.
6. Hilpert, K., et al., *Chromium vapor species over solid oxide fuel cell interconnect materials and their potential for degradation processes.* 1996. **143**(11): p. 3642-3647.
7. Zhang, H., et al., *Studies on elements diffusion of Mn/Co coated ferritic stainless steel for solid oxide fuel cell interconnects application.* International journal of hydrogen energy, 2013. **38**(12): p. 5075-5083.
8. Chen, S., X. Jin, and L. Rong, *Improvement in high temperature oxidation resistance of 9% Cr ferritic–martensitic steel by enhanced diffusion of Mn.* Oxidation of Metals, 2016. **85**(1-2): p. 189-203.
9. Froitzheim, J. and J.-E. Svensson, *Multifunctional nano-coatings for SOFC interconnects.* Ecs Transactions, 2011. **35**(1): p. 2503.
10. Hou, P. and J. Stringer, *The effect of reactive element additions on the selective oxidation, growth and adhesion of chromia scales.* Materials Science and Engineering: A, 1995. **202**(1-2): p. 1-10.
11. Canovic, S., et al., *Oxidation of Co-and Ce-nanocoated FeCr steels: A microstructural investigation.* Surface and Coatings Technology, 2013. **215**: p. 62-74.
12. Falk-Windisch, H., et al., *Co-and Ce/Co-coated ferritic stainless steel as interconnect material for Intermediate Temperature Solid Oxide Fuel Cells.* Journal of Power Sources, 2017. **343**: p. 1-10.
13. Froitzheim, J., et al., *Long term study of Cr evaporation and high temperature corrosion behaviour of Co coated ferritic steel for solid oxide fuel cell interconnects.* Journal of Power Sources, 2012. **220**: p. 217-227.
14. Alnegren, P., et al., *Severe dual atmosphere effect at 600 C for stainless steel 441.* Journal of Power Sources, 2016. **301**: p. 170-178.
15. Gunduz, K.O., et al., *The effect of hydrogen on the breakdown of the protective oxide scale in solid oxide fuel cell interconnects.* Corrosion Science, 2021. **179**: p. 109112.
16. Sabioni, A.C.S., et al., *Comparative study of high temperature oxidation behaviour in AISI 304 and AISI 439 stainless steels.* Materials Research, 2003. **6**(2): p. 179-185.
17. Yang, Z., et al., *Anomalous corrosion behavior of stainless steels under SOFC interconnect exposure conditions.* electrochemical and solid-state letters, 2003. **6**(10): p. B35.
18. Yang, Z., et al., *Oxidation behavior of ferritic stainless steels under SOFC interconnect exposure conditions.* Journal of the Electrochemical Society, 2004. **151**(12): p. B669.
19. Alnegren, P., et al., *Temperature dependence of corrosion of ferritic stainless steel in dual atmosphere at 600–800 C.* Journal of Power Sources, 2018. **392**: p. 129-138.
20. Kurokawa, H., K. Kawamura, and T. Maruyama, *Oxidation behavior of Fe–16Cr alloy interconnect for SOFC under hydrogen potential gradient.* Solid State Ionics, 2004. **168**(1-2): p. 13-21.
21. Rufner, J., et al., *Oxidation behavior of stainless steel 430 and 441 at 800 C in single (air/air) and dual atmosphere (air/hydrogen) exposures.* International Journal of Hydrogen Energy, 2008. **33**(4): p. 1392-1398.
22. Stygar, M., et al., *Oxidation properties of ferritic stainless steel in dual Ar–H2–H2O/air*

atmosphere exposure with regard to SOFC interconnect application. Solid State Ionics, 2014. **262**: p. 449-453.
23. Horita, T., et al., *Oxide scale formation and stability of Fe–Cr alloy interconnects under dual atmospheres and current flow conditions for SOFCs.* Journal of the Electrochemical Society, 2006. **153**(11): p. A2007.
24. Horita, T., et al., *Evaluation of Fe-Cr alloys as interconnects for reduced operation temperature SOFCs.* Journal of the Electrochemical Society, 2003. **150**(3): p. A243.
25. Gagliani, L., et al., *The Influence of Humidity Content on Ferritic Stainless Steels Used in Solid Oxide Fuel Cell Under Dual Atmosphere Conditions at 600° C.* ECS Transactions, 2021. **103**(1): p. 1809.
26. Nakagawa, K., Y. Matsunaga, and T. Yanagisawa, *Corrosion behavior of ferritic steels on the air sides of boiler tubes in a steam/air dual environment.* Materials at high temperatures, 2003. **20**(1): p. 67-73.
27. Ardigo, M., et al., *Dual atmosphere study of the K41X stainless steel for interconnect application in high temperature water vapour electrolysis.* International Journal of Hydrogen Energy, 2015. **40**(15): p. 5305-5312.
28. Goebel, C., et al., *The effect of pre-oxidation parameters on the corrosion behavior of AISI 441 in dual atmosphere.* international journal of hydrogen energy, 2018. **43**(31): p. 14665-14674.
29. Li, J., et al., *Investigation of anomalous oxidation behavior of SUS430 alloy in solid oxide fuel cell dual atmosphere.* Journal of the Electrochemical Society, 2017. **164**(14): p. C945.
30. Zhao, Y. and J. Fergus, *Oxidation of alloys 430 and 441 in SOFC dual atmospheres: effects of flow rate and humidity.* Journal of The Electrochemical Society, 2011. **159**(3): p. C109.
31. Skilbred, A.W.B. and R. Haugsrud, *The effect of dual atmosphere conditions on the corrosion of Sandvik Sanergy HT.* International Journal of Hydrogen Energy, 2012. **37**(9): p. 8095-8101.
32. Amendola, R., et al., *Oxidation behavior of coated and preoxidized ferritic steel in single and dual atmosphere exposures at 800 C.* Surface and Coatings Technology, 2012. **206**(8-9): p. 2173-2180.
33. Reisert, M., et al., *Corrosion of Chromia-Forming and Alumina-Forming Ferritic Stainless Steels under Dual Atmosphere Exposure Conditions.* Journal of The Electrochemical Society, 2021. **168**(11): p. 111506.
34. Essuman, E., et al., *The effect of water vapor on selective oxidation of Fe–Cr alloys.* Oxidation of metals, 2008. **69**(3): p. 143-162.
35. Hammer, J., et al., *The oxidation of ferritic stainless steels in simulated solid-oxide fuel-cell atmospheres.* Oxidation of Metals, 2007. **67**(1): p. 1-38.
36. Skilbred, A.W.B. and R. Haugsrud, *The effect of water vapour on the corrosion of Sandvik Sanergy HT under dual atmosphere conditions.* Oxidation of metals, 2013. **79**(5): p. 639-654.
37. Froitzheim, J., et al., *Investigation of chromium volatilization from FeCr interconnects by a denuder technique.* Journal of The Electrochemical Society, 2010. **157**(9): p. B1295-B1300.
38. Reisert, M., et al. *Preformed Oxide Scale Chemistry and Its Influence on Local Metal Loss During Dual Atmosphere Corrosion*. in *TMS 2020 149th Annual Meeting & Exhibition Supplemental Proceedings*. 2020. Springer.
39. Nemanič, V., *Hydrogen permeation barriers: Basic requirements, materials selection, deposition methods, and quality evaluation.* Nuclear Materials and Energy, 2019. **19**: p. 451-457.
40. Charles, H. and H. Charles, *Hydrogen Permeation Barrier Coatings.* 2008.
41. Jung, I.-H., *Critical evaluation and thermodynamic modeling of the Mn–Cr–O system for the oxidation of SOFC interconnect.* Solid State Ionics, 2006. **177**(7): p. 765-777.
42. Kurokawa, H., et al., *Hydrogen permeation through Fe-16Cr alloy interconnect in atmosphere simulating SOFC at 1073 K.* Journal of The Electrochemical Society, 2004. **151**(8): p. A1264.
43. Stanislowski, M., et al., *Reduction of chromium vaporization from SOFC interconnectors by highly effective coatings.* Journal of Power Sources, 2007. **164**(2): p. 578-589.
44. Falk-Windisch, H., et al., *Chromium vaporization from mechanically deformed pre-coated interconnects in Solid Oxide Fuel Cells.* Journal of Power Sources, 2015. **297**: p. 217-223.
45. Roberts, R.M., et al., *Hydrogen permeability of sintered aluminum oxide.* Journal of the American Ceramic Society, 1979. **62**(9-10): p. 495-499.

46. Shirasaka, H., et al., *Analysis of gas permeability of porous alumina powder compacts.* Journal of Asian Ceramic Societies, 2013. **1**(4): p. 368-373.
47. Serra, E., et al., *Hydrogen permeation measurements on alumina.* Journal of the American Ceramic Society, 2005. **88**(1): p. 15-18.
48. Dynys, F.W. and J.W. Halloran, *Alpha alumina formation in alum-derived gamma alumina.* Journal of the American Ceramic Society, 1982. **65**(9): p. 442-448.
49. Chraska, P., et al., *Alumina-base plasma-sprayed materials part I: Phase stability of alumina and alumina-chromia.* Journal of thermal spray technology, 1997. **6**(3): p. 320-326.
50. Ruppi, S., *Deposition, microstructure and properties of texture-controlled CVD α-Al2O3 coatings.* International Journal of Refractory Metals and Hard Materials, 2005. **23**(4-6): p. 306-316.
51. Piccardo, P., et al., *ASR evaluation of different kinds of coatings on a ferritic stainless steel as SOFC interconnects.* Surface and Coatings Technology, 2007. **202**(4): p. 1221-1225.
52. Arizumi, T. and S. Tani, *On the Electrical Conductivity of Alumina.* Journal of the Physical Society of Japan, 1950. **5**(6): p. 442-447.
53. Cohen, J., *Electrical conductivity of alumina.* Am. Ceram. Soc. Bull., 1959. **38**(9): p. 441-46.
54. Schemmel, R., et al., *ELECTRICAL PROPERTIES OF A POLYCRYSTALLINE ALUMINA SAMPLE*. 1972, Hanford Engineering Development Lab., Richland, WA (United States).
55. Auerkari, P., *Mechanical and physical properties of engineering alumina ceramics*. Vol. 23. 1996: Technical Research Centre of Finland Espoo.
56. Insley, R.H., *Electrical properties of alumina ceramics*, in *Alumina chemicals: Science and technology handbook*. 1990, The American Ceramic Society Westerville, OH. p. 293-297.
57. Miranzo, P., et al., *effect of sintering atmosphere on the densification and electrical properties of alumina.* Journal of the American Ceramic Society, 1990. **73**(7): p. 2119-2121.